

AN H I IMAGING SURVEY OF ASYMPTOTIC GIANT BRANCH STARS

L. D. MATTHEWS¹, T. LE BERTRE², E. GÉRARD³, M. C. JOHNSON⁴

Accepted to AJ

ABSTRACT

We present an imaging study of a sample of eight asymptotic giant branch (AGB) stars in the H I 21-cm line. Using observations from the Very Large Array, we have unambiguously detected H I emission associated with the extended circumstellar envelopes of six of the targets. The detected H I masses range from $M_{\text{HI}} \approx 0.015 - 0.055 M_{\odot}$. The H I morphologies and kinematics are diverse, but in all cases appear to be significantly influenced by the interaction between the circumstellar envelope and the surrounding medium. Four stars (RX Lep, Y UMa, Y CVn, and V1942 Sgr) are surrounded by detached H I shells ranging from 0.36 to 0.76 pc across. We interpret these shells as resulting from material entrained in a stellar outflow being abruptly slowed at a termination shock where it meets the local medium. RX Lep and TX Psc, two stars with moderately high space velocities ($V_{\text{space}} > 56 \text{ km s}^{-1}$), exhibit extended gaseous wakes (~ 0.3 and 0.6 pc in the plane of the sky), trailing their motion through space. The other detected star, R Peg, displays a peculiar “horseshoe-shaped” H I morphology with emission extended on scales up to ~ 1.7 pc; in this case, the circumstellar debris may have been distorted by transverse flows in the local interstellar medium. We briefly discuss our new results in the context of the entire sample of evolved stars that has been imaged in H I to date.

Subject headings: stars: AGB and post-AGB – stars: winds, outflows – circumstellar matter – radio lines: stars

1. INTRODUCTION

Stars on the asymptotic giant branch (AGB) undergo substantial mass-loss through cool, low-velocity winds ($V_{\text{out}} \sim 10 \text{ km s}^{-1}$). These winds are one of the dominant means through which chemically enriched material is recycled back into the Galaxy to sustain new generations of star and planet formation (e.g., Schröder & Sedlmayr 2001; Cristallo et al. 2009; Leitner & Kravtsov 2011). The distribution of circumstellar debris on the largest scales may also be important for the subsequent evolution of novae, planetary nebulae and some Type Ia supernovae (e.g., Wang et al. 2004; Mohamed & Podsiadlowski 2007; Wareing et al. 2007a; Chiotellis et al. 2012; Roy et al. 2012). In addition, the outflows and space motions of these mass-losing stars play a role in shaping the structure of the interstellar medium (ISM) on parsec and sub-parsec scales (Villaver et al. 2002; Wareing et al. 2007b; Begum et al. 2010).

It has long been recognized that the interstellar environment of evolved stars can have a profound impact on the observed mass, size, shape, and chemical composition of their circumstellar envelopes (hereafter CSEs; e.g., Smith 1976; Isaacman 1979; Young et al. 1993b; Villaver et al. 2002, 2012; Wareing et al. 2006; 2007a, b, c; Wareing 2012; see also the review by Stencel 2009). Nonetheless, the interfaces through which AGB stars interact with their environments have remained poorly studied observationally. One problem is that CSEs can be enormously extended ($\gtrsim 1$ pc), and their chemical

compositions change as a function of distance from the star as densities drop, and molecules become dissociated by the interstellar radiation field or other radiation sources. The result is that some of the most frequently used observational tracers of CSEs (e.g., CO, SiO, H₂O, and OH masers) do not probe the outermost CSE or its interaction zone with the ISM. In some cases, more extended material can be traced via imaging observations in the far-infrared (FIR; e.g., Young et al. 1993a, b; Zijlstra & Weinberger 2002; Ueta et al. 2006, 2010; Cox et al. 2012a) or in the far-ultraviolet (FUV; Martin et al. 2007; Sahai & Chronopoulos 2010), but such data do not supply any direct kinematic information.

Recent studies have demonstrated that the H I 21-cm line of neutral hydrogen is a powerful tool for the study of extended CSEs and their interface with their larger-scale environments (e.g., Gérard & Le Bertre 2006; Matthews & Reid 2007; Libert et al. 2007, 2008, 2010a, b; Matthews et al. 2008, 2011a, b, 2012; Gérard et al. 2011a, b). Not only is hydrogen the most plentiful constituent of CSEs, but H I line measurements provide valuable kinematic information and can be directly translated into measurements of atomic hydrogen mass. Furthermore, because H I is not destroyed by the interstellar radiation field, H I measurements are particularly well-suited to probing the outermost reaches of CSEs.

While the number of evolved stars detected in the H I line has grown steadily over the past decade thanks to ongoing surveys with the Nançay Radio Telescope (NRT; Le Bertre & Gérard 2001, 2004; Gérard & Le Bertre 2003; Gérard & Le Bertre 2006; Gardan et al. 2006; Libert et al. 2008, 2010a; Gérard et al. 2011a, b), the number of stars that has been imaged in H I with aperture synthesis arrays has remained small (Bowers & Knapp 1987, 1988; Matthews & Reid 2007; Matthews et al. 2008, 2011b, 2012; Le Bertre et al. 2012). Such imaging observations offer a crucial complement to single-dish measure-

¹ MIT Haystack Observatory, Off Route 40, Westford, MA 01886 USA; lmatthew@haystack.mit.edu

² LERMA, UMR 8112, Observatoire de Paris, 61 av. de l’Observatoire, F-75014 Paris, France

³ GEPI, UMR 8111, Observatoire de Paris, 5 Place J. Janssen, F-92195 Meudon Cedex, France

⁴ University of Texas at Austin, Department of Astronomy, 2515 Speedway, Stop C1400, Austin, TX 78712 USA

ments, since the high angular resolution of interferometers provides detailed information on the structure and spatially resolved kinematics of the CSE and enables detailed comparisons with observations of the CSE at other wavelengths. In addition, interferometers act as effective filters against large-scale Galactic contamination along the line-of-sight, allowing stellar signals to be more readily disentangled from background radiation.

In this paper we present new H I imaging observations of eight mass-losing AGB stars, effectively doubling the existing sample. We describe in detail the results for each individual star, followed by a discussion of emerging trends from the combined sample of evolved stars that has been imaged in H I to date.

2. SAMPLE SELECTION

The targets for the present study of circumstellar H I comprise a set of eight Galactic AGB stars spanning a range in properties, including effective temperature, mass-loss rate, variability class, and chemistry. Some basic parameters of the sample are summarized in Table 1. None of the stars in our current program is a known or suspected binary, although two binary AGB stars, R Aqr and Mira, have been observed in H I as part of our earlier studies (Matthews & Reid 2007; Matthews et al. 2008).

Six of our targets (RX Lep, Y UMa, R Peg, Y CVn, V1942 Sgr, and TX Psc) were selected from the growing sample of AGB stars that has been detected in H I using single-dish observations with the NRT (see above). As we were interested in imaging examples of both carbon-rich and oxygen-rich stars, we selected three from each chemistry type, all of which are relatively nearby and exhibited relatively strong peak H I signals based on the previous NRT measurements ($\gtrsim 0.1$ Jy). In the case of Y UMa, R Peg, Y CVn and V1942 Sgr, an additional motivation for selection was that line-of-sight confusion from Galactic emission near the stellar systemic velocity is low. Imposing this selection criterion results in the selection of stars at high Galactic latitudes that are more likely to be Population II stars. In contrast, RX Lep and TX Psc exhibit moderate and moderately strong line-of-sight confusion, respectively, but were included in our sample owing to evidence for elongated H I morphologies based on single-dish measurements (Gérard & Le Bertre 2006). Finally, we downloaded previously unpublished data for two stars (IK Tau and AFGL 3099) from the Very Large Array (VLA) archive (see Table 2). Both of these stars were previously targeted in single-dish H I surveys but neither was detected (Zuckerman et al. 1980; Gérard & Le Bertre 2006).

3. OBSERVATIONS AND DATA REDUCTION

The data that we present here are a combination of new and archival H I 21-cm line observations obtained with the VLA of the National Radio Astronomy Observatory (NRAO).⁵ All of the data were obtained using the most compact (D) configuration (0.035-1.0 km baselines) of the VLA, providing sensitivity to emission on scales of up to $\sim 15'$. The primary beam of the VLA at our observing frequency is $\sim 31'$. The data were reduced and

imaged using the Astronomical Image Processing System (AIPS). Further details are described below.

3.1. New VLA Observations

Our new VLA observations for six stars were obtained throughout the transition period during which the original VLA antennas were being retrofitted as part of the Expanded Very Large Array (EVLA) upgrade. Throughout this period, the array contained fewer than the nominal 27 antennas (Table 2). As described below, the use of this “hybrid” array necessitated special care during the calibration process.

For the observations of R Peg and Y UMa, the VLA correlator was used in dual polarization (2AC) mode with a 0.78 MHz bandpass, yielding 256 spectral channels with 3.05 kHz spacing, providing an effective velocity resolution of ~ 0.64 km s⁻¹. For V1942 Sgr, RX Lep, TX Psc, and Y CVn, the VLA correlator was used in 1A mode with a 1.5 MHz bandwidth and 512 spectral channels. This mode provided a single right circular (RR) polarization and a 3.05 kHz channel spacing.

The band center velocities adopted for each star are summarized in Table 2. In some cases, the band center was offset from the systemic velocity of the star to shift strong Galactic emission away from the band edges. Total integration times spent on each target are also summarized in Table 2, along with additional details related to the observations.

The observations of the target stars were interspersed with observations of a complex gain calibrator approximately every 20-25 minutes. Either 3C48 (0137+331) or 3C286 (1331+305) was used as an absolute flux calibrator, and in all cases, an additional strong point source was observed as a bandpass calibrator (see Table 3). To insure that the absolute flux scale and bandpass calibration were not corrupted by Galactic emission in the band, the flux and bandpass calibrators were each observed twice, with the band shifted by sufficient positive and negative frequency offsets so as to shift Galactic H I emission out of the band. H I survey spectra from Kalberla et al. (2005) were used to determine the required frequency offsets, and the adopted center frequencies are summarized in Table 3. Each of the gain calibrators was also observed once at each of these offset frequencies to insure accurate bootstrapping of the absolute flux scale. We estimate that the resulting flux density scale for each target star has an uncertainty of $\lesssim 10\%$ (see also §3.3).

3.1.1. Calibration of the R Peg and Y UMa Observations

Traditionally, the calibration of VLA data sets employs a “channel 0” data set formed by taking a vector average of the inner 75% of the observing band. However, the mismatch in bandpass response between the VLA and EVLA antennas causes closure errors in the channel 0 data computed this way.⁶ Furthermore, the hardware used to convert the digital signals from the EVLA antennas into analog signals for the VLA correlator caused aliased power in the bottom 0.5 MHz of the baseband (i.e., at low-numbered channels).⁷ This aliasing is of consequence because of the narrow bandwidth used for our

⁵ The National Radio Astronomy Observatory is operated by Associated Universities, Inc., under cooperative agreement with the National Science Foundation.

⁶ <http://www.vla.nrao.edu/astro/guides/evlaretturn/postproc/>

⁷ <http://www.vla.nrao.edu/astro/guides/evlaretturn/aliasing/>

TABLE 1
PROPERTIES OF THE TARGET STARS

| Name | α (J2000.0) | δ (J2000.0) | l | b | $V_{\star, \text{LSR}}$ | d | T_{eff} | Spec. | Var. | \dot{M} | V_{out} |
|-------------------|--------------------|--------------------|--------|--------|-------------------------|------|------------------|----------|-------|---------------------------------|------------------------|
| (1) | (2) | (3) | (deg) | (deg) | (km s^{-1}) | (pc) | (K) | Type | Class | ($M_{\odot} \text{ yr}^{-1}$) | (km s^{-1}) |
| (1) | (2) | (3) | (4) | (5) | (6) | (7) | (8) | (9) | (10) | (11) | (12) |
| Oxygen-rich stars | | | | | | | | | | | |
| IK Tau | 03 53 28.87 | +11 24 21.7 | 177.95 | -31.41 | 34.6 | 245 | 2000-3000 | M6e-M10e | Mira | 4.2×10^{-6} | 22.0 |
| RX Lep | 05 11 22.87 | -11 50 56.72 | 212.54 | -27.51 | 28.9 | 149 | 3300 | M7 | SRb | 2.0×10^{-7} | 4.1 |
| Y UMa | 12 40 21.28 | +55 50 47.61 | 126.16 | +61.21 | 19.0 | 385 | 3100 | M7II-III | SRb | 2.6×10^{-7} | 5.4 |
| R Peg | 23 06 39.17 | +10 32 36.10 | 85.41 | -44.56 | 24.0 | 400 | 2300-2900 | M7e | Mira | 5.3×10^{-7} | 4.3 |
| Carbon-rich stars | | | | | | | | | | | |
| Y CVn | 12 45 07.82 | +45 26 24.92 | 126.44 | +71.64 | 21.1 | 272 | 2730 | C5.4J | SRb | 1.7×10^{-7} | 7.8 |
| V1942 Sgr | 19 19 09.59 | -15 54 30.03 | 21.61 | -13.19 | -33.7 | 535 | 2960 | C | Lb | $(6.1, 1.0) \times 10^{-7}$ | 17.5, 5.0 |
| AFGL 3099 | 23 28 17.50 | +10 54 36.9 | 92.23 | -46.94 | 46.6 | 1500 | 1800-2000 | C | Mira | 1.3×10^{-5} | 10.1 |
| TX Psc | 23 46 23.51 | +03 29 12.52 | 93.28 | -55.59 | 12.2 | 275 | 3115 | C5II | Lb | 3.1×10^{-7} | 10.7 |

NOTE. — Units of right ascension are hours, minutes, and seconds. Units of declination are degrees, arcminutes, and arcseconds. Explanation of columns: (1) star name; (2) & (3) right ascension and declination (J2000.0); (4) & (5) Galactic coordinates; (6) systemic velocity relative to the Local Standard of Rest (LSR); (7) adopted distance in parsecs; (8) stellar effective temperature in kelvins; (9) spectral type; (10) variability class; (11) mass-loss rate in solar masses per year; two values are quoted in cases of multi-component molecular line profiles (12) outflow velocity in km s^{-1} as determined from CO observations. Coordinates and spectral classifications were taken from SIMBAD (<http://simbad.harvard.edu>). References and additional descriptions for the other parameters are provided throughout §4.1-§4.8.

TABLE 2
SUMMARY OF VLA OBSERVATIONS

| Star | Obs. date | No. | Mode | No. | Bandwidth | V_1, V_2 | V_{cent} | $\Delta\nu$ | Δv | t |
|------------|----------------|----------|------|------|-----------|------------------------|------------------------|-------------|------------------------|---------|
| (1) | (2) | antennas | (4) | pol. | (MHz) | (km s^{-1}) | (km s^{-1}) | (kHz) | (km s^{-1}) | (hours) |
| (1) | (2) | (3) | (4) | (5) | (6) | (7) | (8) | (9) | (10) | (11) |
| IK Tau* | 1989-Dec-18 | 27 | 2AC | 2 | 0.39 | -4.6, 72.6 | 34.0 | 12.2 | 2.6 | 3.97 |
| RX Lep | 2009-Dec-30/31 | 22 | 1A | 1 | 1.5 | -135.3, 193.2 | 29.0 | 3.05 | 1.29 | 3.85 |
| | 2010-Jan-1/2 | 22 | 1A | 1 | 1.5 | -135.3, 193.2 | 29.0 | 3.05 | 1.29 | 2.75 |
| Y UMa | 2007-Apr-27 | 26 | 2AC | 2 | 0.78 | -62.8, 100.8 | 19.0 | 3.05 | 0.64 | 3.35 |
| | 2007-Apr-28 | 26 | 2AC | 2 | 0.78 | -62.8, 100.8 | 19.0 | 3.05 | 0.64 | 3.45 |
| R Peg | 2007-Apr-8 | 26 | 2AC | 2 | 0.78 | -81.8, 81.8 | 0.0 | 3.05 | 0.64 | 3.40 |
| | 2007-May-4 | 26 | 2AC | 2 | 0.78 | -81.8, 81.8 | 0.0 | 3.05 | 0.64 | 3.42 |
| Y CVn | 2010-Jan-1/2 | 22 | 1A | 1 | 1.5 | -143.1, 183.5 | 21.1 | 3.05 | 1.29 | 5.10 |
| | 2010-Jan-2/3 | 21 | 1A | 1 | 1.5 | -143.1, 183.5 | 21.1 | 3.05 | 1.29 | 0.90 |
| V1942 Sgr | 2009-Dec-5 | 23 | 1A | 1 | 1.5 | -196.2, 132.2 | -32.0 | 3.05 | 1.29 | 2.93 |
| | 2009-Dec-7 | 22 | 1A | 1 | 1.5 | -196.2, 132.2 | -32.0 | 3.05 | 1.29 | 2.88 |
| AFGL 3099* | 1989-Dec-17 | 27 | 2AC | 2 | 0.19 | 26.7, 65.3 | 46.0 | 6.10 | 1.29 | 4.23 |
| TX Psc | 2009-Dec-5/6 | 23 | 1A | 1 | 1.5 | -151.3, 177.3 | 13.0 | 3.05 | 1.29 | 0.80 |
| | 2009-Dec-7/8 | 22 | 1A | 1 | 1.5 | -151.3, 177.3 | 13.0 | 3.05 | 1.29 | 0.82 |
| | 2010-Jan-4/5 | 21 | 1A | 1 | 1.5 | -151.3, 177.3 | 13.0 | 3.05 | 1.29 | 4.00 |

NOTE. — Explanation of columns: (1) star name; (2) observing date; (3) number of available antennas; (4) VLA correlator mode; (5) number of circular polarizations; (6) total bandwidth; (7) minimum and maximum LSR velocity covered by the observing band; (8) LSR velocity at band center; (9) channel width; (10) effective velocity resolution of the data presented in this work; all data with the exceptions of Y UMa and R Peg were Hanning smoothed prior to analysis; (11) total on-source integration time.

* Archival data (see §3.2).

observations. However, it affects EVLA-EVLA baselines only, as it does not correlate on ELVA-VLA baselines.

To mitigate the above effects, we used the following modified approach to the gain calibration for the R Peg and Y UMa data sets. After applying the latest available corrections to the antenna positions and performing an initial excision of corrupted data, we computed and applied an initial bandpass calibration to our spectral line data to remove closure errors on VLA-EVLA baselines. EVLA-EVLA baselines were flagged during this step and unflagged afterward. After applying the bandpass solutions, we then computed a new frequency-averaged (channel 0) data set (using the inner 75% of the band) for use in calibrating the frequency-independent complex gains. After flagging the EVLA-EVLA baselines on the channel 0 data, we solved for the frequency-independent portion of the complex gain and transferred these solutions to the full spectral line data set. Lastly, we applied time-dependent frequency shifts to the data

to compensate for changes caused by the Earth's motion during the course of the observations.

3.1.2. Calibration of the RX Lep, Y CVn, V1942 Sgr, and TX Psc Observations

During the observations of RX Lep, Y CVn, V1942 Sgr, and TX Psc, there were too few non-EVLA antennas left in the array to utilize the calibration strategy described in §3.1.1. Instead, we increased our observing bandwidth by a factor of two (at the cost of limiting ourselves to a single polarization product) to provide a suitable amount of bandwidth uncorrupted by aliasing. We then employed the following calibration approach.

After applying the latest available antenna position corrections and performing an initial excision of corrupted data, we computed and applied a bandpass calibration to the spectral line data to remove closure errors on VLA-EVLA baselines. All baselines were used in the calculation, but the bandpass was normalized using

TABLE 3
CALIBRATION SOURCES

| Source | α (J2000.0) | δ (J2000.0) | Flux Density (Jy) | ν_0 (MHz) | Date |
|-----------------------|--------------------|--------------------|-------------------|---------------|-------------|
| 3C48 ^a | 01 37 41.2994 | +33 09 35.132 | 15.8851* | 1419.5 | 2007-Apr-8 |
| | | | 15.8675* | 1420.5 | 2007-Apr-8 |
| | | | 15.8847* | 1419.5 | 2007-May-4 |
| | | | 15.8671* | 1420.5 | 2007-May-4 |
| | | | 15.8905* | 1418.9 | 2009-Dec-6 |
| | | | 15.8691* | 1421.3 | 2009-Dec-6 |
| | | | 15.8905* | 1418.9 | 2009-Dec-8 |
| | | | 15.8691* | 1421.3 | 2009-Dec-8 |
| | | | 15.8885* | 1419.1 | 2009-Dec-31 |
| | | | 15.8701* | 1421.5 | 2009-Dec-31 |
| | | | 15.8885* | 1419.1 | 2010-Jan-2 |
| | | | 15.8701* | 1421.5 | 2010-Jan-2 |
| | | | 15.8868* | 1419.3 | 2010-Jan-5 |
| | | | 15.8696* | 1421.2 | 2010-Jan-5 |
| 0022+002 ^b | 00 22 25.42 | +00 14 56.16 | 2.92±0.06 | 1420.2 | 2009-Dec-6 |
| | | | 3.02±0.07 | 1420.2 | 2009-Dec-8 |
| | | | 2.73±0.05 | 1420.2 | 2010-Jan-2 |
| 0409+122 ^c | 04 09 22.00 | +12 17 39.84 | 0.814±0.002 | 1420.7 | 1989-Dec-18 |
| 0459+024 ^d | 04 59 52.05 | +02 29 31.17 | 1.72±0.04 | 1420.1 | 2009-Dec-31 |
| 1227+365 ^e | 12 27 58.72 | +36 35 11.82 | 1.79±0.03 | 1420.1 | 2010-Jan-2 |
| | | | 1.97±0.04 | 1420.4 | 2010-Jan-2 |
| 1252+565 ^f | 12 52 26.38 | +56 34 19.41 | 2.07±0.06 | 1420.4 | 2010-Jan-3 |
| | | | 2.20±0.02 | 1420.3 | 2007-Apr-27 |
| 3C286 ^g | 13 31 08.2879 | +30 30 32.958 | 2.22±0.01 | 1420.3 | 2007-Apr-28 |
| | | | 16.0394* | 1420.3 | 1989-Dec-18 |
| | | | 14.7317* | 1419.3 | 2007-Apr-27 |
| | | | 14.7218* | 1421.3 | 2007-Apr-27 |
| | | | 14.7317* | 1419.3 | 2007-Apr-28 |
| | | | 14.7218* | 1421.3 | 2007-Apr-28 |
| | | | 14.7305* | 1419.5 | 2010-Jan-2 |
| | | | 14.7193* | 1421.8 | 2010-Jan-2 |
| | | | 14.7305* | 1419.5 | 2010-Jan-3 |
| | | | 14.7193* | 1421.8 | 2010-Jan-3 |
| 1411+522 ^h | 14 11 20.64 | +52 12 09.14 | 21.63±0.08 | 1419.3 | 2007-Apr-27 |
| | | | 21.72±0.06 | 1421.3 | 2007-Apr-27 |
| | | | 21.84±0.05 | 1419.3 | 2007-Apr-28 |
| | | | 21.78±0.05 | 1421.3 | 2007-Apr-28 |
| | | | 21.83±0.20 | 1420.4 | 2010-Jan-2 |
| | | | 22.01±0.73 | 1420.4 | 2010-Jan-3 |
| 1911-201 ⁱ | 19 11 09.65 | -20 06 55.10 | 2.17±0.04 | 1420.5 | 2009-Dec-5 |
| 2253+161 ^j | 22 53 57.74 | +16 08 53.56 | 2.24±0.08 | 1420.5 | 2009-Dec-7 |
| | | | 14.71±0.04 | 1419.5 | 2007-Apr-8 |
| | | | 14.69±0.04 | 1421.5 | 2007-Apr-8 |
| | | | 14.46±0.05 | 1419.5 | 2007-May-4 |
| | | | 14.51±0.04 | 1421.5 | 2007-May-4 |
| | | | 14.13±0.10 | 1418.9 | 2009-Dec-7 |
| | | | 13.42±0.17 | 1419.5 | 2010-Jan-4 |
| | | | 13.31±0.14 | 1421.8 | 2010-Jan-4 |
| 2255+132 ^k | 22 55 03.73 | +13 13 33.01 | 2.65±0.01 | 1420.5 | 2007-Apr-8 |
| | | | 2.66±0.02 | 1420.5 | 2007-May-4 |
| 2330+110 ^l | 23 30 40.85 | +11 00 18.70 | 1.117±0.003 | 1420.0 | 1989-Dec-17 |

NOTE. — Units of right ascension are hours, minutes, and seconds, and units of declination are degrees, arcminutes, and arcseconds. ν_0 is the frequency at which the flux density in the fourth column was computed. For the archival data (§3.2), the phase center coordinates and phase calibrator names have been translated from B1950.0 to J2000.0 coordinates.

* Adopted flux density, computed according to the VLA Calibration Manual (Perley & Taylor 2003).

^a Primary flux calibrator and bandpass calibrator for RX Lep, R Peg, V1942 Sgr, and TX Psc

^b Secondary gain calibrator for TX Psc

^c Secondary gain calibrator for IK Tau

^d Secondary gain calibrator for RX Lep

^e Secondary gain calibrator for Y CVn

^f Secondary gain calibrator for Y UMa

^g Primary flux calibrator for IK Tau, Y UMa, Y CVn, and AFGL 3099; bandpass calibrator for Y UMa and Y CVn

^h Bandpass calibrator for Y UMa and Y CVn

ⁱ Secondary gain calibrator for V1942 Sgr

^j Bandpass calibrator for R Peg and TX Psc

^k Secondary gain calibrator for R Peg

^l Secondary gain calibrator for AFGL 3099

TABLE 4
DECONVOLVED IMAGE CHARACTERISTICS

| Source | Type | \mathcal{R} | Taper (k λ ,k λ) | θ_{FWHM} ("' \times "') | PA (degrees) | rms (mJy beam $^{-1}$) | Continuum velocities (km s $^{-1}$) | Clean Boxes? |
|--------------------|-------|---------------|--------------------------------------|--|-----------------|----------------------------|--|--------------|
| (1) | (2) | (3) | (4) | (5) | (6) | (7) | (8) | (9) |
| IK Tau | line | +5 | ... | 69''2 \times 51''7 | 32.1 | 1.4 | 57.2 to 72.6 | no |
| IK Tau | cont. | +1 | ... | 69''2 \times 51''7 | 32.1 | 0.61 | 57.2 to 72.6 | yes |
| RX Lep | line | +5 | ... | 76''2 \times 47''9 | 10.6 | 2.0 | -37.3 to -121.0; 34.8 to 168.7 | yes |
| RX Lep | cont. | +1 | ... | 67''5 \times 43''8 | 10.7 | 0.4 | -37.3 to -121.0; 34.8 to 168.7 | yes |
| Y UMa ^a | line | +1 | ... | 61''2 \times 52''1 | 51.2 | 1.7 | -41.5 to -15.1; 0.96 to 12.5; 24.2 to 88.6 | yes |
| Y UMa ^a | line | +5 | ... | 72''1 \times 58''1 | 54.9 | 1.7 | -41.5 to -15.1; 0.96 to 12.5; 24.2 to 88.6 | yes |
| Y UMa | cont. | +1 | ... | 61''7 \times 52''4 | 51.4 | 0.18 | -41.5 to -15.1; 0.96 to 12.5; 24.2 to 88.6 | yes |
| R Peg ^a | line | +5 | ... | 62''9 \times 56''9 | 60.9 | 1.7 | -68.9 to -32.8; 35.4 to 57.3 | no |
| R Peg | cont. | +1 | ... | 56''9 \times 67''2 | 67.2 | 0.24 | -68.9 to -32.8; 35.4 to 57.3 | yes |
| Y CVn | line | +1 | ... | 53''6 \times 44''4 | 30.1 | 2.2 | -125.1 to -25.9; 57.8 to 100.3; 124.8 to 150.5 | yes |
| Y CVn | line | +5 | ... | 60''9 \times 48''6 | 32.8 | 2.1 | -125.1 to -25.9; 57.8 to 100.3; 124.8 to 150.5 | yes |
| Y CVn | line | +5 | 2,2 | 106''9 \times 83''5 | 38.6 | 2.6 | -125.1 to -25.9; 57.8 to 100.3; 124.8 to 150.5 | yes |
| Y CVn | cont. | +1 | ... | 53''6 \times 44''4 | 30.0 | 0.48 | -125.1 to -25.9; 57.8 to 100.3; 124.8 to 150.5 | yes |
| V1942 Sgr | line | +5 | ... | 89''5 \times 49''4 | 12.8 | 2.7 | -175.6 to -50.6 | yes |
| V1942 Sgr | cont. | +1 | ... | 79''6 \times 45''7 | 13.8 | 0.48 | -175.6 to -50.6 | yes |
| AFGL 3099 | line | +5 | ... | 63''6 \times 51''9 | 15.6 | 1.7 | 26.7 to 39.5; 52.4 to 65.3 | no |
| AFGL 3099 | cont. | +1 | ... | 56''4 \times 47''9 | 13.8 | 0.45 | 26.7 to 39.5; 52.4 to 65.3 | yes |
| TX Psc | line | +5 | ... | 71''6 \times 48''8 | 5.0 | 2.0 | -130.6 to -25.0; 75.5 to 150.2 | no |
| TX Psc | line | +5 | 2,2,2,2 | 104''2 \times 78''6 | 4.2 | 2.2 | -130.6 to -25.0; 75.5 to 150.2 | no |
| TX Psc | cont. | +1 | ... | 63''6 \times 45''6 | 6.9 | 0.29 | -130.6 to -25.0; 75.5 to 150.2 | yes |

NOTE. — Explanation of columns: (1) target name; (2) indication of whether the image contains line or continuum emission; the continuum images comprise a single spectral channel representing an average of the line-free portions of the band; (3) AIPS robust parameter used in image deconvolution; $\mathcal{R}=+5$ is comparable to natural weighting; (4) Gaussian taper applied in u and v directions, expressed as distance to 30% point of Gaussian in units of kilolambda; (5) FWHM dimensions of synthesized beam; (6) position angle of synthesized beam (measured east from north); (7) rms noise per channel (1σ); (8) LSR velocities of spectral channels used for continuum subtraction (line data) or that were averaged to compute a continuum image; (9) indication of whether or not clean boxes were used during image deconvolution.

^a Data were not Hanning smoothed for the present analysis.

only channels 163 through 448, thus excluding the portion of the band affected by aliasing. We next computed a frequency-averaged channel 0 data set for use in calibrating the frequency-independent complex gains, using a vector average of channels 163 through 448. Following gain calibration, we applied time-dependent frequency shifts to the data to compensate for changes caused by the Earth’s motion during the course of the observations. Lastly, we applied Hanning smoothing in velocity and discarded every other channel, yielding a 256 channel data set with an effective velocity resolution of $\sim 1.3 \text{ km s}^{-1}$.

Issues affecting two stars merit special comment. The data for RX Lep were heavily contaminated by narrow-band radio frequency interference (RFI), necessitating considerable channel-dependent flagging. This resulted in a loss of continuum sensitivity, although fortunately, little RFI was present near the systemic velocity of the star. In the case of V1942 Sgr, a portion of the data taken on 2009 December 7 between 23:07:25 UT and 23:25:46 UT were affected by a bug in the VLA archive software that resulted in the frequencies assigned to each of the spectral channels being mirror reversed relative to their respective channel numbers. The affected data were corrected using the AIPS task FLOPM.

3.1.3. Continuum Subtraction

Prior to imaging the line data for all of the newly observed target stars, we performed a continuum subtraction using a linear fit to the real and imaginary components of the visibilities using the AIPS task UVLIN. The portions of the band that were determined to be line-free channels and were used for these fits are summarized in Column 7 of Table 4. Although the spectral shape of the aliased portion of the continuum as measured toward our continuum calibrators was better approximated by a higher order polynomial, there was generally insufficient continuum signal in our target fields to adequately constrain higher order fits.

3.2. Archival VLA Data

HI data for two stars (AFGL 3099 and IK Tau) were retrieved from the VLA archive. These data were originally taken as part of program AK237 in late 1989 (Principal Investigator: G. Knapp) and to our knowledge are previously unpublished.

The data for IK Tau comprise 32 frequency channels with a channel spacing of 12.2 kHz (2.6 km s^{-1}) after on-line Hanning smoothing, resulting in a total bandwidth of 0.39 MHz ($\sim 82 \text{ km s}^{-1}$) in dual circular polarizations. The AFGL 3099 data comprise 32 frequency channels with a channel spacing of 6.1 kHz (1.3 km s^{-1}) after on-line Hanning smoothing, providing a total bandwidth of 0.195 MHz ($\sim 41 \text{ km s}^{-1}$), also with dual circular polarization. Additional details are provided in Table 2.

We processed both of the archival data sets in a similar manner. After flagging corrupted data, we used a channel 0 data set to calibrate the antenna-based, frequency independent complex gains. The absolute flux level was established using observations of 3C48 (0137+331). We adopted the VLA-determined flux density values for 3C48 from the year 1990, as calculated by the AIPS task SETJY (see Table 3).

Because the 3C48 observations suffered from HI absorption across much of the band, we estimate that the uncertainty in the absolute flux scale for these data may be as high as $\sim 20\%$. This HI absorption also rendered 3C48 unsuitable for use as a bandpass calibrator, hence no bandpass calibration was applied to the archival data. This had minimal impact on the data quality given the narrow bandwidths and the fact that the channels at the band edges had already been discarded by the VLA on-line system.

To create a continuum-subtracted spectral data set for each of the archival sources, we produced a clean image of the continuum using an average of the line-free channels (see Table 4) and then subtracted the clean components from the line data in the visibility domain using the AIPS task UVSUB.

3.3. Imaging the VLA Data

3.3.1. Continuum Data

We produced an image of the 21-cm continuum emission in the field of each target star using the line-free portion of the band (see Table 4). No continuum emission was detected from any of the stars. For the six newly observed target fields (§3.1), we compared the measured flux densities of several continuum sources in each field with values measured from NRAO VLA Sky Survey (NVSS) images (Condon et al. 1998). In all cases we found agreement to within better than 10%. For each target, we also searched for HI absorption against the brightest continuum sources in the field surrounding each star, but in no case did we detect statistically significant absorption.

3.3.2. Line Data

We imaged the VLA HI line data (both new and archival) using the standard AIPS CLEAN deconvolution algorithm. For each target, we produced data cubes using various weighting schemes. The characteristics of those used for the present analysis are summarized in Table 4.

4. RESULTS

In §4.1-4.8 we present the results of our most recent HI imaging study of AGB stars. In six cases we have unambiguously detected HI emission associated with the circumstellar envelopes of the target stars. For the other two targets we derive upper limits on the HI content of their CSEs. We discuss the VLA data for each star and their implications for understanding the mass loss history of each star in the following subsections. In §5 we discuss emerging trends from the entire sample of AGB and related stars that has been imaged in HI to date.

4.1. IK Tauri (IK Tau)

IK Tauri (IK Tau=NML Tau) is an extremely red, large-amplitude Mira variable with an oxygen-rich chemistry and a period of 462 days (Le Bertre 1993). The large amplitude of its variability corresponds to variations in its effective temperature from $\sim 2000 \text{ K}$ to 3000 K (Dyck et al. 1974; Gérard & Le Bertre 2006). Following Le Bertre & Winters (1998), we adopt a distance to the star of 245 pc based on the period-luminosity relation of Feast (1996).

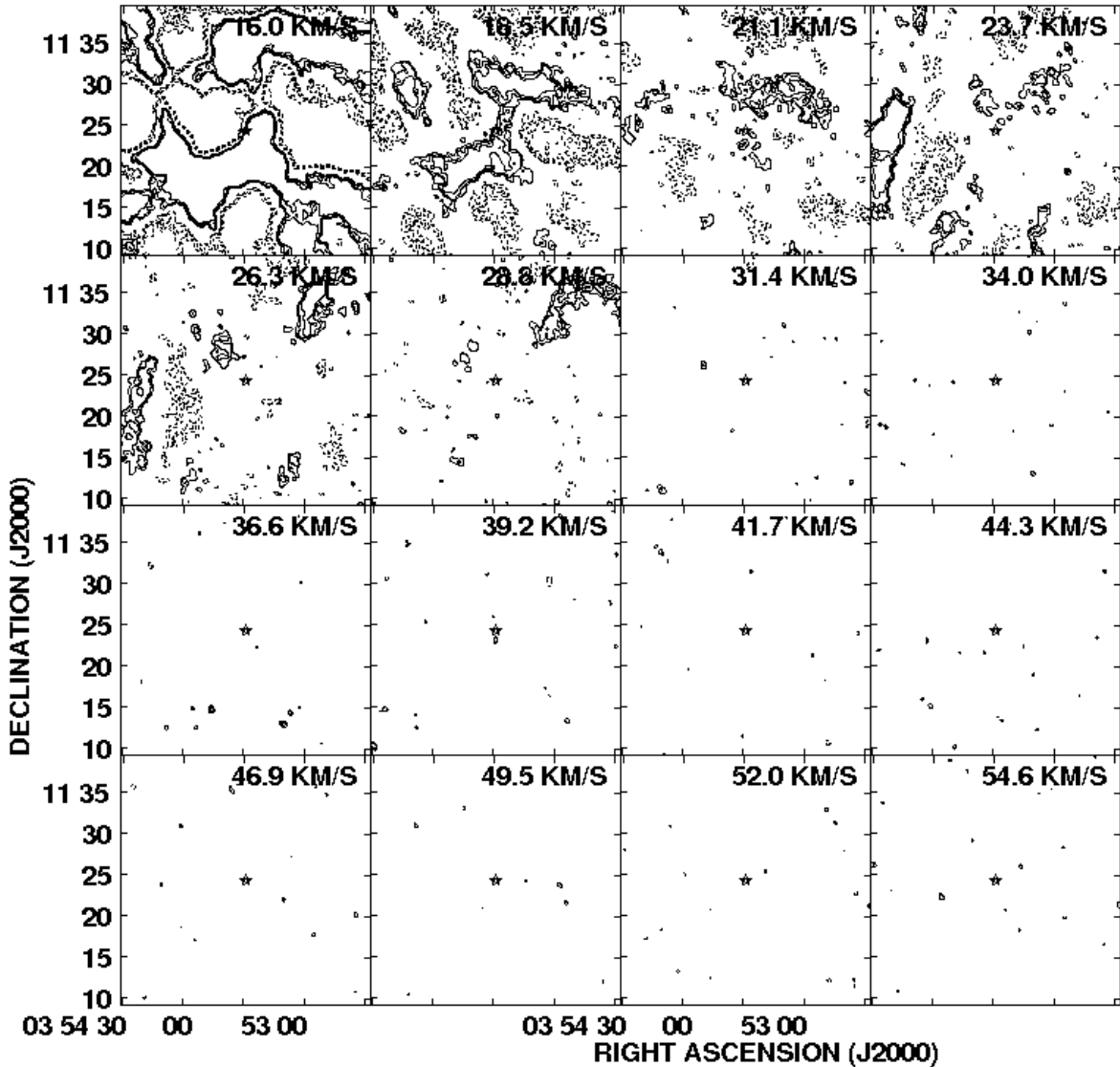


FIG. 1.— H I channel maps bracketing the systemic velocity of IK Tau, derived from naturally weighted VLA data. The spatial resolution is $\sim 69'' \times 52''$. A star symbol indicates the stellar position. Contour levels are $(-8.4, -6, -4.2, -3, 3, \dots, 8.4) \times 1.4 \text{ mJy beam}^{-1}$. The lowest contour is $\sim 3\sigma$ and negative contours are shown as dashed lines. The field-of-view shown is comparable to the VLA primary beam.

IK Tau has been extensively studied at multiple wavelengths and is known to have a rich molecular chemistry (e.g., Milam et al. 2007; Decin et al. 2010; Claussen et al. 2011). Based on CO(1-0) observations, Knapp & Morris (1985) derived a stellar systemic velocity of $V_{*,\text{LSR}} = 34.6 \pm 0.4 \text{ km s}^{-1}$, a mass-loss rate $\dot{M} = 4.2 \times 10^{-6} M_{\odot} \text{ yr}^{-1}$ (scaled to our adopted distance), and an outflow velocity $V_{\text{out}} = 22.0 \pm 0.6 \text{ km s}^{-1}$.

4.1.1. VLA Results for IK Tau

H I channel maps bracketing the systemic velocity of IK Tau are presented in Figure 1. The velocity range shown roughly corresponds to the velocities over which CO emission has been previously detected in the CSE. We find no H I emission features with $\geq 3\sigma$ significance coincident with the stellar position in any of the spectral channels with $V_{\text{LSR}} \geq 23.7 \text{ km s}^{-1}$. For velocities $V_{\text{LSR}} \leq 28.7 \text{ km s}^{-1}$, the data suffer from confusion from line-of-sight Galactic emission that is poorly spatially sampled by the VLA, producing a “mottled” appearance in the channel images. There is no evidence that any of the emission seen at these velocities is related to the CSE of IK Tau.

In Figure 2 we present a spatially integrated H I spectrum derived by summing each plane of the spectral line data cube within a circular aperture of radius $85''$, centered on the star. This aperture was chosen to match the extent of the FIR-emitting shell detected by Cox et al. (2012a; see §4.1.2). Consistent with Figure 1, the resulting H I spectrum is contaminated by Galactic emission at velocities $V_{\text{LSR}} \lesssim 24 \text{ km s}^{-1}$. However, near the stellar systemic velocity, we see marginal evidence for a weak, broad spectral feature that is distinct from the Galactic emission component at lower velocities. Using the spectral data spanning $26.3 \leq V_{\text{LSR}} \leq 72.4 \text{ km s}^{-1}$, we performed a Gaussian fit to this feature. The best-fit Gaussian is overplotted on Figure 2; it has a peak amplitude of $5.6 \pm 1.5 \text{ mJy}$, a velocity centroid of $34.4 \pm 2.3 \text{ km s}^{-1}$, a FWHM velocity width of $17.6 \pm 2.9 \text{ km s}^{-1}$, and a DC offset term of $-0.0013 \pm 0.0008 \text{ Jy}$. The peak amplitude of the Gaussian is roughly 3.5 times the RMS noise in the line-free portion of the spectrum, and the velocity centroid agrees with the stellar systemic velocity derived from CO observations. Despite this, we consider this feature to be of marginal significance given the combination of several factors. The blend with the Galactic

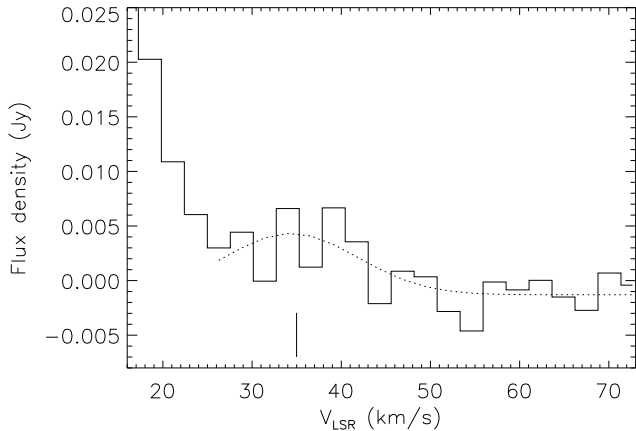


FIG. 2.— Spatially integrated H I spectrum of IK Tau derived from naturally weighted VLA data. The flux density in each channel was derived by integrating within a circular aperture with radius $85''$ (see §4.1.1). The vertical bar indicates the systemic velocity of the star derived from CO observations. Spectral channels with $V_{\text{LSR}} \lesssim 26 \text{ km s}^{-1}$ are contaminated by Galactic emission along the line-of-sight. The dotted line is a Gaussian fit to the data over the velocity range $26.3 \leq V_{\text{LSR}} \leq 72.4 \text{ km s}^{-1}$; we consider this feature to be of marginal significance (see §4.1.1).

emission on the blue edge of the profile makes our Gaussian fit parameters more uncertain than the formal errors would indicate, and the emission giving rise to this possible spectral feature cannot be unambiguously associated with the CSE of IK Tau in any of the individual channel images. Finally, our data cube contains too few line-free channels to permit a robust characterization of the intrinsic instrumental band shape. Deeper H I imaging observations with higher spectral resolution and a wider band could help to overcome these issues.

For the present analysis we use the integral of the Gaussian fit in Figure 2 to provide a $\sim 3\sigma$ upper limit to the integrated H I flux density from the CSE of IK Tau within a $85''$ (0.10 pc) radius of $\int S_{\text{HI}} d\nu < 0.10 \text{ Jy km s}^{-1}$. This translates to an H I mass of $M_{\text{HI}} \leq 1.4 \times 10^{-3} M_{\odot}$ at our adopted distance.

4.1.2. Discussion of IK Tau Results

IK Tau was previously targeted in single-dish H I surveys by Zuckerman et al. (1980) and Gérard & Le Bertre (2006) but was not detected. IK Tau is a challenging target for single-dish studies owing to the strong line-of-sight contamination across the velocity range $V_{\text{LSR}} \approx -40$ to 40 km s^{-1} , which encompasses the stellar systemic velocity (see Gérard & Le Bertre 2006).

With the VLA, we almost entirely filter out the contaminating emission for $V_{\text{LSR}} \geq 31.4 \text{ km s}^{-1}$, allowing us to place more robust constraints on the total amount of atomic hydrogen in the CSE. However, we note some important caveats to the H I mass upper limit that we derived in the previous section. First, the rather coarse spectral resolution employed for the IK Tau observations ($\sim 2.6 \text{ km s}^{-1}$) may have diminished our sensitivity to emission components with narrow velocity widths ($\Delta V \sim 1 \text{ km s}^{-1}$). Such components may be present even when the global (spatially integrated) H I line width is several times larger. A second caveat is that the gas temperature in CSEs is expected to depend strongly on

the mass-loss rate (Jura et al. 1988; Sahai 1990), with cooler CSE temperatures expected for stars with higher values of \dot{M} . Thus a significant fraction of the stellar wind may be molecular (Glassgold & Huggins 1983) and most of the remaining fraction of the atomic hydrogen in the CSE of IK Tau may be simply too cold to detect in emission. This argument may also be relevant to the case of AFGL 3099 (§4.7), another star that remains undetected in H I emission despite its high mass loss rate.

Recent *Herschel* imaging at $70\mu\text{m}$ and $160\mu\text{m}$ by Cox et al. (2012a) revealed that IK Tau is surrounded by extended infrared emission with radius $\sim 85''$ that appears to be consistent with a bow shock and related structures. The total mass of the CSE estimated from these FIR measurements is $\sim 0.037 M_{\odot}$ (assuming a gas-to-dust ratio of 200; Cox et al. 2012b), roughly 20 times higher than the upper limit we derive from our H I measurements (after scaling by a factor of 1.4 to account for the mass of helium).

4.2. RX Leporis (RX Lep)

RX Leporis (RX Lep) is an oxygen-rich AGB star that was reclassified by Samus et al. (2004) from an irregular variable to a semi-regular variable of type SRb. We adopt here a distance of 149 pc based on the *Hipparcos* parallax of $6.71 \pm 0.44 \text{ mas}$ (van Leeuwen 2007).

Libert et al. (2008) presented CO(2-1) observations for RX Lep from which they derived a stellar systemic velocity of $V_{\star, \text{LSR}} = 28.9 \pm 0.1 \text{ km s}^{-1}$, a mass-loss rate $\dot{M} \approx 2.0 \times 10^{-7} M_{\odot} \text{ yr}^{-1}$ (scaled to our adopted distance), and an outflow velocity for the wind $V_{\text{out}} = 4.2 \pm 0.1 \text{ km s}^{-1}$. The proper motions measured by *Hipparcos* are $31.76 \pm 0.58 \text{ mas yr}^{-1}$ in right ascension and $56.93 \pm 0.50 \text{ mas yr}^{-1}$ in declination, implying a peculiar space motion of $V_{\text{space}} \approx 56.6 \text{ km s}^{-1}$ along a position angle of $24^{\circ}6$ (see Table 5).

RX Lep has an effective temperature of $\sim 3300 \text{ K}$ (Dumm & Schild 1998), and using the bolometric correction from Le Bertre et al. (2001), its luminosity is $5300 L_{\odot}$ at our adopted distance (Libert et al. 2008). The initial mass of RX Lep is believed to be in the range $2.5\text{--}4.0 M_{\odot}$ (Mennessier et al. 2001). As discussed further below, RX Lep was previously detected in H I by Libert et al. (2008) using single-dish observations from the NRT.

Technetium lines have not been detected in RX Lep (Little et al. 1987; Lebzelter & Hron 1999), implying that either RX Lep is on the early AGB (E-AGB) or that it is still near the beginning of the thermal pulsing (TP) AGB phase and has not yet undergone dredge-up (e.g., Straniero et al. 1997). The mass-loss rate and wind outflow speed for the star are also consistent with values expected near the beginning of the TP-AGB (Vassiliadis & Wood 1993). As described below (§4.2.2), placement of RX Lep near the start of the TP-AGB is further supported by our new H I observations.

4.2.1. VLA Results for RX Lep

H I channel maps for RX Lep derived from our VLA data are presented in Figure 3 and an H I total intensity map derived from the same data is shown in Figure 4. Together these figures reveal the detection of an extended H I emission nebula surrounding the position of RX Lep

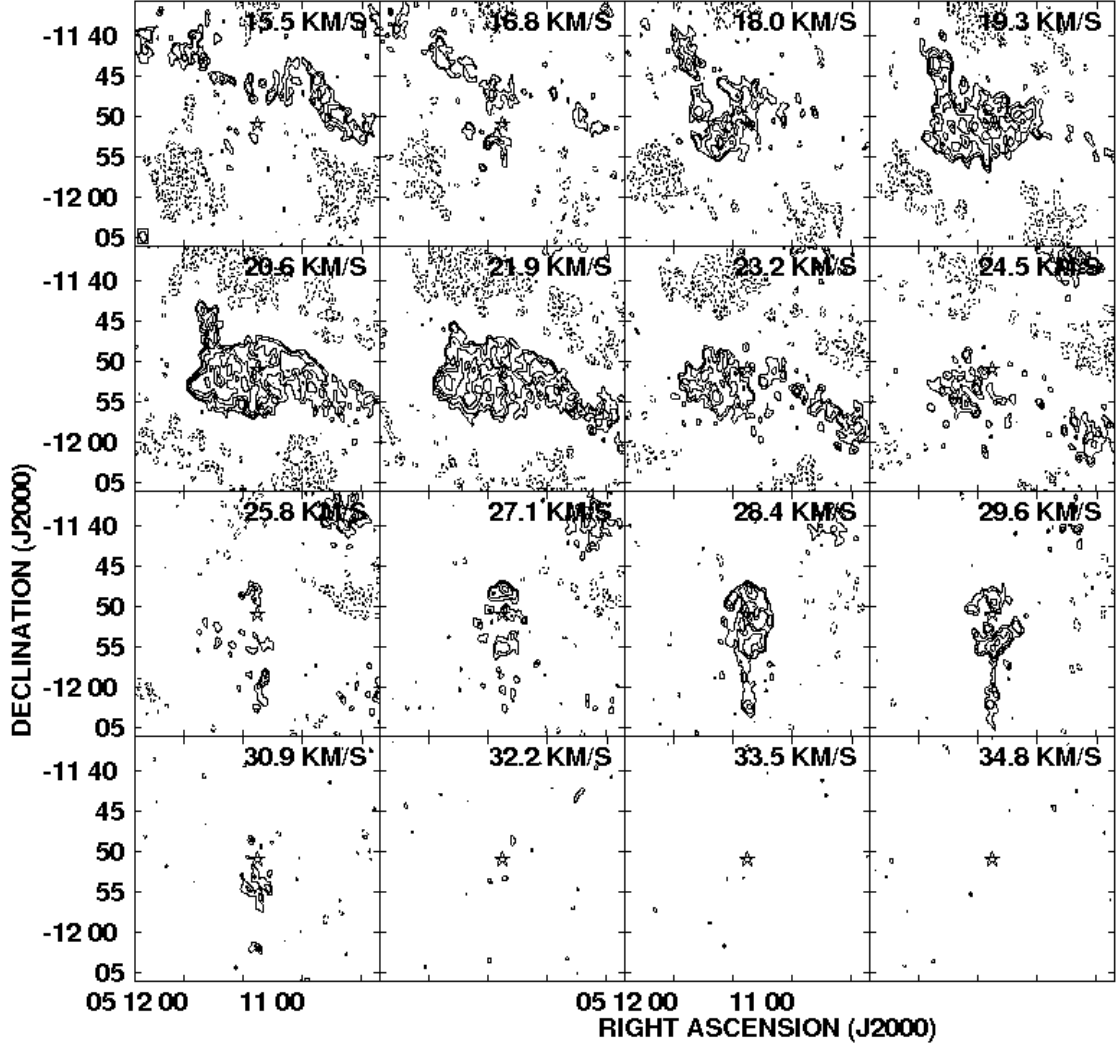


FIG. 3.— HI channel maps bracketing the systemic velocity of RX Lep, derived from naturally weighted VLA data. The spatial resolution is $\sim 76'' \times 48''$. A star symbol indicates the stellar position. Contour levels are $(-6[\text{absent}], -4.2, -3, 3, 4.2, 6, 8.4, 12) \times 2.0 \text{ mJy beam}^{-1}$. The lowest contour is $\sim 3\sigma$. The channels shown correspond to the range of LSR velocities over which CO(2-1) emission was detected by Libert et al. 2008. The field-of-view displayed is comparable to the VLA primary beam.

whose morphology and velocity distribution imply an unambiguous association with the star. The HI emission is most prevalent in the two velocity channels that bracket the stellar systemic velocity ($V_{\text{LSR}} = 28.4 \text{ km s}^{-1}$ and 29.6 km s^{-1}), but the emission can be traced from 25.8 km s^{-1} to 32.2 km s^{-1} .

Additional HI emission is also detected near the position of RX Lep in velocity channels from 16.8 km s^{-1} to 24.5 km s^{-1} . However, the peak intensity of this emission is centered a few arcminutes southeast of the star, and it reaches its peak spatially-integrated intensity ($\sim 1.2 \text{ Jy}$) at $V_{\text{LSR}} = 20.6 \text{ km s}^{-1}$ (see Figure 5). This is outside the velocity range over which molecular line emission has been detected in the CSE of RX Lep. Further, the borders of this emission are not well defined; at low surface brightness levels they begin to blend with large-scale bands of positive and negative emission that stretch across the corresponding channel images. Together these properties suggest that this emission is not related to the CSE of RX Lep, but instead is part of an interstellar cloud or cloud complex along the line-of-sight

that is spatially extended and poorly spatially sampled by the VLA. This interpretation is consistent with evidence for confusion over this velocity range seen in the single-dish spectra of Libert et al. (2008). Based on similar arguments, the HI emission seen northwest of RX Lep (near $\alpha_{\text{J2000}} = 05^{\text{h}}10^{\text{m}}39^{\text{s}}$, $\delta_{\text{J2000}} = -11^{\circ}39'16''$) is also unlikely to be related to the star.

A defining characteristic of the HI emission associated with RX Lep is its “cracked egg” morphology. As seen in Figure 4, the velocity-integrated emission exhibits a distinctly ovate shape with its semi-major axis aligned north-south. The extent of the “egg” is ~ 6.7 (0.30 pc) east-west by ~ 9.8 (0.42 pc) north-south. The star itself lies $\sim 30''$ north of the geometric center of the egg. The HI distribution across the egg appears clumpy, and Figure 4 reveals two enhancements in the HI column density at its north and south “poles”. In contrast, a pronounced dearth of emission is observed along the egg’s east-west equator.

Another striking feature of RX Lep’s circumstellar HI emission is the presence of a narrow, highly extended (\sim

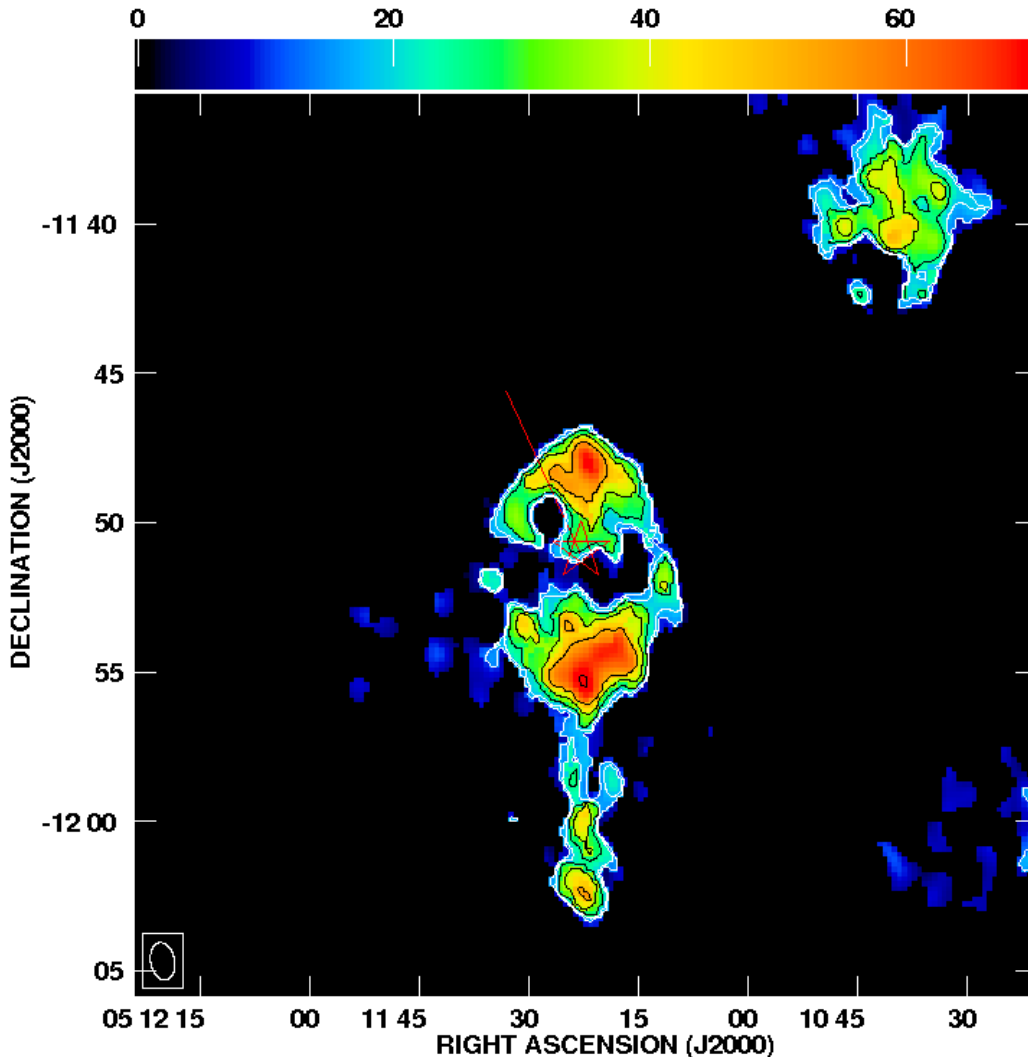


FIG. 4.— HI total intensity map of RX Lep derived from naturally weighted data. The spatial resolution is $\sim 76'' \times 48''$. The map was constructed from emission spanning LSR velocities 25.8 to 32.2 km s^{-1} . The red line indicates the direction of space motion of the star. Intensity levels are 0 to 70 $\text{Jy beam}^{-1} \text{m s}^{-1}$ and contour levels are $(1.8, 3.5, 3.5, 7, 10) \times 7.3$ $\text{Jy beam}^{-1} \text{m s}^{-1}$. To minimize noise in the map, data at a given point were blanked if they did not exceed a 2.5σ threshold after smoothing by a factor of three spatially and spectrally.

$7'$ or 0.30 pc long) tail of emission that stretches almost due south of the star. As seen in Figure 4, the tail includes several compact knots of emission. There are also hints that the tail may have a kinked or corkscrew shape, although this cannot be confirmed from the present data.

Two versions of the spatially integrated HI spectrum of RX Lep are shown in Figure 5. The first (shown as a solid histogram) is derived by integrating the emission within each spectral channel within a fixed aperture. Because of the presence of confusion blueward of the stellar systemic velocity, we have also derived a second spectrum (plotted as a dashed histogram) by summing the emission in irregularly shaped “blotches” surrounding the stellar position in each channel over the velocity range at which circumstellar CO emission has been detected. The blotch peripheries were defined by 3σ contours and encompass the emission comprising the tail and shell structures visible in Figure 4.

Based on a two-component Gaussian fit to the “fixed aperture” spectrum in Figure 5, we derive an HI line centroid for the RX Lep emission of $V_{\text{LSR}} = 28.4 \pm$

0.1 km s^{-1} , in good agreement with the value determined from CO observations. From our Gaussian fits we also find a peak flux density of 0.58 ± 0.02 Jy and a FWHM HI linewidth $\Delta V = 5.0 \pm 0.3$ km s^{-1} . The latter is larger than the value of 3.8 ± 0.1 km s^{-1} previously reported by Libert et al. (2008). From our fit we compute an integrated HI flux density for the CSE of RX Lep of $\int S_\nu dv = 3.09 \pm 0.22$ Jy km s^{-1} . Alternatively, using the “blotch” spectrum, we measure $\int S_\nu dv = 2.77 \pm 0.04$ Jy km s^{-1} . Because the uncertainty is dominated by the systemic uncertainties in determining the intrinsic line profile shape in the presence of confusion, we adopt as our best estimate a mean of our two measurements: $\int S_\nu dv = 2.93 \pm 0.22$ Jy km s^{-1} . This translates to an HI mass of $M_{\text{HI}} \approx 0.015 M_\odot$. This is roughly 2.5 times larger than measured by Libert et al. (2008) from single-dish mapping. The reason for this discrepancy is unclear, although part of the difference may arise from the manner in which the RX Lep line emission was deblended from the neighboring Galactic signal. Libert et al. used polynomial baseline fits, while here we use spatial segre-

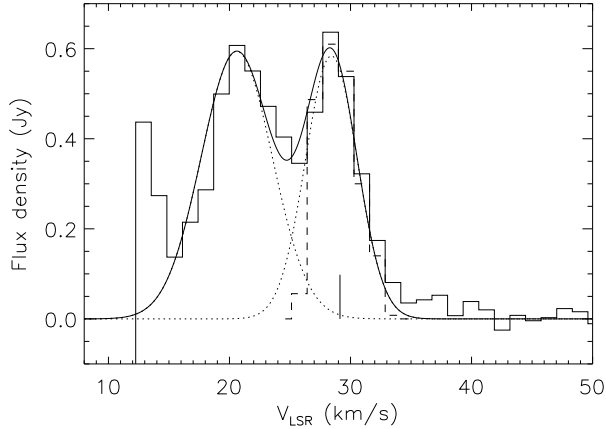


FIG. 5.— Spatially integrated HI spectrum of RX Lep. The stellar systemic velocity derived from molecular line observations is indicated by a vertical bar. The thick histogram shows a spectrum derived from naturally weighted VLA data (after correction for primary beam attenuation) by integrating the emission in each velocity channel within a 7.5×17.8 aperture centered at $\alpha_{J2000} = 05^{\text{h}} 11^{\text{m}} 22.5^{\text{s}}$, $\delta_{J2000} = -11^{\circ} 55' 01.7''$. The blue edge of the RX Lep profile is blended with Galactic emission. The dotted lines and thin solid line show the results of a two-Gaussian fit to the blended profile. The spectrum plotted as a dashed histogram was derived by summing the emission within irregularly shaped blotches whose outer boundaries were defined by 3σ intensity contours.

gation of the emission and Gaussian line decompositions to disentangle the signals. We have verified through measurements of continuum sources in the field (§3.3.1) that the discrepancy does not result from an uncertainty in the amplitude scale of the VLA data. The distinctive morphology of the circumstellar HI emission seen in Figure 4 also seems to rule out significant contamination of the VLA flux density measurements from line-of-sight emission.

4.2.2. Discussion of RX Lep Results

Based on single-dish mapping and numerical modeling, Libert et al. (2008) deduced that RX Lep is surrounded by a detached HI shell comprising material from the stellar wind, augmented by gas swept up from the local ISM. They also found indications of elongation of the emission along the direction of space motion of the star. Our VLA observations of RX Lep confirm these general features of the HI distribution. In addition, the wealth of additional detail revealed by our imaging data provides important new clues on the evolutionary history of the star and its interaction with the local environment.

To first order, the morphological properties of the HI emission surrounding RX Lep appear to be significantly influenced by the interaction between the star and its local interstellar environment. This is not surprising given the moderately high space velocity of the star ($V_{\text{space}} \approx 57 \text{ km s}^{-1}$; Table 5). Manifestations of this interaction include the elongation of its HI shell, the displacement of the star from the center of this shell, and the extended tail of gas trailing to the south. We now discuss each of these properties in turn.

The north-south elongation of RX Lep’s egg-shaped shell aligns roughly with the space motion vector that we have computed for the star ($\text{PA} \approx 25^\circ$). This small misalignment between the two may be due to a bulk

ISM flow in the region, directed roughly perpendicular to the trajectory of the star. Evidence for similar local flows has recently been inferred from observations of other evolved stars (Ueta 2008; Ueta et al. 2010; Wareing 2012; Menten et al. 2012; see also §4.8.2).

As noted above, RX Lep is displaced by $\sim 30''$ (0.022 pc) north of the geometric center of its HI shell. If we adopt half of the FWHM linewidth of the HI spectral profile as a measure of the outflow velocity (i.e., $V_{\text{out}} \approx 2.6 \text{ km s}^{-1}$) and a mean shell radius of 0.15 pc, the dynamical crossing time for the shell is $\sim 56,000$ yr. If RX Lep has traveled from the shell center to its present position in this amount of time, its implied rate of motion in declination would be only $\sim 0.5 \text{ mas yr}^{-1}$ —significantly less than its *Hipparcos* proper motion along this direction ($56.93 \text{ mas yr}^{-1}$). This implies that the HI shell is not “free-floating”, but rather that it is being dragged along with the moving star. Furthermore, this suggests that the displacement of the star from the shell center originates primarily from the lower pressure encountered in the direction opposite the motion of the star compared with in the leading direction.

As described below, our new data support the possibility that RX Lep has only recently begun a new phase of mass-loss. If true, this may help to explain another prominent feature of its shell: the dearth of emission along its equatorial region. Villaver et al. (2012) point out that for mass-losing stars moving supersonically through the ISM, an ensuing pressure drop interior to an existing shell that occurs in-between mass-loss episodes may trigger instabilities, leading it to break apart. Villaver et al. also note that as the wind from a new mass loss episode propagates through previously ejected material, shock regions are expected to develop. We speculate that the break in RX Lep’s shell may be linked with such shocks or instabilities.

Extended gaseous wakes resembling cometary-like tails have now been detected in HI emission toward several AGB stars, trailing their motions through space (Matthews & Reid 2007; Matthews et al. 2008, 2011b; see also §4.8). However, none of the tails discovered to date has been as highly collimated as the one seen trailing RX Lep. It is likely that this narrow tail results from the confluence of the relatively early evolutionary status of RX Lep compared with other stars imaged in HI to date, coupled with its relatively high space velocity and the star’s location near the Galactic disk (see Table 5). In general, higher stellar space velocities allow more efficient deflection of mass loss debris behind the star to form a trailing wake (e.g., Villaver et al. 2012), while higher local ISM densities (as are expected near the Galactic plane) produce greater external pressure, leading to greater collimation (e.g., Wareing 2012). We note however that in simulations, the adopted cooling function and the temperature assumed for the stellar wind will also influence the resulting properties of the cometary tail.

A counterpart to the RX Lep tail is also visible in *IRAS* $60\mu\text{m}$ and $100\mu\text{m}$ images of the star, extending $\sim 12'$ to the south (see Figure 9 of Libert et al. 2008). While Libert et al. cautioned that this structure could be an artifact resulting from the north-south scanning direction of the *IRAS* satellite, our HI imaging now provides cor-

roborating evidence that this feature is likely real. The poor angular resolution of the *IRAS* data preclude a detailed comparison between the FIR and H I emission, but the data are consistent with the two tracers having comparable linear extents.

To account for their original H I observations of RX Lep, Libert et al. (2008) proposed a simple model comprising a freely expanding wind with a constant outflow speed and mass loss rate, interior to some radius, r_1 , at which a termination shock occurs owing to the collision between the freely expanding stellar wind and the surrounding medium. Exterior to r_1 , the wind sweeps up additional matter from its surroundings and is decelerated and compressed as a result of this interaction, leading to the formation of a detached shell.

Incorporating new constraints derived from our VLA measurements together with the molecular wind parameters from Libert et al. (2008), we have computed a revised version of the Libert et al. model. Details are described in Appendix A. We recognize that our model is an oversimplification, since it assumes spherical symmetry and does not account for the space motion of RX Lep. The stellar motion will result in a higher effective pressure on the leading edge of its H I shell and a pressure in the trailing direction that is lower than the average ISM pressure. These effects will impart an elongation to the H I shell (as well as a reduction of the size of the shell in the leading direction) and lead to the formation of a trailing wake. Despite these limitations, our model is able to provide a satisfactory fit to the globally averaged H I line profile of RX Lep (Figure 28a) and supplies a first order estimate of the duration of mass loss time history for this star. Based on our best-fit model (Table A1), we find a mass loss timescale of $\sim 90,000$ yr. Our derived age is consistent with the hypothesis that RX Lep has begun its life as a TP-AGB star only relatively recently.

4.3. *Y Ursae Majoris (Y UMa)*

Y Ursae Majoris (Y UMa) is a semi-regular variable with an oxygen-rich chemistry. Its spectral type (M7II-III) is later than the vast majority of semi-regular variables (Dickinson & Dinger 1982). Kiss et al. (1999) found this star to have a triply periodic variability with a dominant period of 162 days, plus additional modulations on time scales of 315 and 324 days. (Another star in our current sample, the carbon-rich Y CVn, is also a triply periodic semi-regular variable; see §4.5). Y UMa has an effective temperature of ~ 3100 K based on the temperature scale of normal giants of type later than M6 (Perrin et al. 2004). We adopt a distance to the star of 385 pc based on the *Hipparcos* parallax of 2.60 ± 0.59 mas (van Leeuwen 2007).

Y UMa was observed in the CO(2-1) line by Knapp et al. (1998). Based on those data, the authors derived a stellar systemic velocity of $V_{*,\text{LSR}} = 19.0 \pm 0.5$ km s $^{-1}$, a wind outflow speed of $V_{\text{out}} = 5.4 \pm 0.6$ km s $^{-1}$, and a mass-loss rate of $\dot{M} = 2.6 \times 10^{-7} M_{\odot} \text{ yr}^{-1}$ (scaled to our adopted distance). The systemic velocity and outflow velocity are in agreement with those derived from the thermal SiO $v=0$ $J=2-1$ and $J=3-2$ lines detected by González Delgado et al. (2003). The *Hipparcos* proper motions of -4.95 ± 0.53 mas yr $^{-1}$ in right ascension and 2.05 ± 0.50 mas yr $^{-1}$ in declination imply a peculiar space

motion of 19.2 km s $^{-1}$ along a position angle of 57°1 (Table 5).

4.3.1. *VLA Results for Y UMa*

We present H I channel maps from our naturally weighted VLA data cube in Figure 6. Emission is detected at the stellar position in the channel centered at $V_{\text{LSR}} = 19.0$ km s $^{-1}$ (corresponding to the stellar systemic velocity) and in several surrounding channels. Indeed, we detect H I emission at $\geq 3\sigma$ that appears to be associated with the CSE over the velocity range 13.8 to 22.9 km s $^{-1}$. The velocity extent of the H I emission is thus nearly identical to that of the CO(2-1) emission detected by Knapp et al. (1998). Redward of the stellar velocity ($V_{\text{LSR}} \geq 19.6$ km s $^{-1}$), the detected emission is weak and unresolved and lies at or near the stellar position. However, for velocities $V_{\text{LSR}} \leq 19.0$ km s $^{-1}$, the emission is clearly extended, and there are hints of a bifurcation in the emission structure. This is most clearly seen in the 15.8 km s $^{-1}$ and 16.4 km s $^{-1}$ velocity channels.

In Figure 7 we present an H I total intensity map of Y UMa. This map was produced from the robust +1 weighted data (Table 4) to highlight the clumpy nature of the emission and the existence of a “notch” in the CSE to the northeast of the star, along a position angle of $\sim 60^\circ$. This position angle closely matches that of the direction of space motion of the star (Table 5). An analogous feature, also along the direction of space motion, is seen in the CSE of Y CVn (Figure 15; §4.5.2). One can also see from Figure 7 that the peak H I column density in the CSE of Y UMa is displaced by $\sim 20''$ (~ 0.037 pc) to the northeast of the stellar position.

The morphology of the H I emission surrounding Y UMa suggests that the emission in the northwestern part of the CSE has been severely distorted by its interaction with the surrounding medium or other external forces. The result is a CSE with a distinctly non-spherical shape, including a small plume of gas extending from the western edge of the H I nebula. Despite this distortion, we measure nearly equal H I masses on either side of the bisector running along the position angle of the space motion. Including the extended plume, the maximum H I extent of Y UMa is $\sim 6/8$ (0.76 pc).

Figure 8 shows an H I velocity field for Y UMa, again derived from the robust +1 data. The H I velocity field is clearly dominated by emission blueward of the stellar systemic velocity. Interestingly, the velocity pattern exhibits a 180-degree rotational symmetry, but with the symmetry point displaced by $\sim 1'$ northeast of the stellar position. This displacement is along the space motion vector of the star. One can also see in Figure 8 evidence for systematic velocity gradients across the CSE; along $\text{PA} \approx 70^\circ$ and 250° , the emission becomes systematically redshifted with increasing distance from the star, while along $\text{PA} \approx 110^\circ$ and $\approx 350^\circ$, the emission becomes systematically blueshifted with increasing distance. These angles match the bifurcation visible in the channel images in Figure 6. Y UMa is the only star imaged in H I to date to show these types of features in the velocity field, and their origin and interpretation are presently unclear.

A spatially integrated H I spectrum of Y UMa is presented in Figure 9. As expected from the emission distribution seen in Figure 7, the peak integrated flux den-

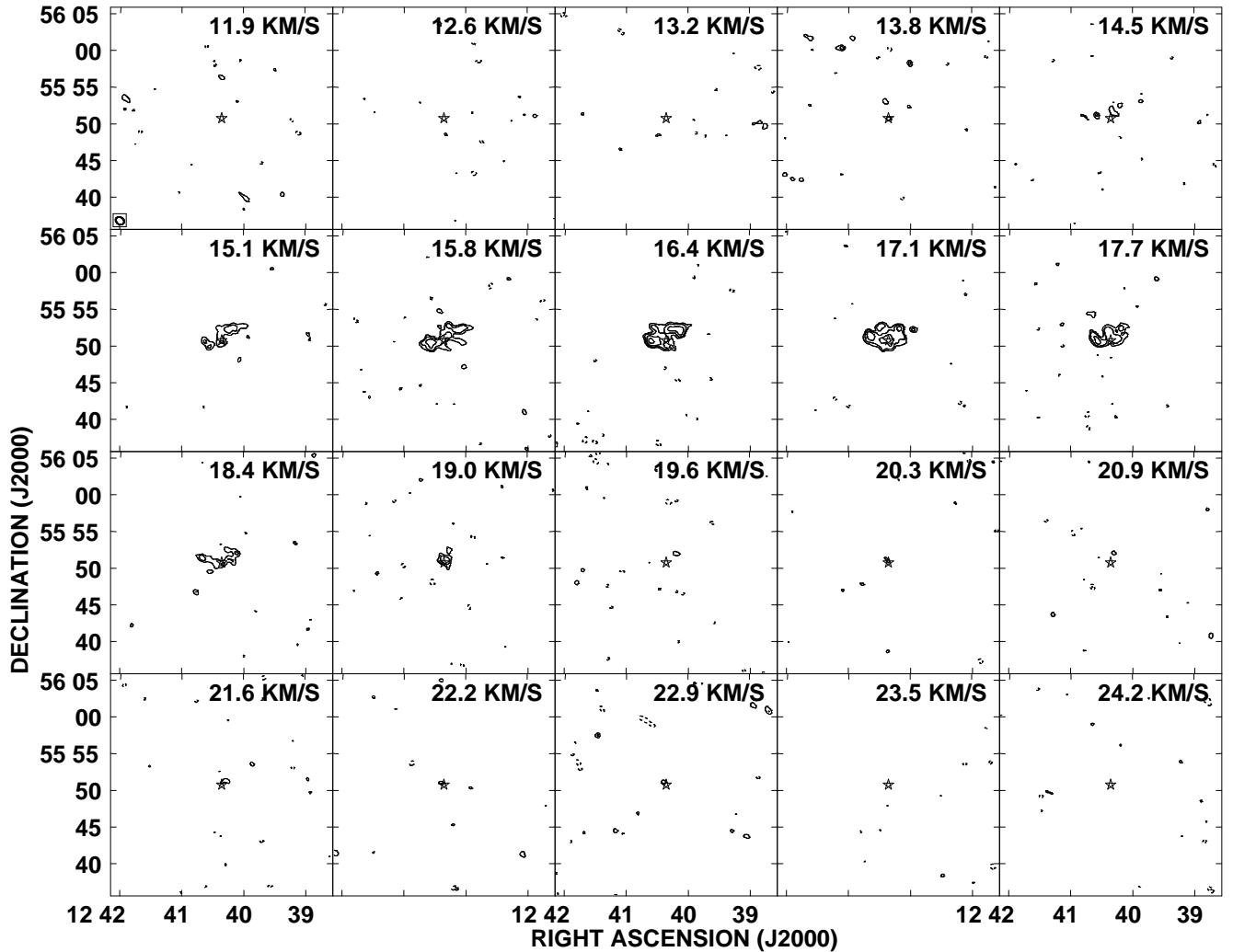


FIG. 6.— HI channel maps bracketing the systemic velocity of Y UMa, derived from naturally weighted VLA data. The spatial resolution is $\sim 72'' \times 58''$. A star symbol indicates the stellar position. Contour levels are $(-4.2, -3.3, 4.2, 6, 8.4) \times 1.7 \text{ mJy beam}^{-1}$. The lowest contour is $\sim 3\sigma$. The field-of-view shown is comparable to the VLA primary beam.

sity occurs blueward of the stellar systemic velocity. The spectrum has a two-component structure similar to what was reported previously by Gérard & Le Bertre (2006) based on NRT spectroscopy. Using a two-component Gaussian fit to the VLA spectrum, we find a narrow component with a peak flux density of $0.10 \pm 0.01 \text{ Jy}$ and a FWHM line width of $3.2 \pm 0.4 \text{ km s}^{-1}$, centered at $V_{\text{LSR}} = 16.4 \pm 0.2 \text{ km s}^{-1}$, and a weaker, broad component centered at $17.2 \pm 0.8 \text{ km s}^{-1}$ with a peak flux density $0.03 \pm 0.01 \text{ Jy}$ and a FWHM line width of $9.2 \pm 2.3 \text{ km s}^{-1}$. Both components are blueshifted relative to the systematic velocity of the star as determined from CO observations, although the broad component matches the systemic velocity determined from near infrared lines by Lebzelter & Hinkle (2002) ($V_* = 17.7 \pm 0.5 \text{ km s}^{-1}$).

The peak HI flux density measured with the VLA is $\sim 40\%$ higher than the original NRT measurement by Gérard & Le Bertre (2006). However, a new analysis using higher quality NRT data now shows good agreement between the VLA and NRT measurements, although the NRT data hint that the source size may be more ex-

tended than we observe with the VLA (up to $16'$; Gérard & Le Bertre, in prep.).

Based on our Gaussian fit to the spectrum in Figure 9, we measure an integrated HI flux density associated with the CSE of Y UMa of $\int S_{\text{HI}} d\nu = 0.63 \pm 0.13 \text{ Jy km s}^{-1}$, translating to a total HI mass $M_{\text{HI}} \approx 0.022 M_{\odot}$. Although the double Gaussian provides a good fit to the line profile, the peak of the composite Gaussian profile is shifted by $\sim 0.6 \text{ km s}^{-1}$ to the blue of the observed line peak, and there are hints of residual emission in the blue wing of the line.

4.3.2. Discussion of Y UMa Results

From Figure 6 one sees that the emission giving rise to the broader of the two HI line components in Figure 9 arises from spatially compact emission lying at or near the position of the star, while the narrower velocity component comes from material that is more spatially extended. This suggests that the broad line component may be linked with the freely expanding wind detected at small radii through its CO and SiO emission. This hypothesis is consistent with the respective widths of the HI and molecular lines. If we approxi-

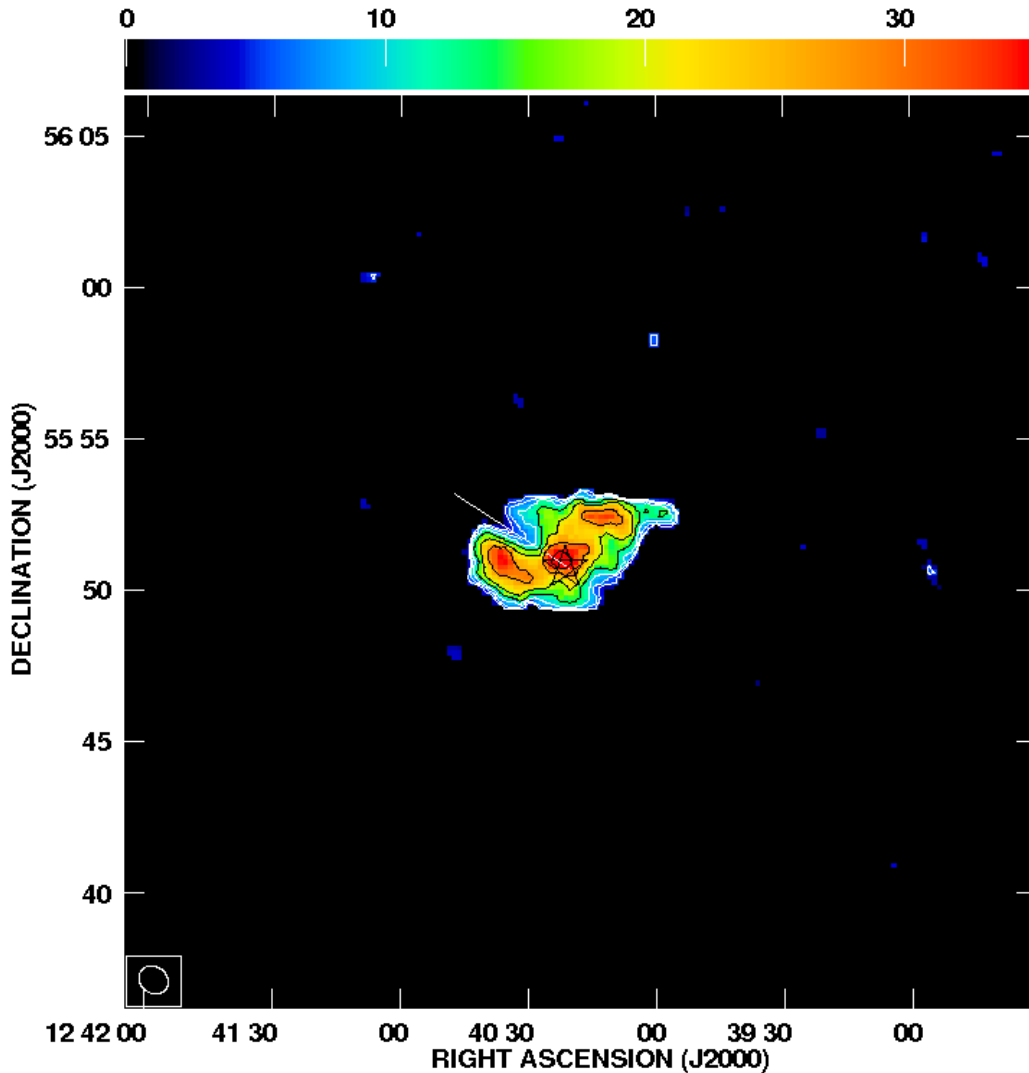


FIG. 7.— HI total intensity map of Y UMa derived from data with robust +1 weighting. The spatial resolution is $\sim 61'' \times 52''$. The map was constructed from emission spanning LSR velocities 13.8 to 22.9 km s^{-1} . Contour levels are $(1, 1.4, 2, 2.8, 4, 5.6, 8) \times 4.8 \text{ Jy beam}^{-1} \text{ m s}^{-1}$ and the intensity levels are 0 to 35 $\text{Jy beam}^{-1} \text{ m s}^{-1}$. To minimize noise in the map, data at a given point were blanked if they did not exceed a 1.8σ threshold after smoothing by a factor of three spatially and spectrally. A star symbol indicates the stellar position and white line indicates the direction of space motion. The field-of-view shown is comparable to the VLA primary beam.

mate the molecular linewidth as twice the CO outflow velocity ($\sim 10.8 \pm 0.6 \text{ km s}^{-1}$), this matches the FWHM of the broad HI line, although the line centroids differ by $\sim 2\text{--}3 \text{ km s}^{-1}$. Higher resolution HI imaging together with CO imaging of Y UMa would be of interest for more thoroughly investigating this link.

Y UMa was reported by Young et al. (1993a) to be an extended infrared source with a diameter of $7'.6$ at $60\mu\text{m}$. The extended nature of the FIR emission is confirmed by an archival *ISO* $65\mu\text{m}$ image shown in Figure 10. To our knowledge, these *ISO* data have not been published previously. The observations were executed on 1996 October 18 as part of program 33700231 (Principal Investigator: J. Gurtler). We have downloaded the oversampled map as a “Standard Processed Data” FITS file from the *ISO* data archive.⁸ The original image had a field-of-view of $687'' \times 687''$ and a pixel size of $15''.0$. For display pur-

poses, the image was resampled to a pixel size of $10''$ to match the VLA data.

While the FIR emission appears to have a roughly comparable spatial extent as the HI emission detected with the VLA, the two do not correspond closely in detail. For example, the FIR emission appears elongated along a northeast/southwest direction, extending further to the southwest than the HI emission. Conversely, we see that there is little or no FIR emission underlying the northwestern portion of the HI nebula, including the ridge of enhanced HI column density and the weaker plume extending from the northern edge. Since in principle, whatever process is responsible for the distortion on the northwestern side of the CSE and creation of the “plume” observed in HI should have acted on both the HI and the FIR-emitting (presumably dusty) material, this suggests that either the atomic hydrogen is intrinsically more extended than the dust or that dust grains were destroyed during this process. The absence of any strong correla-

⁸ The archive is hosted by the European Space Agency at <http://iso.esac.esa.int/ida>.

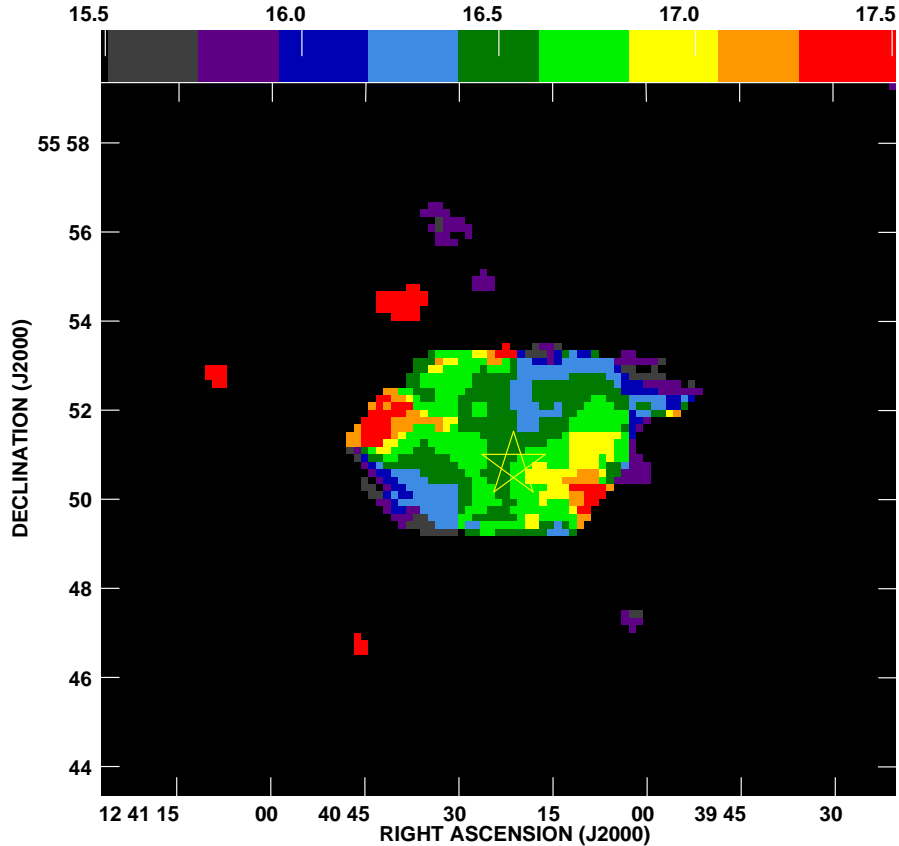


FIG. 8.— HI velocity field of Y UMa derived from naturally weighted data. The spatial resolution is $\sim 72'' \times 58''$. The intensity scale indicates LSR radial velocity in km s^{-1} .

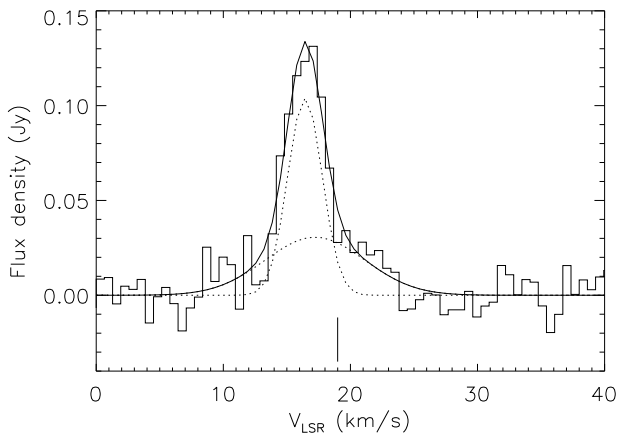


FIG. 9.— Spatially integrated HI spectrum of Y UMa. The spectrum was derived from naturally weighted VLA data (after correction for primary beam attenuation) by integrating the emission in each velocity channel within a 8.5×7.0 aperture centered at $\alpha_{\text{J2000}} = 12^{\text{h}} 40^{\text{m}} 20.1^{\text{s}}$, $\delta_{\text{J2000}} = 55^{\circ} 51' 27.6''$. The dotted curves and thin solid curve show, respectively, a two-component Gaussian fit to the line profile and the sum of the two components. The vertical bar indicates the stellar systemic velocity as determined from CO observations.

tions between the atomic gas and the FIR emission may also imply that the dust grains are not uniformly mixed throughout the CSE. Simulations by van Marle et al. (2011) have shown that such non-uniform mixing is expected for the largest CSE grains (with radii $\gtrsim 0.105 \mu\text{m}$).

As in the case of RX Lep (§4.2.2), we have derived a simple model for the HI emission of Y UMa under the assumption that it arises from an outflowing wind that has been abruptly slowed at a termination shock where it meets the surrounding ISM, resulting in the formation of a detached shell (see Appendix A and Table A1 for details). Despite the observed distortions of the Y UMa HI shell, our simple model provides a reasonable fit to the global (spatially averaged) HI line profile, including its two-component structure (Figure 28b). Using this model we estimate a total duration of the mass loss history of the star of $\sim 1.2 \times 10^5$ yr.

4.4. *R Pegasi (R Peg)*

R Pegasi (R Peg) is an oxygen-rich Mira variable with a mean spectral type M7e and a pulsation period of 378 days (Jura & Kleinmann 1992; Whitelock et al. 2008). The effective temperature of R Peg is known to vary significantly throughout its pulsation cycle; van Belle et al. (1996) measured $T_{\text{eff}} = 2333 \pm 100$ K at minimum and 2881 ± 153 K at maximum.

We adopt a distance to R Peg of 400 pc based on the period-luminosity relation for Miras derived by Jura & Kleinmann (1992), although we note that the study of Whitelock et al. (2008) yielded a value $\sim 25\%$ higher (490 pc). The *Hipparcos* parallax for this star (2.61 ± 2.03 mas yr^{-1} ; Knapp et al. 2003) is too uncertain to provide any additional meaningful constraints on the distance.

Based on the CO(2-1) observations of Winters et

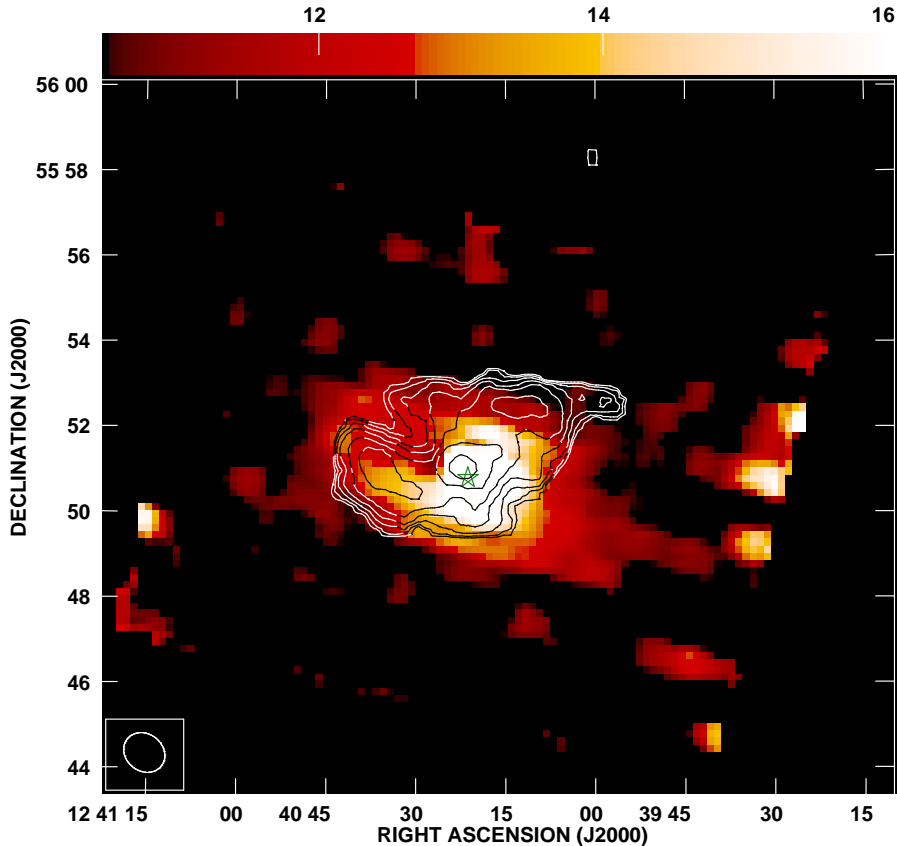


FIG. 10.— H I total intensity contours (same as in Figure 7) overlaid on an *ISO* 65 μ m image of Y UMa. The brightness units of the *ISO* image are MJy steradian $^{-1}$.

al. (2003), we assume a stellar systemic velocity of $V_{\star, \text{LSR}} = 24.0 \text{ km s}^{-1}$, an outflow velocity of $V_{\text{out}} = 5.5 \text{ km s}^{-1}$, and a mass loss rate of $\dot{M} \sim 5.3 \times 10^{-7} M_{\odot} \text{ yr}^{-1}$ (scaled to our adopted distance). Using the *Hipparcos* proper motions from van Leeuwen (2007) of $12.63 \pm 1.74 \text{ mas yr}^{-1}$ in right ascension and $-9.71 \pm 1.67 \text{ mas yr}^{-1}$ in declination, we derive a peculiar space motion of $V_{\text{space}} = 26.3 \text{ km s}^{-1}$ along a $\text{PA} = 147^{\circ}6$ (Table 5).

R Peg was previously detected in H I by Gérard & Le Bertre (2006), who found evidence for a two-component line profile comprising a strong, narrow, roughly Gaussian component superposed on a broader pedestal. They found a velocity offset of $\sim 2 \text{ km s}^{-1}$ between the two components, with the two bracketing the systemic velocity of the star as determined from CO observations.

4.4.1. VLA Results for R Peg

H I channel maps surrounding the stellar systemic velocity of R Peg are presented in Figure 11. The morphology of the H I emission seen in these channel images is unlike any other star that has been imaged in H I to date. H I emission is clearly detected near the stellar position in several velocity channels bracketing V_{\star} . However, at $V_{\text{LSR}} = 25.1 \text{ km s}^{-1}$, the emission peak is offset by roughly an arcminute (one beam width) to the southeast of the stellar position. In the three velocity channels from 23.2 to 24.5 km s^{-1} , multiple emission peaks are present near the stellar position, but again the peak

emission in each channel is offset to the southwest of the star, with a relative dearth of emission at the stellar position itself. The morphology in these channels is somewhat reminiscent of a bipolar flow (but see below). This bifurcation is even more evident at $V_{\text{LSR}} = 22.5 \text{ km s}^{-1}$, but here the far reaches of the two lobes curve to form a horseshoe shape, with an extent of $> 15'$ (1.7 pc). This “horseshoe” is also delineated by multiple emission clumps at $V_{\text{LSR}} = 21.9 \text{ km s}^{-1}$. Finally, from $V_{\text{LSR}} = 20.0$ to 21.3 km s^{-1} , the emission clumps along the horseshoe decrease in number and peak column density while their projected distances from the star increase.

We present an H I total intensity map for R Peg in Figure 12. This map confirms that the peak H I column density toward R Peg does not coincide with the stellar position, but instead lies at a projected distance of $\sim 1'$ (0.1 pc) southeast of the star.

A global H I spectrum of R Peg is shown in Figure 13. There are hints of a slight asymmetry in the line profile, as well as a line peak that is broader and flatter than the other stars in the current sample. Nonetheless, a single Gaussian (dotted line on Figure 13) provides a reasonable fit to the data for the purpose of characterizing the global line parameters. Based on such a fit, we measure a peak H I flux density of $0.16 \pm 0.01 \text{ Jy}$, in excellent agreement with Gérard & Le Bertre (2006). We also find a FWHM line width of $4.35 \pm 0.39 \text{ km s}^{-1}$, centered at $V_{\text{LSR}} = 22.4 \pm 0.2 \text{ km s}^{-1}$. The H I line centroid is blueshifted by $\sim 1 \text{ km s}^{-1}$ relative to the stellar systemic velocity determined from CO observations. From our

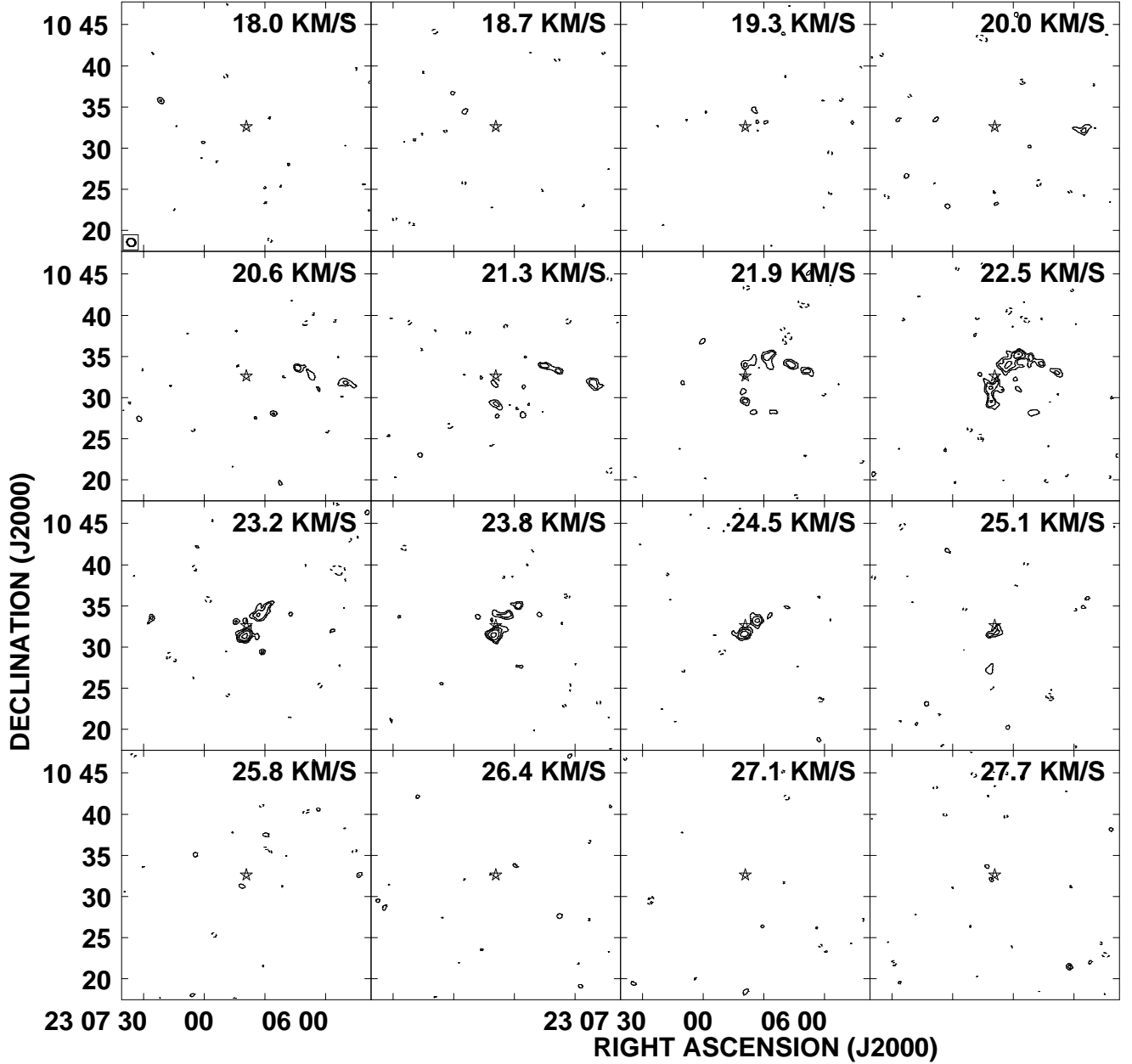


FIG. 11.— HI channel maps bracketing the systemic velocity of R Peg, derived from naturally weighted VLA data. The spatial resolution is $\sim 63'' \times 57''$. A star symbol indicates the stellar position. Contour levels are $(-4.2[\text{absent}], -3, 3, 4.2, 6, 8.4) \times 1.7 \text{ mJy beam}^{-1}$. The lowest contour is $\sim 3\sigma$. The field-of-view shown is comparable to the VLA primary beam.

Gaussian fit we also calculate an integrated HI flux density of $\int S_{\text{HI}} d\nu = 0.76 \pm 0.09 \text{ Jy km s}^{-1}$, translating to an HI mass of $M_{\text{HI}} \approx 0.029 M_{\odot}$. After scaling to account for our different adopted distances, the latter agrees closely with the value of $0.03 M_{\odot}$ previously reported by Gérard & Le Bertre (2006).

Gérard & Le Bertre (2006) also reported a second weaker, broader line component centered on the stellar systemic velocity and with a velocity extent comparable to that of the CO(2-1) line emission (FWHM $\sim 10 \text{ km s}^{-1}$). New NRT measurements (Gérard & Le Bertre, in prep.) reaffirm the presence of this broad component with a peak flux density of $0.006 \pm 0.003 \text{ Jy}$, too weak to have been detected in the current VLA data.

4.4.2. Discussion of R Peg Results

Above we noted the presence of an offset of $\sim 0.1 \text{ pc}$ to the southeast between the peak HI column density observed near R Peg and the stellar position. The direction of this offset is within $\sim 10^\circ$ of position angle of the space velocity vector that we have computed for the star ($\text{PA} \approx 148^\circ$; Table 5), suggesting that one possible explanation is that there is an accumulation of material in front of the star caused by the “snowplow effect” (Isaacman 1979). In this picture, the gas to the northwest of the star could comprise a trailing wake of material, ram pressure-stripped through the interaction between the CSE and the local ISM (see §4.2.2). Consistent with this hypothesis, over the velocity channels spanning

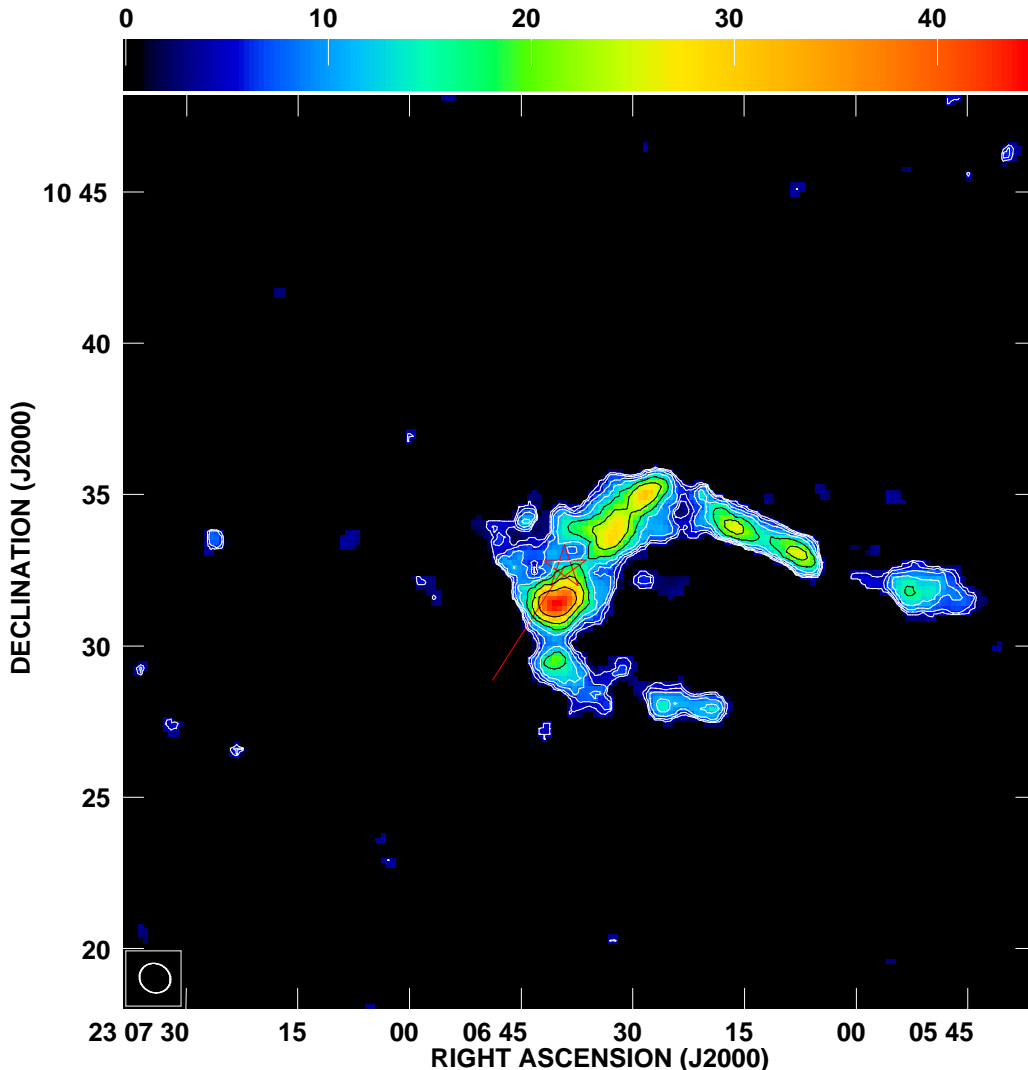


FIG. 12.— H I total intensity map of R Peg derived from naturally weighted data. A star symbol indicates the stellar position and the red line indicates the direction of space motion. The spatial resolution is $\sim 63'' \times 57''$. The map was constructed from emission spanning LSR velocities 20.0 to 25.1 km s^{-1} . Contour levels are (1,1.4,2,2.8,4,5.6,8) $\times 4 \text{ Jy beam}^{-1} \text{ m s}^{-1}$ and the intensity range is 0 to 43 $\text{Jy beam}^{-1} \text{ m s}^{-1}$. To minimize noise in the map, data at a given point were blanked if they did not exceed a 2σ threshold after smoothing by a factor of three spatially and spectrally.

25.1 km s^{-1} to 22.5 km s^{-1} , the emission in the putative wake shows a systematic increase in projected distance from R Peg with decreasing LSR velocity, as would be expected for debris that is being slowly decelerated by dynamical friction from the local ISM (see Matthews et al. 2008, 2011b; Raga & Cantó 2008). A related possibility is that the lobes of H I emission near the star are the remnants of a wake of debris shed during a previous cycle of mass-loss, and that the material has since drifted relative to the stellar position. This could also help to explain the small blueshift of the H I line centroid relative to the systemic velocity determined from molecular line observations visible in Figure 13. However, an ISM flow originating from a northerly direction would seem to be required to account for the direction of the offset between the star and the H I emission, as well as the curving sides of the horseshoe, which are oriented roughly perpendicular to the direction of the stellar space motion.

Despite the bifurcated appearance of the emission in several of the H I channel maps (Figure 11), we con-

sider the possibility that the H I surrounding R Peg results from some type of bipolar outflow to be unlikely. While bipolar flows are known in the case of a number of AGB stars, with the exception of the high-velocity flows ($\sim 100 \text{ km s}^{-1}$) arising from certain known or suspected binaries (Imai et al. 2002; Sahai et al. 2003), these outflows do not tend to be strongly collimated (e.g., Inomata et al. 2007; Libert et al. 2010; Castro-Carrizo et al. 2010). Further, in the case of R Peg, the two “lobes” would have to be oriented close to the plane of the sky to account for their similar radial velocities. Finally, the asymmetry of the velocity-integrated emission relative to the stellar position and the elongation of the emission parallel to the space motion vector (Figure 12) are both effects expected as a result of interaction between the ejecta of a moving star and the surrounding ISM.

4.5. *Y Canum Venaticorum* (*Y CVn*)

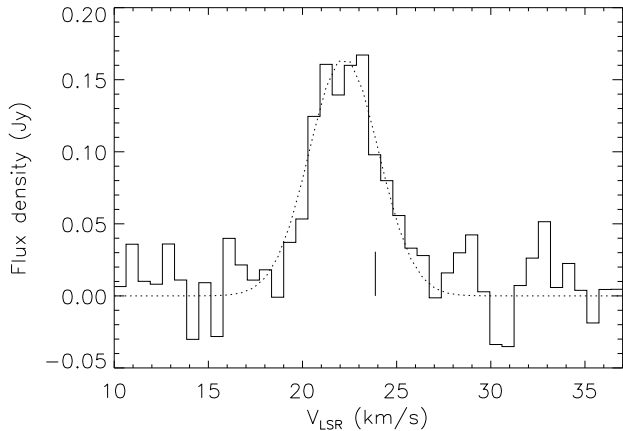


FIG. 13.— Spatially integrated HI spectrum of R Peg. The spectrum was derived from naturally weighted VLA data (after correction for primary beam attenuation) by integrating the emission in each velocity channel within a 15.5×8.3 aperture centered at $\alpha_{J2000} = 23^{\text{h}} 06^{\text{m}} 18.49^{\text{s}}$, $\delta_{J2000} = 10^{\circ} 31' 06.0''$. The dotted line shows a Gaussian fit to the line profile. The vertical bar indicates the stellar systemic velocity as determined from CO measurements.

Y Canum Venaticorum (Y CVn) is a rare example of a J-type carbon star. Its exact evolutionary stage is poorly known (e.g., Dominy 1984; Lambert et al. 1986; Lorenz-Martins 1996). The absence of technetium absorption (Little et al. 1987) and the lack of enhancement in *s*-process elements (Utsumi 1985) both suggest that the star has not yet undergone a thermal pulse. Some authors have even suggested that Y CVn is still on the red giant branch and that its carbon-rich composition may have resulted from a core He flash (Dominy 1984), although the high derived mass loss rate from the star appears to preclude this possibility and place the star on the AGB (e.g., Izumiura et al. 1996). The bolometric luminosity of Y CVn also places it on the AGB; Libert et al. (2007) derived a value of $9652L_{\odot}$ (scaled to our adopted distance; see below) using the bolometric correction of Le Bertre et al. (2001).

Y CVn belongs to the class of semi-regular variables, having a dominant pulsation period of ~ 160 days and secondary periods of 273 and 3000 days (Kiss et al. 1999). (Another star in our sample, the oxygen-rich Y UMa, is also a triply periodic semi-regular variable; see §4.3). Lambert et al. (1986) derived an effective temperature for Y CVn of ~ 2730 K.

From CO(3-2) observations, Knapp et al. (1998) derived a stellar systemic velocity for Y CVn of $V_{\star, \text{LSR}} = 21.1 \pm 0.9$ km s $^{-1}$, an outflow velocity for its wind of $V_{\text{out}} = 7.8 \pm 1.3$ km s $^{-1}$, and a mass loss rate $\dot{M} = 1.7 \times 10^{-7} M_{\odot} \text{ yr}^{-1}$ (scaled to our adopted distance). We note however that the observations of Jura et al. (1988) imply a large ^{13}C abundance in the star, thus the mass-loss rate derived from ^{12}CO lines may be underestimated by a factor of ~ 1.4 (see Libert et al. 2007).

The distance to Y CVn is uncertain, with values in the literature differing by more than ± 60 pc. Here we adopt a value of 272 pc based on the re-analysis of the *Hipparcos* parallax measurements by Knapp et al. (2003; 3.68 ± 0.83 mas). The proper motion is -1.40 ± 0.31 mas yr $^{-1}$ in right ascension and 13.24 ± 0.26 mas yr $^{-1}$ in decli-

nation (van Leeuwen 2007), which translates to a peculiar space velocity of $V_{\text{space}} = 31.0$ km s $^{-1}$ at PA = $36^{\circ} 8$.

Y CVn was previously detected in HI with the NRT by Le Bertre & Gérard (2004) and Libert et al. (2007) (see §4.5.2 for a discussion). Y CVn has also long been known to be surrounded by extended FIR emission (Young et al. 1993a; Izumiura et al. 1996; Geise 2011; Cox et al. 2012a). The *ISO* 90 μm data of Izumiura et al. show a central infrared source surrounded by a quasi-circular shell with an inner radius $r_{\text{in}} \sim 2.8$ and an outer radius $r_{\text{out}} \sim 5.1$. This shell is displaced slightly relative to the central infrared source. Izumiura et al. interpreted the properties of the FIR emission as indicating that Y CVn has undergone a decrease in mass loss rate of two orders of magnitude compared to the value at the time of the dust shell formation. However, Libert et al. proposed an alternative interpretation, namely that the shell is a several hundred thousand year-old structure formed by the slowing down of the stellar wind by the surrounding matter. This does not rule out that changes in the mass loss rate over time have occurred in Y CVn, but it removes the requirement of an abrupt drop in \dot{M} posterior to the formation of shell in order to explain the central hole seen in the FIR observations. As described below, our new data strengthen the interpretation put forth by Libert et al. and permit a more detailed comparison with the *ISO* FIR data.

4.5.1. VLA Results for Y CVn

HI channel maps for Y CVn derived from a tapered, naturally weighted version of our VLA data cube are presented in Figure 14. HI emission associated with the CSE of Y CVn is detected at LSR velocities ranging from 15.3 to 25.6 km s $^{-1}$. We show a tapered version of our data here despite their lower spatial resolution, as they better highlight the faint emission features present near the stellar position in the velocity channels from 15.3 to 17.9 km s $^{-1}$ and from 24.3 to 25.6 km s $^{-1}$. At the velocities closest to the stellar systemic velocity, the emission appears extended and clumpy and distributed over a shell-like structure, while a relative dearth of emission is notable directly toward the stellar position.

An HI total intensity map of Y CVn derived from naturally weighted data is presented in Figure 15. The stellar position is offset $\sim 45''$ to the northeast relative to the geometric center of the HI emission distribution. The HI nebula is roughly symmetric about the position angle of this offset ($\sim 42^{\circ}$), which corresponds to the direction of space motion of the star (Table 5). In contrast to the quasi-spherical appearance of the CSE in previous FIR images (Izumiura et al. 1996), the integrated HI distribution exhibits a more boxy shape, with the extent of the northeastern edge of the nebula being somewhat broader ($\sim 9'$) than the southwest side ($\sim 7'$). This boxiness is also visible in the *Spitzer* 70 μm image of Geise (2011).

The HI distribution of Y CVn is quite clumpy down to the resolution limit of our data, with two of the brightest clumps lying at the southern and western “corners” of the nebula. Several additional compact, quasi-spherical clumps of gas are also detected outside the main emission distribution and appear to be connected with the CSE by faint ($\sim 3\sigma$) tendrils of gas. The nature of these structures is unclear, but they appear to be circumstellar

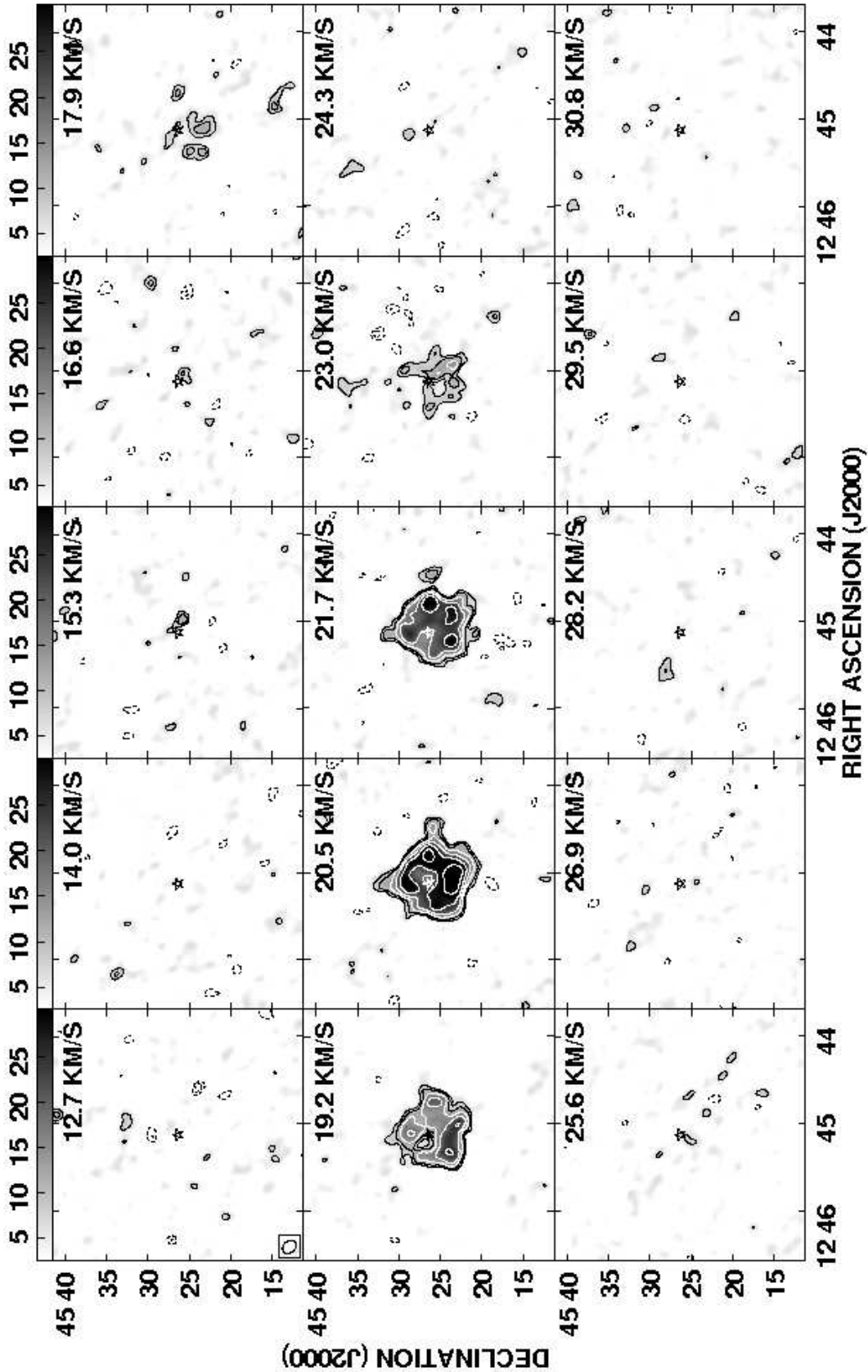


FIG. 14.— H I channel maps bracketing the LSR velocity of Y CVn, derived from tapered, naturally weighted VLA data. The velocities shown correspond to the values over which CO(3-2) emission was detected by Knapp et al. 1998. A star symbol indicates the stellar position. The spatial resolution is $\sim 107'' \times 83''$. Contour levels are $(-3.5, -2.5, 2.5, 3.5, 5, 7.1, 10.0, 14.1) \times 2.6 \text{ mJy beam}^{-1}$. The lowest contour is $\sim 2.5\sigma$. The greyscale intensity levels are 2.7 to $30.0 \text{ mJy beam}^{-1}$.

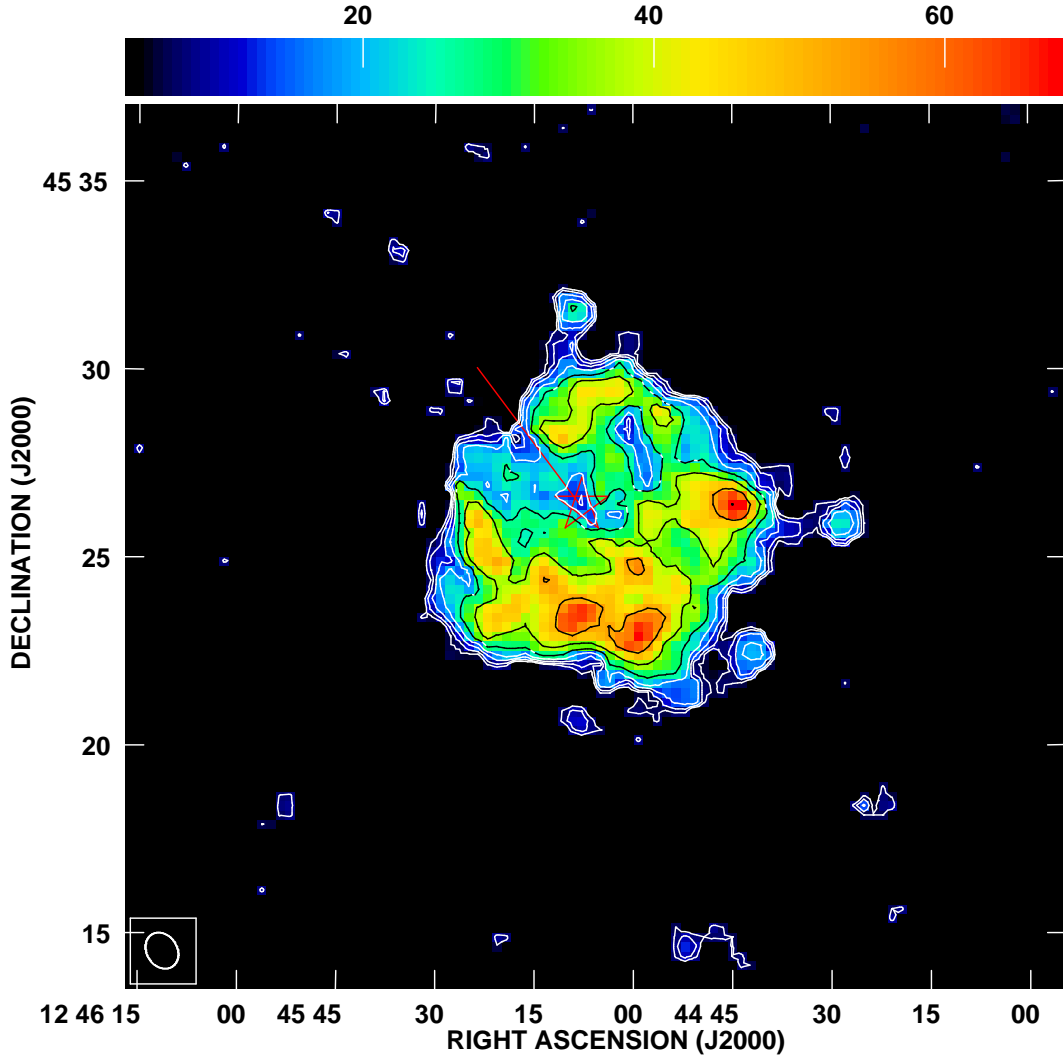


FIG. 15.— HI total intensity map of Y CVn derived from naturally weighted VLA data. The spatial resolution is $\sim 61'' \times 49''$. The map was constructed from emission spanning LSR velocities 17.8 to 23.0 km s^{-1} . Contour levels are $(0.5, 0.7, 1, 1.4, 2, 2.8, 4, 5.6, 8) \times 13 \text{ Jy beam}^{-1} \text{ m s}^{-1}$. To minimize noise in the map, data at a given point were blanked if they did not exceed a 2σ threshold after spatially smoothing the data by a factor of three. Intensity levels are 4 to 68 Jy m s^{-1} . A star symbol indicates the stellar position, and the red line indicates the direction of space motion.

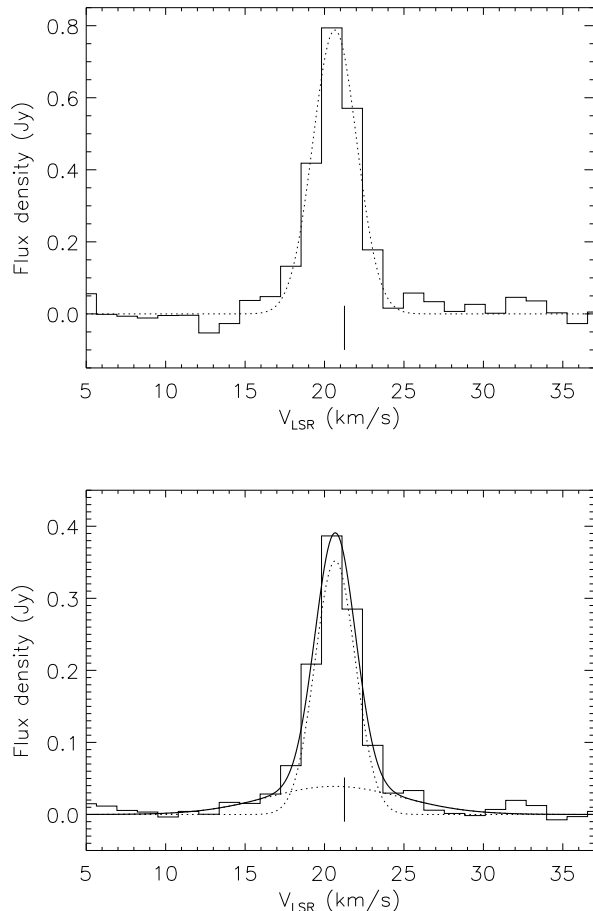


FIG. 16.— Spatially integrated HI spectra of Y CVn, derived from naturally weighted VLA data (after correction for primary beam attenuation). *Upper panel:* Spectrum obtained by integrating the emission in each velocity channel within a $12'0 \times 12'2$ aperture centered at $\alpha_{J2000} = 12^{\text{h}} 45^{\text{m}} 01.2^{\text{s}}$, $\delta_{J2000} = 45^{\circ} 25' 39.9''$. The dotted line shows a Gaussian fit to the spectrum and the vertical bar indicates the stellar systemic velocity as determined from CO observations. *Lower panel:* Spectrum integrated within a circular aperture of radius $2'8$ centered on the star. The dotted lines show a two-component Gaussian fit and the thick solid line shows their sum (see text for details).

in nature.

The depression in the total HI column density toward the stellar position seen in the individual HI channel maps is also apparent in the HI total intensity map. In addition, the HI total intensity map reveals a “notch” extending from the star to the northeastern edge of the nebula along $\text{PA} \approx 42^{\circ}$ where relatively little HI emission is detected. The nature of this feature is discussed further below.

The spatially integrated HI spectrum of Y CVn (Figure 16) displays a narrow, roughly Gaussian shape, similar to what we observe for V1942 Sgr (§4.6.2). Based on a single Gaussian fit (dotted line on Figure 16) we measure a peak flux density of 0.79 ± 0.02 Jy and a FWHM linewidth of 3.2 ± 0.1 km s $^{-1}$ centered at an LSR velocity of 20.65 ± 0.05 km s $^{-1}$. From this fit we derive an integrated HI flux density of $\int S_{\text{HI}} d\nu = 2.68 \pm 0.11$ Jy km s $^{-1}$, translating to an HI mass $M_{\text{HI}} \approx 0.047 M_{\odot}$.

The HI mass and global line width that we derive from

the VLA data are in excellent agreement with those derived previously from NRT observations by Le Bertre & Gérard (2004), although our integrated HI line flux is $\sim 25\%$ smaller than reported by Libert et al. (2007). Further comparisons with prior NRT results are described below.

4.5.2. Discussion of Y CVn Results

Above we drew attention to the presence of a “notch” (depression in the HI column density) in the shell of Y CVn, lying ahead of the star and running parallel to its direction of space motion. A similar feature was also seen in the CSE of Y UMa (§4.3.2). In both cases, a corresponding depression is also present in the FIR light (Figure 10 and Figure 17, discussed below). The origin of these notches is unclear, but one possibility is that they are linked to instabilities along the leading edge of the CSE. For example, in the hydrodynamic simulations of mass-losing stars moving through the ISM performed by Wareing et al. (2007a, b) and Villaver et al. (2012), instabilities may develop under certain conditions that lead to a bending of the leading edge of the CSE (bow shock) back toward the star. Unfortunately, none of the currently published simulations are closely matched to the current age, mass-loss parameters, and space motion parameters of Y CVn and Y UMa.

Another interesting phenomenon seen in the HI images of Y CVn is the presence of multiple compact knots of emission lying just exterior to the CSE at several locations along both its leading and trailing edges. These knots are detected at high significance and appear to be linked to the Y CVn shell by tendrils of gas, suggesting that they are quite likely to be circumstellar in nature. One possibility is that these knots may arise from thermal instabilities (e.g., Zucker & Soker 1993) along the interface between the Y CVn shell and the surrounding ISM.

In Figure 17 we present HI contours derived from the robust +1 version of our VLA data overlaid on the *ISO* $90\mu\text{m}$ data from Izumiura et al. (1996). We downloaded the archival data for Y CVn as described in §4.3.2. The original *ISO* image has a pixel size of $15''0$ but was re-binned to $10''$ pixels for display purposes.

The shape and extent of the HI and FIR emitting shells are quite similar along the northwest and southwest edges. However, along the southeast portion of the CSE, the HI contours extend outside the FIR emission detected by *ISO*. At the same time, an absence of HI emission is apparent along the northeast (leading) side of the FIR-emitting shell. The gas along this edge may have been ionized by shocks owing to the interaction with the ISM. However, there is no obvious enhancement in FIR surface brightness or change in morphology along the leading edge of the shell that would indicate the presence of a strong bow shock capable of ionizing hydrogen. Similarly, no clear evidence of a FIR bow shock is seen in the more recent, higher resolution observations from *Herschel* (Cox et al. 2012a). We have also examined archival *Galaxy Evolution Explorer* (*GALEX*) images of the region around the star to search for FUV emission from a possible bow shock as has been detected in the case of at least three evolved stars (Martin et al. 2007; Sahai & Chronopoulos 2010; Le Bertre et al. 2012), but no extended FUV emission is visible.

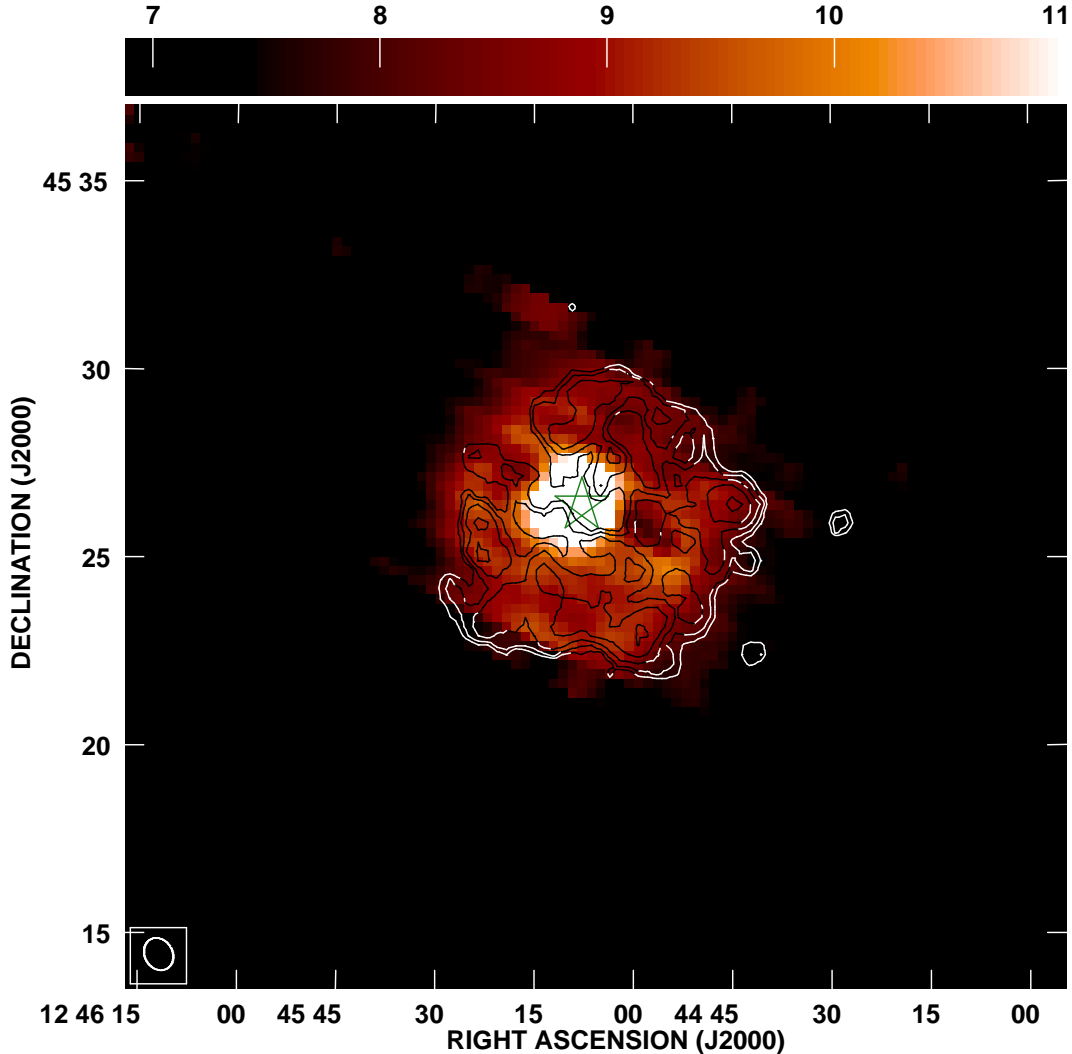


FIG. 17.— HI total intensity contours of Y CVn derived from VLA data with robust +1 weighting, overlaid on an *ISO* 90 μ m image of the star from Izumiura et al. 1996. The HI data have a resolution of $\sim 54'' \times 44''$. The contour levels are (1,1.4,2,2.8,4,5.6,8) $\times 13$ Jy beam $^{-1}$ m s $^{-1}$. The *ISO* image has brightness units of MJy sr $^{-1}$.

Izumiura et al. (1996) noted that the western part of the FIR shell of Y CVn has a slightly lower surface brightness in both 90 μ m and 160 μ m images compared with the eastern side. Similarly, we find that the HI emission is slightly enhanced on the eastern side of the shell compared with the western side (cf. Figures 15 & 17). After applying a multiplicative correction of 1.4 to account for the mass of helium, the mass we derive for the circumstellar shell of Y CVn ($\approx 0.066 M_{\odot}$) is consistent with the value derived previously from FIR observations ($M_{\text{shell}} \approx 0.047$ to $0.16 M_{\odot}$, scaled to our adopted distance; Izumiura et al. 1996). Since the latter determination depends on the adopted dust-to-gas ratio, implicit to this agreement is that the dust-to-gas ratio of the shell is typical of other carbon-rich stars ($\sim 4.5 \times 10^{-3}$; Jura 1986). It also assumes that the gas in the shell is predominantly atomic, although as noted by Libert et al. (2007), the temperature and density conditions within Y CVn's shell may be conducive to molecule formation through a non-equilibrium chemistry.

Our VLA imaging confirms that the narrow HI line component detected by Le Bertre & Gérard (2004) and

Libert et al. (2007) is closely linked with material distributed within the extended FIR-emitting shell surrounding Y CVn. However, both of these studies also reported a second broad (FWHM ~ 16 km s $^{-1}$) line component that they attributed to a counterpart to the freely expanding wind traced by molecular lines at small radii. This broad component is not evident in the global HI profile presented in Figure 16. However, we tentatively identify a counterpart to this component in Figure 16 (lower panel), where we plot a spectrum derived from only the emission confined within a radius of 2'.8. (This radius was adopted based on a model of the shell presented in Appendix A; see also below). We find that a single Gaussian fit to the spectrum in the lower panel of Figure 16 leaves statistically significant residuals in the line wings. Adopting instead a two-Gaussian fit, we find a narrow component with $F_{\text{peak}} = 0.35 \pm 0.02$ Jy and a FWHM line width of 3.0 ± 0.1 km s $^{-1}$, centered at $V_{\text{LSR}} = 20.68 \pm 0.04$ km s $^{-1}$ (i.e., consistent in position and width with the fit to the global spectrum in the upper panel of Figure 16) and a broad component centered

at $20.6 \pm 0.5 \text{ km s}^{-1}$ with $F_{\text{peak}} = 0.04 \pm 0.02 \text{ Jy}$ and a FWHM line width of $10.0 \pm 1.8 \text{ km s}^{-1}$. The line width we derive for the broader component is smaller than the values reported by Le Bertre & Gérard (14.3 km s^{-1}) and by Libert et al. ($\sim 16 \text{ km s}^{-1}$). However, Libert et al. fitted a rectangular rather than a Gaussian line profile, and moreover, the single-dish determinations are sensitive to uncertainties in baseline fitting. Thus accounting for systematic uncertainties, it appears that all three measurements of the broad H I component are roughly consistent with the CO(3-2) line, for which Knapp et al. 1998 measured a FWHM $\sim 12 \text{ km s}^{-1}$ and derived $V_{\text{out}} = 7.8 \pm 1.3 \text{ km s}^{-1}$. This supports the suggestion that this material is linked with Y CVn's freely expanding wind. Corroborating evidence is also seen in our H I channel maps (Figure 14), where weak emission ($\geq 2.5\sigma$) is detected near the stellar position at velocities offset by $\sim \pm 4$ to 6 km s^{-1} from the stellar systemic velocity. However, we note that there is evidence that the H I emission at these velocity extremes is spatially extended on scales $> 1'$ and thus must be extended well beyond the outer boundary of the detected CO(1-0) emission ($r \sim 6''.5$) and the molecular dissociation radius ($r \sim 20''$; Neri et al. 1998). Additionally, the peaks of this emission near the velocity extrema in some channels appear offset from the stellar position by $\sim 1'$.

Our new VLA measurements allow us to provide improved constraints on the numerical model of the H I shell of Y CVn presented by Libert et al. (2007) (see Appendix A for details). In Figure 28c we show our model spectrum overplotted on the global VLA H I spectrum of Y CVn. Based on this model, we estimate an age for the H I shell of $\sim 4.5 \times 10^5 \text{ yr}$. This value is consistent with the previous determination of Libert et al., but we note that we have adopted a larger distance to the star than those authors as well as slightly different model parameters. Our value is more than 6 times larger than the age for the circumstellar shell previously derived by Young et al. (1993b) based on FIR data.

4.6. V1942 Sagittarii (V1942 Sgr)

V1942 Sagittarii (V1942 Sgr) has been previously classified an N-type carbon star and a long period irregular (Lb) variable. However, Miller et al. (2012) recently reported evidence that V1942 Sgr belongs to the class of DY Persei-type stars. DY Persei stars, only a handful of which have been identified to date, are thought to be either a cooler subclass of R Coronae Borealis stars (see Clayton 2012) or normal carbon stars that have experienced ejection events (Tisserand et al. 2009). DY Persei-type stars generally exhibit C-rich spectra similar to N-type carbon stars and show detectable ^{13}C . They are also characterized by large-amplitude, irregular variations in brightness (> 1.5 magnitudes). In the case of V1942 Sgr, Miller et al. reported evidence for multiple periodicities in the light curve variations (120, 175, and 221 days) that appear to change on time scales of 1-2 years. However, Soszyński et al. (2009) found no evidence for a marked discontinuity between the variations observed among DY Persei stars and other carbon-rich long-period variables.

V1942 Sgr has an effective temperature $T_{\text{eff}} \approx 2960 \text{ K}$ (Bergeat et al. 2001) and a bolometric luminosity of

$5200 L_{\odot}$ (Libert et al. 2010a). Its properties are believed to place V1942 Sgr on the TP-AGB (e.g., Bergeat et al. 2002), although its new classification as a DY Persei-type star suggests that its evolutionary status and/or history could be somewhat different from the other carbon stars previously studied in H I. We adopt a distance to V1942 Sgr of 535 pc based on the *Hipparcos* parallax of $1.87 \pm 0.51 \text{ mas}$ (van Leeuwen 2007).

IRAS $60\mu\text{m}$ data show V1942 Sgr to be surrounded by an extended infrared shell of radius $3'.2$ ($\sim 0.5 \text{ pc}$; Young et al. 1993a). V1942 Sgr exhibits a featureless mid-infrared ($8\text{-}22\mu\text{m}$) spectrum, consistent with the absence of current mass loss (Olson & Raimond 1986). However, the changes in its variability and its DY Persei classification suggest that regular ejection events may be taking place (Miller et al. 2012). Furthermore, Libert et al. (2010a) found evidence of ongoing mass loss from CO observations.

The CO(1-0) and CO(2-1) profiles of V1942 Sgr obtained by Libert et al. (2010a) exhibit a two-component structure comprising broad and narrow components. In several cases, such line profiles have been found to be the hallmark of bipolar outflows in AGB stars (e.g., Kahane & Jura 1996; Bergman et al. 2000; Josselin et al. 2000; Libert et al. 2010b; Castro-Carrizo et al. 2010), although CO imaging observations are needed to confirm this interpretation for the case of V1942 Sgr. Based on the CO(1-0) line, Libert et al. (2010a) derive a stellar systemic velocity $V_{\star, \text{LSR}} = -33.75 \pm 0.25 \text{ km s}^{-1}$, outflow velocities for the broad (narrow) line components of $V_{\text{out}} = 17.5 \pm 0.5 \text{ km s}^{-1}$ ($5.0 \pm 0.5 \text{ km s}^{-1}$), and mass loss rates for the broad (narrow) components of $\dot{M} = 6.1 \times 10^{-7} M_{\odot} \text{ yr}^{-1}$ ($1.0 \times 10^{-7} M_{\odot} \text{ yr}^{-1}$). Results from the CO(2-1) line were comparable to within uncertainties. We note that the outflow velocity of V1942 Sgr is unusually large for an Lb variable (e.g., Olofsson et al. 2002), a fact that may be linked with its DY Persei status.

The proper motions derived from *Hipparcos* measurements of V1942 Sgr are $10.98 \pm 0.59 \text{ mas yr}^{-1}$ in right ascension and $-5.10 \pm 0.43 \text{ mas yr}^{-1}$ in declination. From these values we derive a Galactic peculiar space velocity $V_{\text{space}} = 40.2 \text{ km s}^{-1}$ at a position angle of $95^\circ 1'$ (Table 5).

4.6.1. VLA Results for V1942 Sgr

H I channel maps for V1942 Sgr derived from our naturally weighted VLA data are presented in Figure 18. An H I total intensity map derived from the same data is shown in Figure 19. As seen in Figure 18 (and in Figure 20, discussed below), V1942 Sgr lies at a velocity that suffers very low contamination from H I emission along the line-of-sight (see also Libert et al. 2010a). We are able to trace circumstellar H I emission at or near the stellar position at $\geq 3\sigma$ significance across five contiguous spectral channels ($V_{\text{LSR}} = -35.2$ to -30.1 km s^{-1}). The emission distribution at each of these velocities appears somewhat amorphous, but with a sharp drop-off in H I surface density at its boundaries. Versions of our H I data cube made using u - v tapering (not shown) do not reveal any emission extended beyond what is seen in Figure 18.

To first order, the velocity-integrated H I emission distribution of V1942 Sgr (Figure 19) has a shell-like mor-

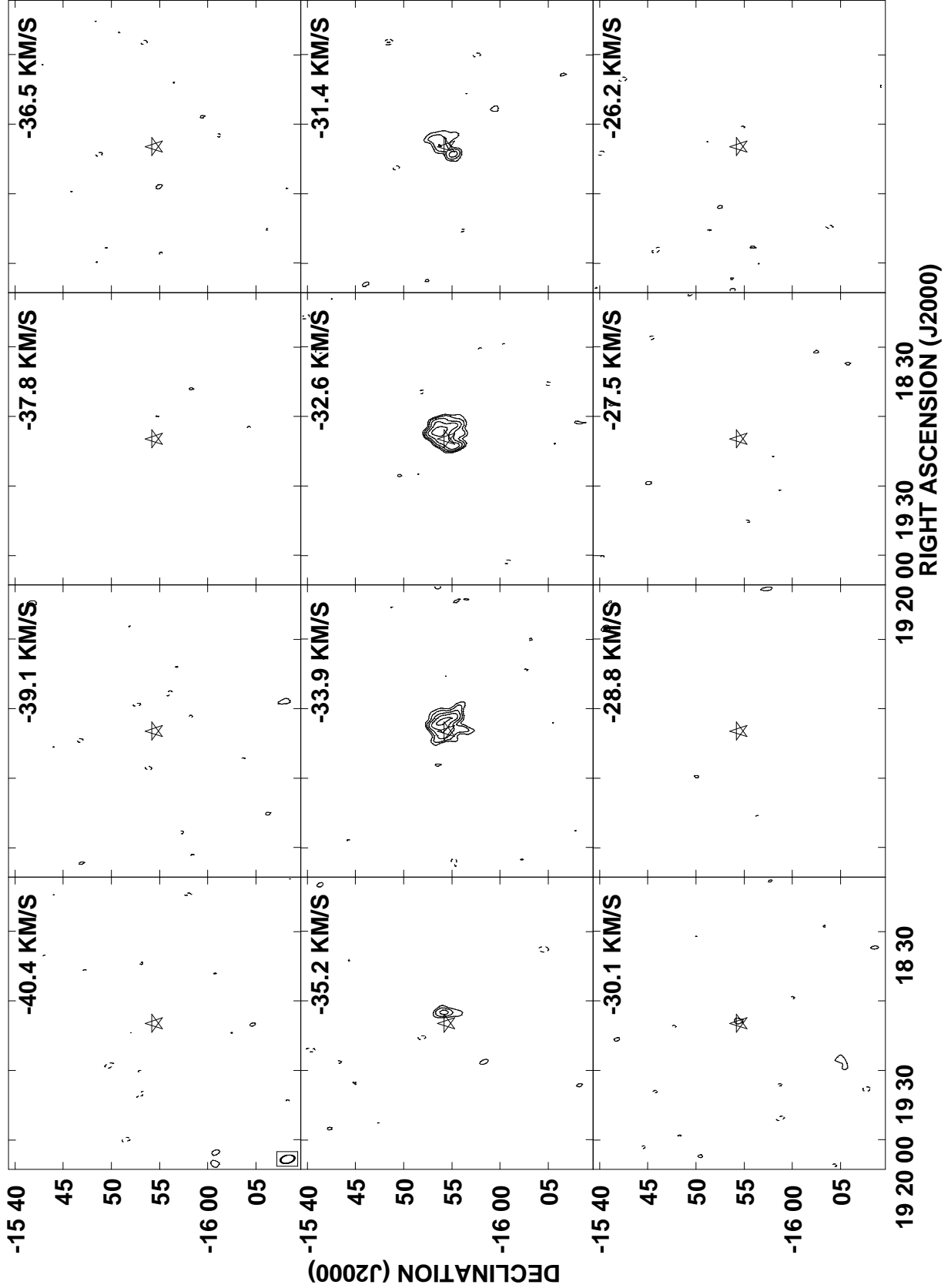


FIG. 18.— HI channel maps bracketing the LSR velocity of V1942 Sgr, derived from naturally weighted VLA data. The spatial resolution is $\sim 89'' \times 49''$. A star symbol indicates the stellar position. Contour levels are $(-4.2[\text{absent}], -3, 3, 4.2, 6, 8.4) \times 2.7 \text{ mJy beam}^{-1}$. The lowest contour is $\sim 3\sigma$. The field-of-view shown is comparable to the VLA primary beam.

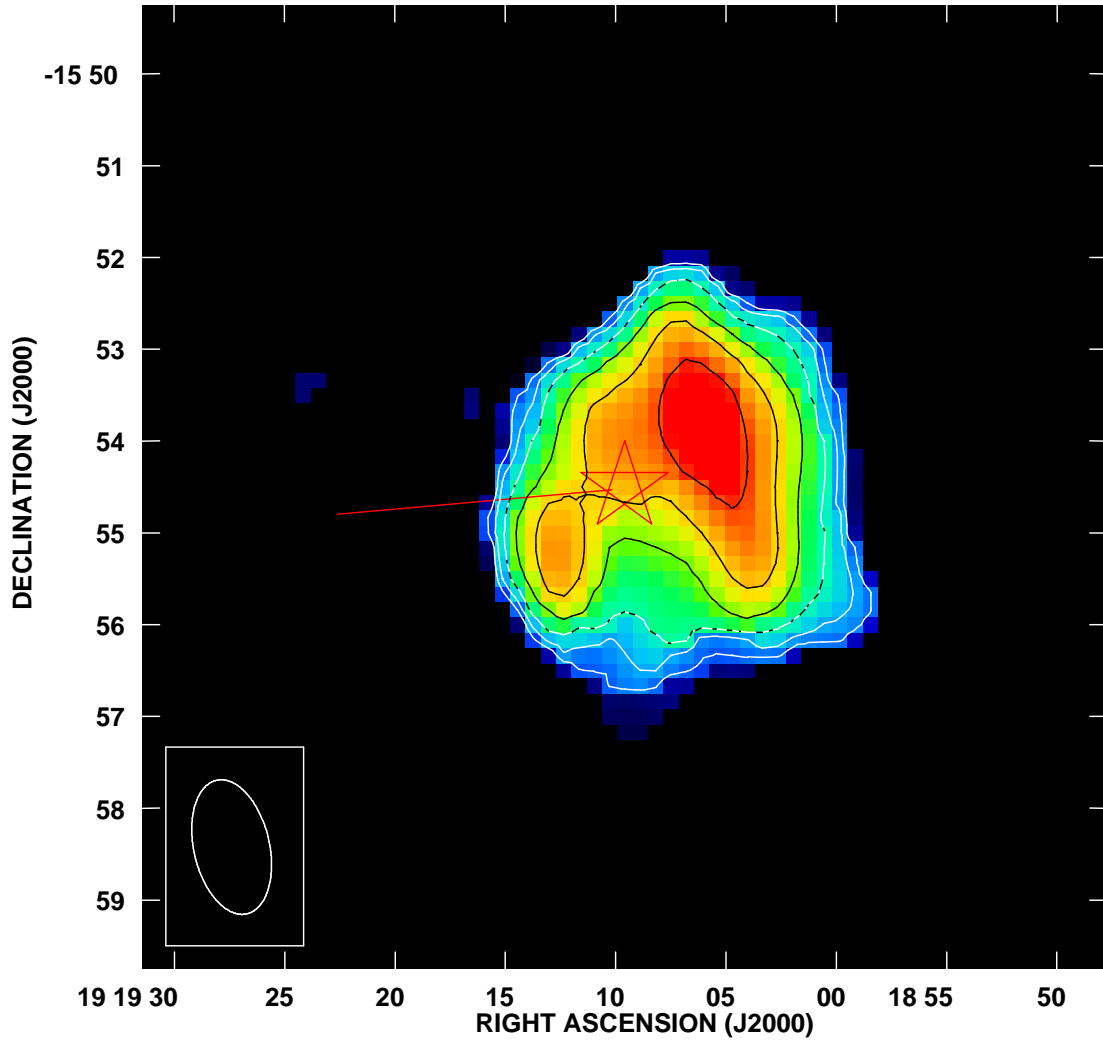


FIG. 19.— HI total intensity map of V1942 Sgr derived from naturally weighted VLA data. The spatial resolution is $\sim 89'' \times 49''$. A star symbol indicates the stellar position and the red line indicates the direction of space motion. The map was constructed from emission spanning LSR velocities -35.2 to -30.1 km s^{-1} . Intensity levels are 0 to $120 \text{ Jy beam}^{-1} \text{ m s}^{-1}$ and contour levels are $(1.4, 2, 2.8, 4, 5.6, 8) \times 14.1 \text{ Jy beam}^{-1} \text{ m s}^{-1}$. To minimize noise in the map, data at a given point were blanked if they did not exceed a 2σ threshold after smoothing by a factor of three spatially and spectrally.

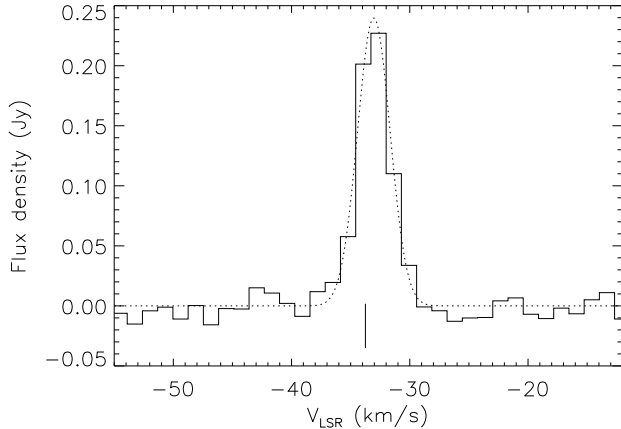


FIG. 20.— Spatially integrated HI spectrum of V1942 Sgr. The spectrum was derived from naturally weighted VLA data (after correction for primary beam attenuation) by integrating the emission in each velocity channel within a $4'7 \times 5'5$ aperture centered at $\alpha_{J2000}=19^{\text{h}} 19^{\text{m}} 06.5^{\text{s}}$, $\delta_{J2000} = -15^{\circ}54' 45''$. The vertical line indicates the stellar systemic velocity derived from CO observations. The dotted line shows a Gaussian fit.

phology, reminiscent of Y UMa (§4.3) and Y CVn (§4.5). Similar to those other two stars, the outer boundaries of the shell are irregular. The total extent of the HI emission of V1942 Sgr is roughly $4'0$ (~ 0.6 pc) east-west and $4'6$ (~ 0.7 pc) north-south, as measured through the position of the star. The stellar position is offset $\sim 30''$ to the east of the geometric center of the HI nebula. Other noteworthy features are the two enhancements in HI surface brightness that are observed southeast and northwest of the star, respectively (see also Figure 18). The northwestern feature is the brighter of the two and lies atop a spatially extended ridge of enhanced surface brightness. Both of the HI enhancements lie along a line that bisects the stellar position at $\text{PA} \approx 126^{\circ}$, although the significance of this is unclear, and the two surface brightness enhancements do not show any obvious relationship to the position angle of the peculiar space motion of the star ($\text{PA} \approx 95^{\circ}$).

A Gaussian fit to the integrated HI spectrum in Figure 20 yields a peak flux density of 0.240 ± 0.009 Jy, a FWHM line width of 3.23 ± 0.13 km s $^{-1}$, and a line centroid of $V_{\text{LSR}} = -33.04 \pm 0.06$ km s $^{-1}$. From these fit parameters, we derive an integrated HI flux density $\int S_{\text{HI}} d\nu = 0.82 \pm 0.04$ Jy km s $^{-1}$, translating to a total HI mass $M_{\text{HI}} \approx 0.055 M_{\odot}$. Our measurements are in good agreement with the HI line parameters reported by Libert et al. (2010a).

4.6.2. Discussion of V1942 Sgr Results

The maximum angular extent of the HI-emitting shell that we observe surrounding V1942 Sgr ($\sim 4'6$ across) is markedly smaller than the FIR diameter derived by Young et al. (1993a) from *IRAS* data ($\sim 6'4$). Furthermore, the good agreement between the HI size and HI line parameters that we derive in the present study compared with those derived from the NRT by Libert et al. (2010a) also suggests that V1942 Sgr has little or no circumstellar HI emission extended beyond what is detected in our VLA images. Thus in contrast to the carbon star Y CVn (§ 4.5), our findings suggest that the HI shell

of V1942 Sgr may be significantly more compact than the FIR-emitting shell. Simulations by van Marle et al. (2011) have shown that this type of segregation can occur preferentially for large dust grains (radius $\lesssim 0.105 \mu\text{m}$). Higher resolution observations would be of considerable interest for confirming the FIR extent of V1942 Sgr and for examining in detail the relationship between the FIR and HI emission.

Libert et al. (2010a) found evidence in their integrated HI line profile of V1942 Sgr for a weak ($\sim 6 \pm 2$ mJy) pedestal of emission extending from -39 to -27 km s $^{-1}$. Based on the results of numerical modeling, they attribute this weaker, broader line component to a counterpart to the freely expanding wind at small radii (as traced by the narrower of the two CO line components detected by these authors). They interpret the dominant narrow HI line component as arising from a detached shell that has been decelerated as a result of its interaction with the ISM. Thus the interpretation of the line profile is analogous to the cases of RX Lep, Y UMa, and Y CVn (see Appendix A).

We do not find any evidence for a counterpart to the broad HI emission component in our integrated VLA line profile (Figure 20) or in our HI channel maps (Figure 18). In the channel maps, we would expect the broad component to give rise to emission at or near the stellar position at velocities of roughly $V_{\star} \pm 5$ km s $^{-1}$. However, the absence of this component in our data is not surprising. Since its expected peak line strength of only $\sim 6 \pm 2$ mJy, it is near the limits of detectability in our present data (where RMS noise per channel is ~ 2.7 mJy beam $^{-1}$; Table 4).

We have also searched our HI data cube for a counterpart to the broad CO line component detected by Libert et al. (2010a). Consistent with Libert et al., we find no evidence of HI emission at velocities near $V_{\star} \pm 17.5$ km s $^{-1}$. Libert et al. suggested that this high-velocity outflow is likely to result from very recent mass-loss ($\lesssim 10^4$ years) and that it may be a signpost of the star being close to the end of its life on the AGB. This possibility is interesting in light of the newly established DY Persei classification of V1942 Sgr, since some workers have suggested that these may be highly evolved stars nearing the planetary nebula stage (see Miller et al. 2012 for discussion). HI and CO observations of additional DY Persei stars would be valuable for establishing whether the CSE properties of V1942 Sgr are typical of its class.

We have estimated an age for the HI shell surrounding V1942 Sgr using a simple numerical model (see Appendix A and Table A1 for details). The resulting fit to the global HI spectrum is presented in Figure 28d. We estimate that a duration of $\sim 7.2 \times 10^5$ yr was required to form the observed shell. This is $\sim 20\%$ higher than the previous estimate from Libert et al. (2010a) based on constraints from single dish data and more than 6 times larger than the CSE age derived by Young et al. (1993b) based on FIR data.

4.7. AFGL 3099

AFGL 3099 (=CRL 3099=IZ Peg) is a carbon star and Mira-type variable with a period of 484 days (Le Bertre 1992). This star has a very low effective temperature

(1800-2000 K; Gérard & Le Bertre 2006) and is the coolest AGB star observed in H I with the VLA to date. We adopt a distance to the star of 1500 pc based on the period-luminosity relation of Groenewegen & Whitelock (1996).

AFGL 3099 is thought to be in a highly evolved evolutionary state (Gehrz et al. 1978). It is similar to the prototypical carbon star IRC+10216 in that one of the few known examples of Galactic carbon stars to show regular, large-amplitude variability and exhibit a pulsation period longer than normal (optically selected) carbon Miras (Feast et al. 1985).

Knapp & Morris (1985) detected CO(1-0) emission from AFGL 3099 from which they derived a rather high mass-loss rate of $1.3 \times 10^{-5} M_{\odot} \text{ yr}^{-1}$ (after scaling to our adopted distance). They also found a stellar systemic velocity of $V_{*,\text{LSR}} = 46.6 \pm 0.4 \text{ km s}^{-1}$ and a wind outflow speed of $V_{\text{out}} = 10.1 \pm 0.5 \text{ km s}^{-1}$. The extremely red color of AFGL 3099 implies it is surrounded by a dense circumstellar dust shell (Gehrz et al. 1978). AFGL 3099 was not found to be an extended FIR source based on *IRAS* observations (Young et al. 1993a), although this may have been a consequence of the relatively large stellar distance.

4.7.1. VLA Results for AFGL 3099

H I channel maps of the AFGL 3099 field are presented in Figure 21 and a global H I spectrum coincident with the stellar position is presented in Figure 22. We find no evidence for H I emission associated with the CSE of AFGL 3099 despite the presence of negligible interstellar contamination. No emission is seen coincident with the stellar position at $\geq 2.5\sigma$ in any spectral channel within the band. Assuming a Gaussian line profile with FWHM equal to twice the outflow velocity measured in CO, we derive a 3σ upper limit for the H I mass of AFGL 3099 within a single synthesized beam centered on the star of $M_{\text{HI}} < 0.058 M_{\odot}$. This is consistent with the 1σ limit previously reported by Gérard & Le Bertre (2006).

4.7.2. Discussion of AFGL 3099 Results

The absence of detectable H I emission directly toward the position of AFGL 3099 despite its high mass loss rate is not entirely surprising. AFGL 3099 is significantly more distant than other stars in our sample (Table 1), and the extremely low effective temperature of the star suggests that the bulk of its wind may be molecular (Glassgold & Huggins 1983) or simply too cold to emit efficiently in the 21-cm line. However, another similarly cool and distant carbon Mira, AFGL 3068, was detected in H I by Gérard & Le Bertre (2006). Based on the data of Knapp & Morris (1985), AFGL 3099 has a ~ 3 times weaker integrated CO line intensity compared with AFGL 3068, but its peak H I intensity is more than 8 times weaker.

In the case of the cool and highly evolved carbon Mira IRC+10216 ($T_{\text{eff}} \sim 2200 \text{ K}$), Matthews & Reid (2007) found no H I emission coincident with the position of the star (see also Le Bertre & Gérard 2001), but detected arcs of H I emission displaced from the central position. These arcs were later found to be associated with the interface between the CSE and the ISM and to lie along an astrosheath and vortical tail visible in the FUV (Matthews

et al. 2011a). We do not find any sign of analogous features in the AFGL 3099 field, although the large distance of this star from the Galactic plane suggests that the local ISM density is likely to be significantly lower than in the case of IRC+10216.

Another possible explanation for the absence of extended H I emission around AFGL 3099 is that the star has only recently begun undergoing mass loss at a high rate (cf. Libert et al. 2010a). We further note that the outflow velocity for AFGL 3099 is surprisingly low for a star this red (e.g., Loup et al. 1993, their Figure 8), suggesting that its mass-loss properties may be atypical.

4.8. TX Piscium (TX Psc)

The N-type carbon star TX Piscium (TX Psc) is frequently classified as an irregular (Lb) variable, although evidence for a period of ~ 220 days has been reported by Wasatonic (1995, 1997). TX Psc was among the first evolved stars in which technetium was detected (Merrill 1956) and it is thought to be in a post-Mira evolutionary phase (Judge & Stencel 1991). TX Psc is the warmest carbon star that has been imaged in H I to date, with $T_{\text{eff}} = 3115 \pm 130 \text{ K}$ (Bergeat et al. 2001). Based on the *Hipparcos* parallax of $3.63 \pm 0.39 \text{ mas}$ (van Leeuwen 2007) we adopt a distance to TX Psc of 275 pc. A recent analysis by Klotz et al. (2013) suggests that the initial mass of TX Psc was in the range 1-3 M_{\odot} .

Using the CO(1-0) data of Eriksson et al. (1986), Loup et al. (1993) derived an outflow velocity for TX Psc's wind of $V_{\text{out}} = 10.7 \pm 1.9 \text{ km s}^{-1}$ and a mass loss rate $\dot{M} = (3.1 \pm 1.6) \times 10^{-7} M_{\odot} \text{ yr}^{-1}$ (scaled to our adopted distance). The stellar systemic velocity as derived from CO observations varies among different authors depending on the telescope and the transition used; here we adopt the mean of the values quoted by Olofsson et al. (1993): $V_{*,\text{LSR}} = 12.2 \pm 1.1 \text{ km s}^{-1}$, where the quoted uncertainty is based on the dispersion in the measurements. The *Hipparcos* proper motions of $-33.68 \pm 0.40 \text{ mas yr}^{-1}$ in right ascension and $-24.49 \pm 0.32 \text{ mas yr}^{-1}$ in declination imply a peculiar space velocity of $V_{\text{space}} = 66.4 \text{ km s}^{-1}$ along a position angle of 248° (Table 5).

4.8.1. VLA Results for TX Psc

We present H I channel maps for TX Psc in Figure 23. In the spectral channel centered at $V_{\text{LSR}} = 12.4 \text{ km s}^{-1}$ (which is the nearest to the systemic velocity of the star), H I emission is detected at the position of TX Psc and is seen extending several arcminutes to the northeast. Spatially resolved emission is also clearly detected toward the stellar position at $V_{\text{LSR}} = 13.6 \text{ km s}^{-1}$. The spectral channels with $V_{\text{LSR}} \geq 12.4 \text{ km s}^{-1}$ appear to suffer only minimally from line-of-sight confusion, implying that the detected emission almost certainly arises from the CSE of TX Psc. The distribution of this material is consistent with a gaseous wake trailing the star. The H I emission structure in these velocity channels also resembles the morphology and orientation of the faint FIR-emitting wake seen in the *Herschel* images of Jorissen et al. (2011) and the *Spitzer* $70\mu\text{m}$ image of Geise (2011).

Looking toward more blueshifted velocities ($V_{\text{LSR}} = 7.2$ to 11.1 km s^{-1}), we see evidence of an increasingly extended trail of emission stretching behind TX Psc. This emission appears well-collimated out to roughly $8'$ from

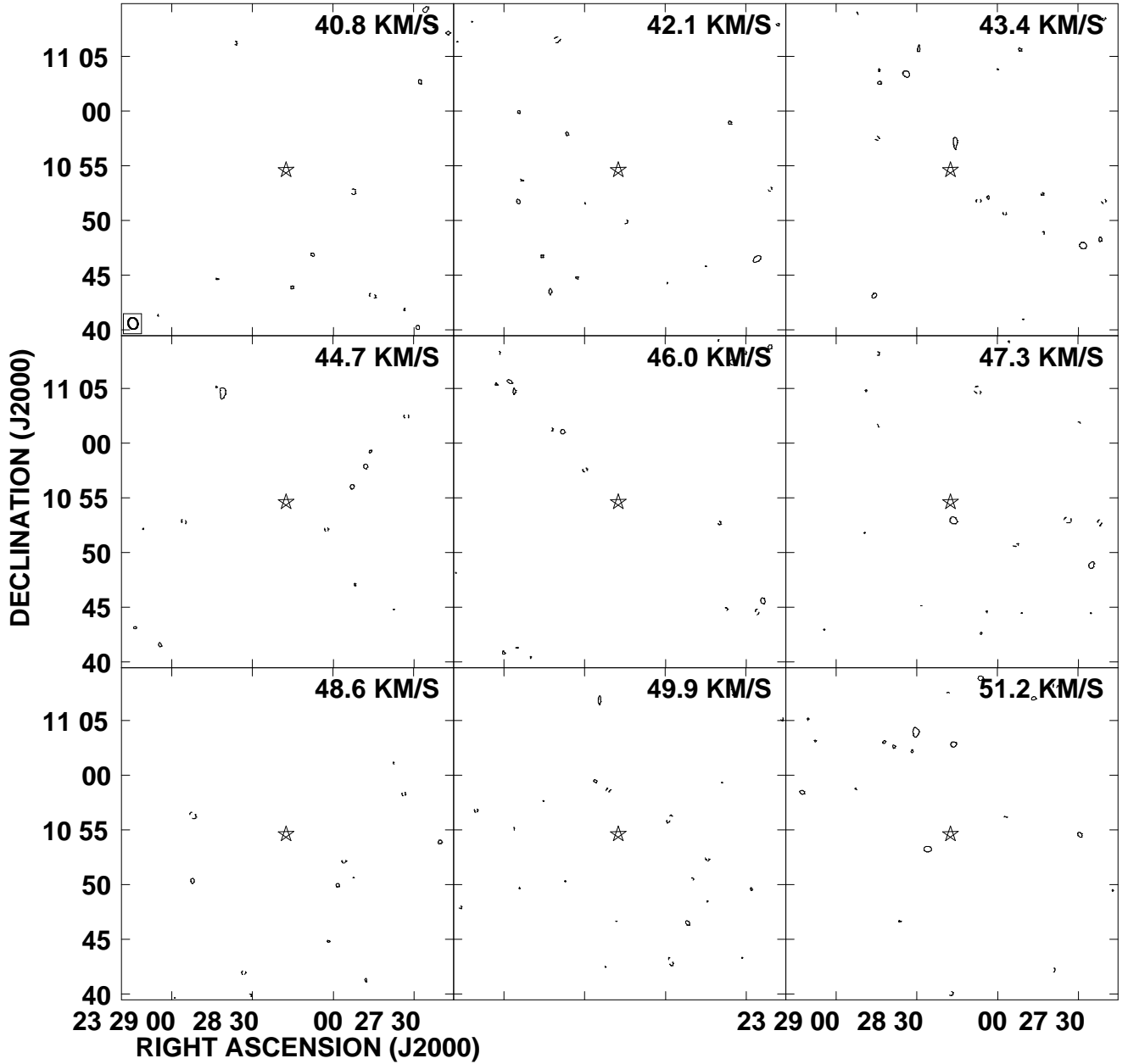


FIG. 21.— HI channel maps bracketing the systemic velocity of AFGL 3099 derived from naturally weighted VLA data. The spatial resolution is $\sim 64'' \times 52''$. A star symbol indicates the stellar position. Contour levels are $(-3, 3, 4, 2[\text{absent}]) \times 1.7 \text{ mJy beam}^{-1}$. The lowest contour is $\sim 3\sigma$. The field-of-view shown is comparable to the VLA primary beam.

the star. However, within this velocity range there are also clear signatures of large-scale emission that is poorly sampled by the VLA. The incomplete spatial sampling of this large-scale emission results in the occurrence of positive and negative bands across the field (see also §4.8.2). These artifacts make it difficult to accurately and unambiguously determine the full extent of the HI wake associated with TX Psc. However, a careful examination of the data does provide some important clues.

In the spectral channel centered at $V_{\text{LSR}} = 11.1 \text{ km s}^{-1}$, a “kink” is visible in the emission trailing to the northeast of TX Psc, near $\alpha_{J2000} = 23^{\text{h}}46^{\text{m}}48^{\text{s}}$, $\delta_{J2000} = 03^{\circ}33'02''$. The presence of this discontinuity raises some doubt that the material east of this position

is related to the circumstellar wake. Furthermore, in the $V_{\text{LSR}} = 8.5$ and 9.8 km s^{-1} velocity channels, an extended HI “cloud” is observed to the northeast of the star whose characteristics suggest that it is not associated with the CSE of TX Psc. This becomes further evident in the HI total intensity map in Figure 24.

Figure 24 highlights a tapering of the emission trailing TX Psc, occurring roughly $8'$ behind the star. This is analogous to what has been observed in the HI wakes of other AGB stars (Matthews et al. 2008, 2011b). However, beyond this, there is a dip in the HI column density followed by an abrupt change in the opening angle of the trailing emission. The marked discontinuity in column density is evident even in the u - v tapered version of our

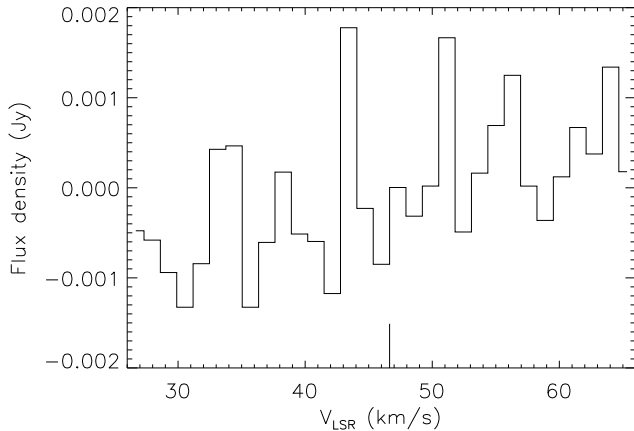


FIG. 22.— VLA H I spectrum of AFGL 3099 obtained by averaging over a single synthesized beam centered on the star. The vertical line indicates the systemic velocity of the star as determined from CO observations.

data where we expect improved sensitivity to extended, low surface brightness emission. Furthermore, the overall morphology of this emission beyond this point (i.e., at $r \gtrsim 8'$ from the star) appears to be generally inconsistent with a circumstellar wake (cf. Villaver et al. 2002, 2012; Wareing et al. 2007a, b, c). While wide-angle circumstellar wakes may indeed arise from mass-losing stars under certain conditions (e.g., Comerón & Kaper 1998; Wareing et al. 2007a; Sahai & Chronopoulos 2010; Matthews et al. 2012), a change from narrow collimation near the star to a broad, wide-angle wake at larger projected distances would be difficult to explain. For these reasons, we conclude that only the gas within $\lesssim 8'$ from TX Psc can be convincingly associated with a trailing circumstellar wake. While we cannot rule out the presence of some additional circumstellar debris beyond this radius (see below), the dominant emission in our VLA maps at these projected distances from the star appears to be interstellar in origin. Under these assumptions, we have derived the spatially integrated H I spectrum of TX Psc shown in (Figure 25). Based on a Gaussian fit to this spectrum (including only data with $V_{\text{LSR}} \geq 8.5 \text{ km s}^{-1}$), we derive a peak H I flux density of $0.35 \pm 0.02 \text{ Jy}$, a line centroid of $V_{\text{LSR}} = 11.4 \pm 0.1 \text{ km s}^{-1}$, and a FWHM line width of $4.0 \pm 0.2 \text{ km s}^{-1}$. From this we measure an integrated H I flux density of $\int S_{\text{HI}} d\nu = 1.48 \pm 0.11 \text{ Jy km s}^{-1}$, translating to an H I mass $M_{\text{HI}} \approx 0.026 M_{\odot}$.

The wake of emission trailing behind TX Psc lies along a position angle of $\sim 45^\circ$, and is thus displaced by -23° compared with a bisector defined by the space motion vector of the star (see Table 5). This suggests the presence of a transverse flow in the local ISM (see below).

Perhaps the most striking feature of the H I emission toward TX Psc is its velocity field (Figure 26). While the velocity field map contains a great deal of spurious structure resulting from undersampled large-scale emission, some noteworthy features are nonetheless apparent, including velocity gradients both parallel and perpendicular to the space motion of the star. These are discussed in detail below.

4.8.2. Discussion of TX Psc Results

TX Psc was previously observed in H I by Gérard & Le Bertre (2006). Its CSE was clearly detected, although the blue edge of the line profile suffered from confusion. Gérard & Le Bertre found evidence that the H I emission associated with TX Psc is quite extended, with a radius of $\sim 12'$. This is significantly larger than the $60\mu\text{m}$ radius of 3:1 reported by Young et al. (1993a) based on *IRAS* data. Similarly, based on higher resolution *Herschel* $70\mu\text{m}$ data, Jorissen et al. (2011) found a source with a total extent of roughly $3'$ (as estimated from their Figure 6), which includes a broad, low surface brightness trail of emission extending toward the northeast. Geise (2011) measured a slightly larger angular extent ($\sim 4.6'$) from a *Spitzer* $70\mu\text{m}$ image.

Examination of H I survey spectra from Kalberla et al. (2003) toward the direction of TX Psc reveals that there is a line component with peak brightness temperature $\sim 2 \text{ K}$ centered near $V_{\text{LSR}} \approx 10 \text{ km s}^{-1}$, very near the systemic velocity of TX Psc. This emission is too strong to be plausibly associated with the CSE of TX Psc, and instead is likely to be interstellar in origin. This emission reveals its presence in our VLA maps as the positive and negative banding seen in our channel images from $V_{\text{LSR}} = 8.5$ to 11.1 km s^{-1} (Figure 23) implying that it is extended over scales of $\gtrsim 15'$ (the maximum angular scales that can be sampled with the VLA in D configuration). The presence of this additional emission component so close in projected position and velocity to TX Psc suggests that the amount of extended emission in the CSE may have been overestimated from the NRT observations. Indeed, the H I mass for the CSE of TX Psc derived from the NRT data is nearly five times larger than we derive from the VLA. While we cannot rule out that the H I wake of TX Psc may include a low surface brightness extension that cannot be readily detected with the VLA (analogous to the one confirmed by the NRT toward Mira; see Matthews et al. 2008), our VLA maps suggest that confusion may preclude a definitive test of this possibility.

A systemic decrease in the radial velocity of gas in extended circumstellar wakes parallel to the direction of motion is expected as a consequence of the gradual deceleration of the wake material owing to its interaction with the ISM (e.g., Wareing et al. 2007c; Raga & Cantó 2008). Indeed, such gradients have been detected in the extended wakes of Mira (Matthews et al. 2008) and X Her (Matthews et al. 2011b). In the case of TX Psc, we likewise see evidence for a systematic blueshifting of the “tail” gas with increasing distance from the star in the H I channel maps (Figure 23) and H I velocity field (Figure 26). The gradient is maximized along a position angle of $\sim 58^\circ$ and has a magnitude of $\sim 1\text{-}2 \text{ km s}^{-1}$ projected in the plane of the sky.

While in principle, quantifying the velocity gradient along a gaseous wake provides a means of age-dating the stellar mass loss history (Matthews et al. 2008, 2011b; Raga & Cantó 2008), our ability to do this for TX Psc is compromised by the presence of a second prominent velocity gradient *perpendicular* to the direction of space motion of the star. The magnitude of this gradient (projected in the plane of the sky) is $\sim 4.5 \text{ km s}^{-1}$ across the width of the H I envelope ($\sim 6'$ or 0.48 pc). This is further illustrated in Figure 27, where we show a position-

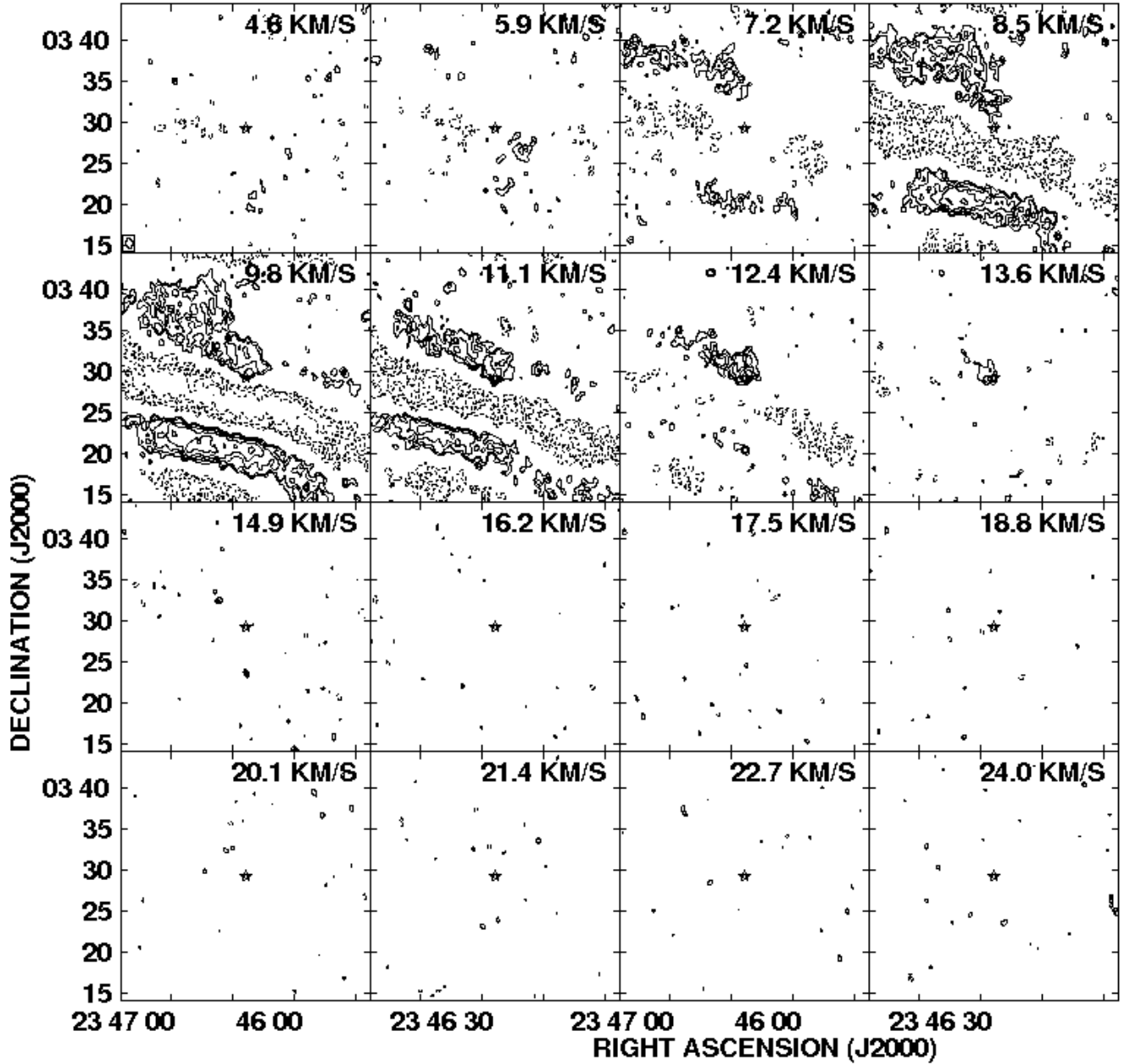


FIG. 23.— HI channel maps bracketing the systemic velocity of TX Psc derived from naturally weighted VLA data. The spatial resolution is $\sim 72'' \times 49''$. A star symbol indicates the stellar position. Contour levels are $(-6, -4.2, -3, 3, 4.2, \dots, 12) \times 2$ mJy beam $^{-1}$. The lowest contour is $\sim 3\sigma$. The field-of-view shown is comparable to the VLA primary beam.

velocity cut across the emission. This perpendicular velocity gradient appears to be real and not an artifact caused by unresolved large-scale structure or its sidelobes in our maps. The most compelling evidence of this is that the velocity gradient persists even at velocities that are uncontaminated by confusion ($V_{\text{LSR}} \geq 12$ km s $^{-1}$). It also persists if we impose u - v restrictions on the data during imaging in order to suppress the short spacings ($u, v < 350\lambda$) that give rise to the spurious large-scale structure in the images. Unfortunately, such u - v restrictions also suppress much of the large-scale emission that appears to be genuinely associated with TX Psc.

For the semi-regular variable X Her, Matthews et al. (2011b) also reported evidence of a velocity gradient or-

thogonal to the direction of space motion in their HI data. In the X Her case, this orthogonal axis corresponds to the symmetry axis of a bipolar outflow previously detected at smaller radii through molecular line observations. Matthews et al. suggested that the HI may therefore be tracing an extension of this outflow out beyond the molecular dissociation radius. Might a similar situation apply to the case of TX Psc?

TX Psc has no published molecular line imaging observations, so it is unknown whether the star has an axisymmetric molecular outflow. Single-dish mapping by Heske et al. (1989) revealed hints of deviations from spherical symmetry, and the CO profile published by Heske (1990) shows a two component line structure, which is

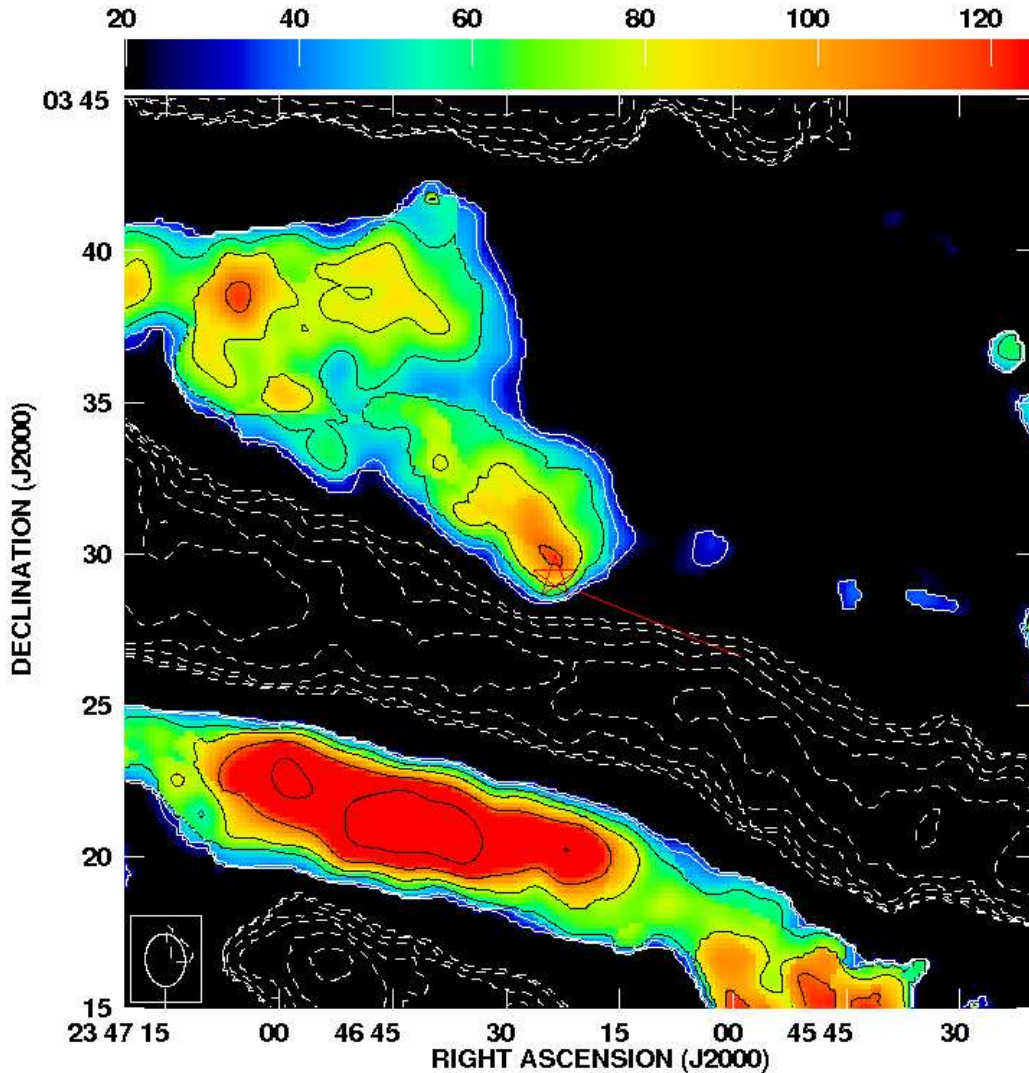


FIG. 24.— H I total intensity map of TX Psc, derived from tapered VLA data, incorporating emission at LSR velocities from 8.5 to 13.6 km s^{-1} . The spatial resolution is $\sim 104'' \times 79''$. A star indicates the stellar position and the red line indicates the direction of space motion. The contour levels are $(-5.6, -4, -2.8, -2, -1.4, -1, 1 \dots 5.6) \times 28 \text{ Jy beam}^{-1} \text{ m s}^{-1}$ and intensity levels are 20 to $125 \text{ Jy beam}^{-1} \text{ m s}^{-1}$. The data have been corrected for primary beam attenuation. The emission associated with the CSE of TX Psc exhibits a head-tail morphology, although the bulk of the emission east of $\alpha_{\text{J2000}} = 23^{\text{h}}46^{\text{m}}48^{\text{s}}$ and north of $\delta_{\text{J2000}} = 03^{\circ}35'35.8''$ is probably unrelated to the star (see text). To minimize noise in the map, data at a given point were blanked if their absolute value did not exceed a 3σ threshold after spatially smoothing the data by a factor of three in velocity and factor of 5 spatially. The positive and negative bands running across the image arise from large-scale interstellar emission that is poorly spatially sampled by the VLA.

frequently a hallmark of stars with bipolar outflows (e.g., Kahane & Jura 1996; Bergman et al. 2000; Josselin et al. 2000; Libert et al. 2010b). The CO mapping data of Heske et al. also show evidence for a spatial offset between the blue and red portions of the line emission along a position angle roughly parallel to the direction of space motion of the star. However, this velocity shift has the opposite sign to the gradient seen in the H I along this direction (i.e., with blueshifted CO emission peaking to the southwest and redshifted CO emission to the northeast).⁹ Another significant problem with this explanation for the velocity gradient transverse to the TX Psc wake is that the velocity gradient appears to persist well beyond the vicinity of the star, where the gas should be

⁹ We assume that right ascension increases to the left in Figure 3 of Heske et al. 1989. However, the signs of the offsets in the x -axis labeling create an ambiguity.

dominated by a turbulent flow of ram pressure stripped material, not the stellar outflow.

An alternative explanation for the velocity gradient orthogonal to its H I wake is the influence of a transverse flow in the local ISM. Evidence for local transverse flows has now been seen in the neighborhood of several other evolved stars (e.g., Ueta et al. 2008; Ferguson & Ueta 2010; Ueta et al. 2010; see also §4.2.2), although the origin of these flows remains unclear. In the case of TX Psc, such a transverse flow could also offer a natural explanation for the offset in position angle between the observed H I wake and the derived space motion vector in Figure 24.

We can attempt to quantify the magnitude and direction of a local ISM flow following the procedure outlined in Ueta et al. (2008). Wilkin (1996) derived an analytic expression that relates the shape of a bow shock surface

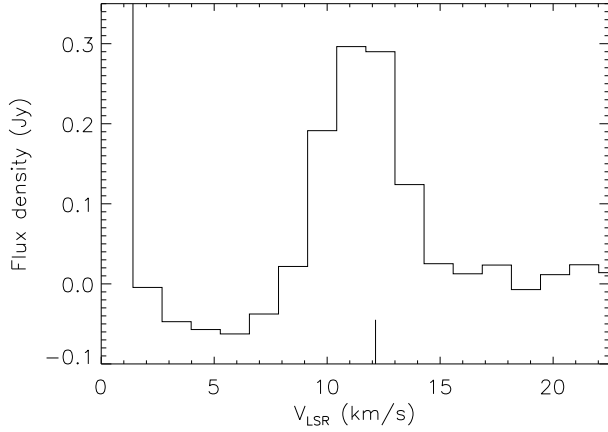


FIG. 25.— Spatially integrated HI spectrum of TX Psc derived from naturally weighted VLA data (after correction for primary beam attenuation). Emission integrated over two adjacent rectangular apertures was summed to produce the final spectrum; the first aperture was $6'2 \times 6'8$, centered at $\alpha_{J2000} = 23^{\text{h}}46^{\text{m}}29.8^{\text{s}}$, $\delta_{J2000} = 03^{\circ}30'27.5''$; the second was $2'8 \times 4'0$, centered at $\alpha_{J2000} = 23^{\text{h}}46^{\text{m}}47.9^{\text{s}}$, $\delta_{J2000} = 03^{\circ}32'42.5''$. The portion of the spectrum blueward of $V_{\text{LSR}} \approx 8 \text{ km s}^{-1}$ is affected by sidelobes from large-scale Galactic emission. The vertical bar indicates the systemic velocity of the star as determined from CO observations.

to its standoff distance, R_0 :

$$R(\theta) = R_0 \csc \theta \sqrt{3(1 - \theta \cot \theta)} \quad (1)$$

where θ is the angular displacement from the bow shock apex as measured from the position of the star, and:

$$R_0 = \sqrt{\frac{\dot{M} V_{\text{out}}}{4\pi \mu m_{\text{H}} n_{\text{H}} V_{\text{space}}^2}}. \quad (2)$$

Here m_{H} is the mass of the hydrogen atom, n_{H} is the HI number density of the local ISM, and μ is the mean molecular weight of the gas (assumed to be 1.3). R_0 effectively defines the locus of ram pressure balance between the internal pressure of the CSE surrounding a mass-losing star and the ram pressure exerted by the ISM due to the star's supersonic space motion.

Based on a three-dimensional fit of Equation 1 to the *Herschel* FIR data of TX Psc, Cox et al. (2012a) derived a deprojected standoff distance, $R_0 = 37''$ (1.52×10^{17} cm), with a position angle and inclination for the bow shock of 238° and 11° , respectively. Inverting Equation 2 and using the fitted R_0 value together with \dot{M} and V_{out} from Table 1, one may then derive the peculiar space velocity of the star with respect to its local ISM: $V'_{\text{space}} \approx 55.6 n_{\text{H}}^{-0.5} \text{ km s}^{-1}$.

Adopting the position angle and inclination of the bow shock from Cox et al., V'_{space} can now be decomposed into its equatorial space-velocity components:

$$V'_{\text{space}} = \begin{bmatrix} V_r \\ V_{\alpha} \\ V_{\delta} \end{bmatrix}_{*,\text{ISM}} = \begin{bmatrix} 10.6 \\ -46.3 \\ -28.9 \end{bmatrix} n_{\text{H}}^{-0.5} \text{ km s}^{-1} \quad (3)$$

From the measured proper motion of TX Psc (see above), the heliocentric Galactic space velocity of the star in equatorial coordinates (see Table 5) can be expressed as

$$V_{\text{space}} = \begin{bmatrix} V_r \\ V_{\alpha} \\ V_{\delta} \end{bmatrix}_{*,\odot} = \begin{bmatrix} 10.8 \\ -60.6 \\ -24.9 \end{bmatrix} \text{ km s}^{-1} \quad (4)$$

The local ISM flow in the vicinity of TX Psc may then be obtained as the difference between V'_{space} and V_{space} :

$$V_{\text{flow}} = V_{\text{space}} - V'_{\text{space}} = \begin{bmatrix} 10.8 & - & 10.6 n_{\text{H}}^{-0.5} \\ -60.6 & - & -46.3 n_{\text{H}}^{-0.5} \\ -24.9 & - & -28.9 n_{\text{H}}^{-0.5} \end{bmatrix} \text{ km s}^{-1} \quad (5)$$

Based on the distance of TX Psc from the Galactic plane (-212 pc; Table 5), the expected ISM density in the vicinity of TX Psc is $n_{\text{H}} \sim 0.2 \text{ cm}^{-3}$ (Table 5). Adopting this value yields $V_{\text{flow}} \approx 60 \text{ km s}^{-1}$ along a position angle $\text{PA} = 338^{\circ}$. While the true value of n_{H} is uncertain, the nominal value predicts a position angle for the flow that corresponds precisely to the direction of the vertical velocity gradient across the TX Psc envelope (Figure 27). It thus seems quite plausible that the velocity gradient across the TX Psc shell results from a transverse ISM flow rather than outflow from the star itself. The direction of the observed velocity gradient is also consistent with this interpretation.

5. GENERAL DISCUSSION

5.1. A Synopsis of HI Imaging Results to Date

The present study now brings the total number of red giants successfully imaged in the HI 21-cm line to 12. These comprise 11 AGB stars and the red supergiant α Ori (see also Bowers & Knapp 1987, 1988; Matthews & Reid 2007; Matthews et al. 2008, 2011a, b; Le Bertre et al. 2012). Including the current study, five additional stars have also been observed with the VLA but were not detected (see also Hawkins & Proctor 1993; Matthews & Reid 2007).¹⁰ This is only a small fraction of the total sample of evolved stars now surveyed in the HI line from single-dish surveys. For a more extensive discussion of HI detection statistics as a function of stellar properties, we therefore direct the reader to the single-dish surveys of Gérard & Le Bertre (2006) and Gérard et al. (2011b). Nonetheless, the imaged sample is now large enough to enable investigation of some emerging trends and to begin to explore how HI properties correlate with other properties of the stars.

We emphasize that the current sample is a biased one in that imaging studies to date have largely (although not exclusively) targeted stars that were already securely detected in HI, based on single-dish surveys (see §2; Matthews & Reid 2007). Additionally, since a portion of the HI imaging sample was chosen to be displaced from the predominant Galactic HI emission along the line-of-sight, the sample may contain a disproportionate number of stars with moderately high space velocities, whose ages and metallicities may not be representative of mean Galactic values.

¹⁰ Knapp & Bowers 1983 presented upper limits on the circumstellar HI content of 16 evolved stars based on VLA snapshot observations; however, several of these stars have been subsequently detected, and the upper limits for the remainder cannot rule out the presence of circumstellar HI at comparable levels.

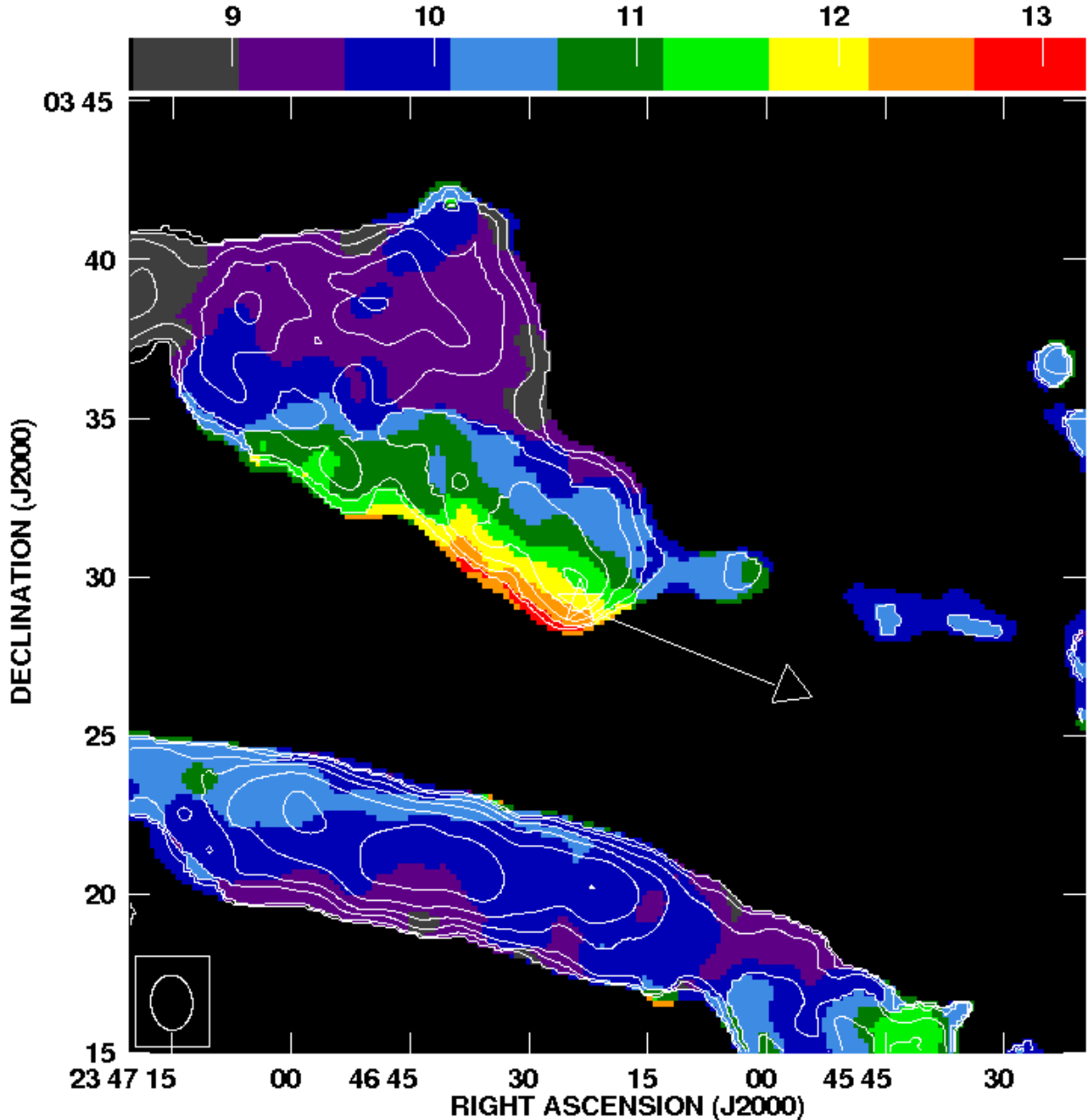


FIG. 26.— Intensity-weighted H I velocity field of TX Psc, derived from tapered VLA data. The spatial resolution is $\sim 104'' \times 79''$. The arrow indicates the direction of space motion of the star. Note the presence of velocity gradients both parallel and perpendicular to the direction of motion. The H I total intensity contours from Figure 24 (positive values only) are overplotted for reference. The color bar shows LSR radial velocity in units of km s^{-1} .

One unifying trend among the stars successfully imaged in H I so far is that in all cases, the H I images and spatially resolved kinematics display evidence for interaction between the CSE and surrounding medium. This local medium includes the ISM, but may also include material shed during earlier mass-loss episodes. Manifestations of this interaction come in several forms, including: (1) *extended wakes, trailing the motions of the stars through space* (hereafter “Category 1”); (2) *quasi-stationary detached shells*, whose properties can be modeled as the slowing of ejected wind material through its interaction with the ISM (hereafter “Category 2”); (3)

arcs or clumps of gas displaced from the stellar position that correlate with bow shocks or other signatures of interaction with the ISM seen at other wavelengths (hereafter “Category 3”). A few stars display features of more than one of these classifications.

To date, five stars have been imaged that display the trailing H I wakes characteristic of Category 1: RX Lep, TX Psc, X Her, Mira, and RS Cnc (see §4.2; §4.8; Matthews & Reid 2007; Matthews et al. 2008, 2011b; Libert et al. 2010b). Among these stars, four have in common relatively high space velocities ($V_{\text{space}} \gtrsim 57 \text{ km s}^{-1}$). This is consistent with the results

TABLE 5
 DERIVED PROPERTIES OF THE SAMPLE

| Name (1) | S_{peak} (Jy) (2) | $\int S d\nu$ (Jy km s ⁻¹) (3) | $V_{\text{LSR,HI}}$ (km s ⁻¹) (4) | ΔV_{HI} (km s ⁻¹) (5) | M_{HI} (M_{\odot}) (6) | θ_{H} ($'$) (7) | V_{space} (km s ⁻¹) (8) | PA ($^{\circ}$) (9) | z (pc) (10) | n_{HI} (cm ⁻³) (11) |
|-------------------|----------------------------------|--|---|--|---|---------------------------------------|--|-----------------------------|---------------------|--|
| Oxygen-rich stars | | | | | | | | | | |
| IK Tau* | ≤ 0.006 | ≤ 0.10 | ... | ... | < 0.001 | ... | > 34.6 | ... | -113 | 0.65 |
| RX Lep | 0.58 ± 0.02 | 2.93 ± 0.22 | 28.4 ± 0.1 | 5.0 ± 0.3 | 0.015 | 17/5 | 56.6 | 24.6 | 54 | 1.16 |
| Y UMa | $0.10 \pm 0.01, 0.03 \pm 0.01$ | 0.63 ± 0.13 | $16.4 \pm 0.2, 17.2 \pm 0.8$ | $3.2 \pm 0.4, 9.2 \pm 2.3$ | 0.022 | 6/8 | 19.2 | 57.1 | 352 | 0.06 |
| R Peg | 0.16 ± 0.01 | 0.76 ± 0.09 | 22.4 ± 0.2 | 4.4 ± 0.4 | 0.029 | $\gtrsim 15'$ | 26.3 | 147.6 | -266 | 0.14 |
| Carbon-rich stars | | | | | | | | | | |
| Y CVn | 0.79 ± 0.02 | 2.68 ± 0.11 | 20.65 ± 0.05 | 3.2 ± 0.1 | 0.047 | 9/ | 31.0 | 36.8 | 273 | 0.13 |
| V1942 Sgr | 0.240 ± 0.009 | 0.82 ± 0.04 | -33.04 ± 0.06 | 3.2 ± 0.1 | 0.055 | 4/6 | 40.2 | 95.1 | -107 | 0.69 |
| AFGL3099* | < 0.0024 | < 0.11 | ... | ... | < 0.058 | ... | > 46.6 | ... | -1081 | 0.00 |
| TX Psc | 0.35 ± 0.01 | 1.48 ± 0.11 | 11.4 ± 0.1 | 4.0 ± 0.2 | 0.026 | $\sim 8'$ | 66.4 | 248.0 | -212 | 0.24 |

NOTE. — Explanation of columns: (1) target name; (2) peak H I flux density in the spatially integrated line profile; upper limits are 3σ ; (3) integrated flux density of the H I line profile, based on a Gaussian fit; (4) LSR velocity of the H I line center based on a Gaussian fit; two values are quoted for multi-component lines (5) FWHM linewidth of the H I profile based on a Gaussian fit; two values are quoted for multi-component lines; (6) H I mass of the CSE derived from the current VLA observations; upper limits are 3σ ; (7) maximum angular extent of the observed circumstellar H I emission; (8) peculiar space velocity (in LSR frame); (9) position angle of space motion projected on the plane of the sky (measured east from north), derived using the prescription of Johnson & Soderblom 1987 and the solar constants from Schönrich et al. 2010; (10) distance from the Galactic plane, estimated as $z \approx d \sin b + 15$ pc,

where values of distance d and Galactic latitude b are taken from Table 1; (11) local ISM number density, estimated from $n_{\text{HI}}(z) = 2.0e^{-\frac{|z|}{100\text{pc}}}$ (Loup et al. 1993), where z is taken from column 10.

* Proper motion measurements are unavailable; no space motion vector was derived.

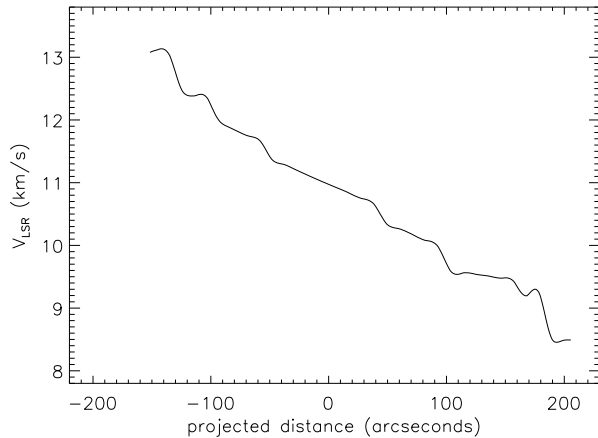


FIG. 27.— Position-velocity cut perpendicular to the direction of space motion of TX Psc, derived from velocity field shown in Figure 26. The cut was extracted along a position angle of 158° and is centered northeast of the stellar position, at $\alpha_{\text{J2000}} = 23^{\text{h}} 46^{\text{m}} 26.8^{\text{s}}$, $\delta_{\text{J2000}} = 03^{\circ} 31' 17.5''$. Negative displacements are to the southeast and positive displacements to the northwest.

of hydrodynamic simulations (e.g., Wareing et al. 2007a; Villaver et al. 2012) that show that high space velocity is one of the primary criteria leading to the development of extended gaseous tails. The one exception is RS Cnc, with $V_{\text{space}} \approx 12.4$ km s⁻¹. This star is located relatively close to the Galactic plane ($z \approx 97$ pc), so its H I tail may be enhanced through the effects of a high local ISM density. Simulations also show that cometary tails may form very early in the AGB stage even for stars with low space velocities (Villaver et al. 2012). Furthermore, since the proper motion values for this star have large uncertainties (van Leeuwen 2007), the space velocity may be underestimated.

One feature in common to all of the stars so far found to have extended gaseous wakes is that their mean effective temperatures are high enough ($T_{\text{eff}} > 2500$ K) such that their winds are predicted to be dominated by atomic hydrogen (Glassgold & Huggins 1983). In addition, all

five stars have mass loss rates within a narrow range of values $\dot{M} \approx (1 - 3) \times 10^{-7} M_{\odot} \text{ yr}^{-1}$, despite a range of outflow velocities and variability classes.

The current study has identified four stars belonging to Category 2 (i.e., that appear to be surrounded by quasi-stationary detached shells): RX Lep (§4.2), Y UMa (§4.3), Y CVn (§4.5), and V1942 Sgr (§4.6). The red supergiant α Ori (Le Bertre et al. 2012) also falls into this category. All four of the AGB stars in this category have mass-loss rates in the same narrow range as the stars with H I tails [$\dot{M} \approx (1 - 3) \times 10^{-7} M_{\odot} \text{ yr}^{-1}$]. However, the space velocities of these stars (Table 5) are on average lower, ranging from 19.2 km s⁻¹ for Y UMa to 56.6 km s⁻¹ for RX Lep (which also exhibits an extended H I tail). Similarly, α Ori has $V_{\text{space}} \approx 31$ km s⁻¹ (Le Bertre et al. 2012). Our imaging confirms that detached H I shells with similar properties can occur in both carbon-rich and oxygen-rich stars. As already suggested by Libert et al. (2007), the formation mechanism for these H I shells is almost certainly different from the thin molecular shells seen around some carbon stars (cf. Schöier et al. 2005; Olofsson et al. 2010). Some key differences are that the molecular shells are extremely thin and nearly perfectly circular, whereas the H I shells are geometrically thick and have shapes ranging from irregular to boxy to egg-shaped.

We have presented the results of simple numerical modeling of the four AGB H I shells from which we estimate ages in the range 9.0×10^4 to 7.2×10^5 yr (Appendix A; see also Le Bertre et al. 2012 for the case of α Ori). For Y UMa, the age that we derive for the CSE is comparable to that previously derived from FIR observations by Young et al. (1993b). However, for Y CVn and V1942 Sgr (both carbon stars) the duration of the mass loss history inferred from our new H I observations is nearly 7 times larger than derived previously from FIR observations. Indeed, as more H I measurements of the extended CSEs become available, they continue to point toward a past systematic underestimation of the mass loss timescales for many red giants (see also Matthews et al. 2008, 2011b; Le Bertre et al. 2012).

One of the stars recently identified as belonging to Category 3 (i.e., stars surrounded by arcs or clumps of gas displaced from the stellar position) is α Ori (Le Bertre et al. 2012), while the other two stars we place in this class, IRC+10216 and R Cas (Matthews & Reid 2007; Matthews et al. 2011a), are Mira variables. All three of these stars have high mass-loss rates ($\dot{M} > 1 \times 10^{-6} M_{\odot} \text{ yr}^{-1}$), although α Ori has a much higher effective temperature ($T_{\text{eff}} = 3641 \pm 53 \text{ K}$; Perrin et al. 2004) compared with the two Miras ($T_{\text{eff}} \lesssim 2500 \text{ K}$). For both IRC+10216 and R Cas, the H I imaged by the VLA comprises isolated arcs of emission displaced from the stellar position, although the two stars differ dramatically in the size scales of their CSEs (cf. Matthews & Reid 2007), and they are believed to be at very different evolutionary stages. In the case of IRC+10216, it is suspected that the observed H I emission is partly the result of swept-up interstellar material, although there is evidence that it is augmented by photodissociated H₂ (Matthews et al. 2011a).

Only one star imaged in H I to date, the Mira variable R Peg, does not fall neatly into any of the three classifications defined above. While its H I mass and integrated H I profile are similar to the other detected stars, its morphology is rather peculiar (§4.4). R Peg has a higher mass loss rate than any of the other VLA sample stars where H I has been detected directly toward the stellar position ($\dot{M} \approx 5 \times 10^{-7} M_{\odot} \text{ yr}^{-1}$), suggesting that it may be somewhat more evolved. In this case, one possibility is that the ejecta that we observe in H I are left over from previous cycles of mass loss and have been subsequently distorted by transverse flows in the surrounding ISM.

For all stars detected in H I so far, we have estimated the number density of hydrogen atoms in the local ISM using the expression from Loup et al. (1993): $n_{\text{H}}(z) = 2.0e^{-\frac{|z|}{100\text{pc}}} \text{ cm}^{-3}$, where z is the distance from the Galactic Plane in pc, estimated as $z \approx d \sin(b) + 15 \text{ pc}$. Here d is the distance to the star and b is the Galactic latitude. For the full VLA-detected sample, the values range from $n_{\text{H}} \sim 0.059 \text{ cm}^{-3}$ for Y UMa (Table 5) to $n_{\text{H}} \sim 1.7 \text{ cm}^{-3}$ for α Ori and R Cas. For the Category 1 stars, values of n_{H} range from 0.24 cm^{-3} for TX Psc to 1.2 cm^{-3} for RX Lep (Table 5). Thus there is no evidence that trailing H I wakes are preferentially found associated with stars in dense local environments, although as noted in §4.2.2, the moderately high local ISM density surrounding RX Lep may help to account for its highly collimated wake. We also emphasize that the n_{H} values computed using the above formula are rather uncertain owing to their dependence on the adopted Galactic model and small-scale fluctuations in the ISM density across the Galaxy.

The sample of five stars so far undetected in H I with the VLA is still too small to draw any firm conclusions, but here we briefly review their properties to help guide future studies. First, we point out that the two undetected stars from the current study, IK Tau and AFGL 3099, have temperatures and mass loss rates comparable to two previously detected Category 3 Miras: R Cas and IRC+10216. However, Gérard et al. (2011b) have found that in general, cooler stars with higher mass loss rates are less frequently detected in H I. This may

be due to a combination of a predominantly molecular composition in the CSEs, their geometrically large sizes, and/or temperatures in the CSE that are too cool to allow the detection of H I in emission (see §4.1.2).

Having a low mass loss rate does not necessarily imply that a star should be more difficult to detect in H I, since available \dot{M} estimates generally represent only recent mass loss and are derived from tracers at much smaller radii than the extended circumstellar material traced by H I. However, to date, the two stars observed with the VLA having the lowest mass loss rates both remain undetected. The Mira R Aqr ($\dot{M} = 6 \times 10^{-8} M_{\odot} \text{ yr}^{-1}$; Spergel et al. 1983) is part of a symbiotic binary and is surrounded by a hot ionized region. Matthews & Reid (2007) placed an upper limit on its H I mass of $M_{\text{HI}} < 4.9 \times 10^{-4} M_{\odot}$. The undetected semi-regular variable W Hya (Hawkins & Proctor 1993) also has a comparably small mass loss rate ($\dot{M} \approx 7 \times 10^{-8} M_{\odot} \text{ yr}^{-1}$; Olofsson et al. 2002). In this case, the lack of detection might be related to the moderately cool stellar temperature ($T_{\text{eff}} \approx 2450 \text{ K}$; Feast 1996) or the difficulty of disentangling weak and clumpy CSE emission from line-of-sight contamination (see Hawkins & Proctor 1993).

The remaining star so far undetected in H I by the VLA is the semi-regular variable EP Aqr, whose mass loss rate is an order of magnitude higher than R Aqr or W Hya ($\dot{M} \approx 6 \times 10^{-7} M_{\odot} \text{ yr}^{-1}$; Winters et al. 2007). It poses an interesting case, since it is not a known binary, and its effective temperature is high enough to predict the presence of atomic hydrogen in its atmosphere ($T_{\text{eff}} \approx 3240 \text{ K}$; Dumm & Schild 1998). The non-detection of this star with the VLA is particularly puzzling, as Le Bertre & Gérard (2004) reported an H I detection of EP Aqr with the NRT, and the star is also an extended FIR source (Young et al. 1993a; Cox et al. 2012a). However, Matthews & Reid (2007) found only a few isolated clumps of H I in the region, none of which could be unambiguously linked with the CSE. Deeper observations of this star with improved u - v coverage might be enlightening, as some of the clumps detected by Matthews & Reid might turn out to be density enhancements in an extended, diffuse envelope or pockets of photodissociated gas within an ancient molecular envelope.

5.2. Future Prospects

It is clear that H I imaging studies of larger samples of stars are needed to enable better statistical comparisons between the properties of the stars, their CSEs, and their interstellar neighborhoods. However, despite the small size of the current VLA H I sample, certain trends are already clear. The results to date underscore initial findings from single-dish surveys and unambiguously establish the importance of the interstellar environment on the large-scale properties of CSEs. While additional examples of stars interacting with their environments have also been identified in recent FIR and FUV surveys (e.g., Martin et al. 2007; Stencel 2009; Sahai & Chronopoulos 2010; Ueta 2011; Cox et al. 2012a), H I data have the unique advantage that they supply *kinematic* information on the extended circumstellar material. As demonstrated in the present study, such data in turn permit numerical modeling of the interaction between circum-

stellar shells and their surroundings and the determinations of the duration of the stellar mass loss history (see also Matthews et al. 2008, 2011b; Libert et al. 2007, 2010a, b). HI data can also provide crucial morphological and kinematic information for testing hydrodynamic simulations of individual mass-losing stars moving through the ISM—a potential that has largely gone untapped (cf. Villaver et al. 2012; Wareing 2012; Mohamed et al. 2012).

Another important lesson that has emerged from HI imaging surveys to date is that no single tracer can provide a complete picture of the complex circumstellar environments of mass-losing evolved stars. If one hopes to understand the complete stellar mass loss history, it is critical to study the CSE on both large and small spatial scales. Moreover, it has become clear that even when different tracers span overlapping spatial scales (e.g., HI and FIR-emitting dust), each supplies unique yet complementary information that can be used together to provide a more comprehensive picture of the kinematics, physical conditions, and chemistry across the entire CSE.

6. SUMMARY

We have presented HI 21-cm line imaging observations of a sample of eight AGB stars obtained with the VLA. We have unambiguously detected HI emission associated with the CSEs of six of the stars. All six of these stars were already known to have atomic hydrogen in their CSEs based on the results of single-dish surveys. However, our imaging results reveal a wealth of new information on their spatially resolved morphologies and kinematics. In all cases we identify clear evidence that the properties of the extended CSEs are significantly affected by interaction with their local interstellar environments. The detected stars have circumstellar HI masses in the range $M_{\text{HI}} \approx 0.015 - 0.055 M_{\odot}$ and the size scales of their circumstellar HI emission range from ~ 0.6 to 1.7 pc.

Four stars in the present study (RX Lep, Y UMa, Y CVn, and V1942 Sgr) are found to be surrounded by quasi-stationary detached hydrogen shells whose origin can be explained as a result of the stellar outflow being abruptly decelerated at a termination shock that occurs at the interface between the circumstellar and interstellar environments. These shells are seen around both oxygen-rich and carbon-rich stars, and appear to have a different origin from the thin detached molecular shells seen around some carbon stars. All four HI shell stars have similar mass-loss rates [$\dot{M} \approx (1-3) \times 10^{-7} M_{\odot} \text{ yr}^{-1}$] and low-to-moderate space velocities, but otherwise show a range in properties, including chemistries, wind outflow velocities, and variability classes. All of the shells have a clumpy rather than smooth structure, and none of the observed HI shells are spherical; they range from egg-shaped (RX Lep) to boxy (Y CVn) to amorphous (Y UMa and V1942 Sgr). In the case of Y UMa, there is evidence that one edge of the shell was distorted through its interaction with the local ISM. The shell of RX Lep exhibits a pronounced elongation along the direction of space motion of the star, as well as a “cracked egg” morphology, with a dearth of emission along its equatorial region.

Based on simple numerical models we have estimated ages for the four shells in the range 9.0×10^4 to 7.2×10^5 yr (Appendix A). These results support previous sugges-

tions that RX Lep is in a relative early evolutionary state compared with the other three stars. For the carbon stars Y CVn and V1942 Sgr the derived ages also imply that mass loss time scales previously derived from FIR measurements have been underestimated by a factor of ~ 7 .

For both Y UMa and Y CVn, high-resolution FIR images are available that reveal counterparts of the HI-emitting shells. In both cases, the extent of the FIR shell is comparable to that of the HI shell, but the two tracers show notable differences, perhaps due to effects such as ionization of the HI from shocks or local destruction of dust grains. Both Y UMa and Y CVn also exhibit “notch”-like depressions in their HI and FIR intensity along the leading edge of their HI shells and running parallel to their direction of space motion. These notches may be signatures of instabilities along the leading edge of the CSE. While the HI shells of Y UMa and Y CVn are similar in terms of their sizes, morphologies, and line widths, the Y UMa shell contains only half the HI mass as that of Y CVn and also shows a distinct rotationally symmetric pattern in its HI velocity field whose origin is unclear.

The two highest velocity stars in our study (RX Lep and TX Psc) were found to have extended gaseous wakes trailing the motions of the stars through the Galaxy. Such wakes are formed by the effects of ram pressure on the circumstellar ejecta as the stars move supersonically through the ISM. The wake of RX Lep (which stretches ~ 0.36 pc) is more highly collimated than any HI wake detected to date, a fact that is likely due to a combination of the relatively early evolutionary status of the star on the TP-AGB and the high density of its interstellar surroundings. For TX Psc, the orientation of the wake (which stretches ~ 0.6 pc) appears to be affected by a local transverse flow in the ISM. This flow could also explain a velocity gradient observed across the CSE, perpendicular to the direction of space motion.

We find the oxygen-rich Mira R Peg to be surrounded by a peculiar “horseshoe”-shaped HI nebula that extends over ~ 1.7 pc on the sky. This morphology may result in part from the effects of local ISM flows. However, the CSE morphology close to the stellar position is also peculiar, with two asymmetric lobes of emission stretching roughly parallel to the direction of space motion of the star. These lobes differ from the head-tail structures seen toward other stars in that the “head” of the nebula lies at a projected distance of ~ 0.1 pc southeast of the star. One possible explanation is that the observed HI structures are the vestiges of an earlier cycle of mass-loss.

The two undetected stars in the present sample (IK Tau and AFGL 3099) are both relatively cool Mira variables with high mass-loss rates [$\dot{M} \approx (4.2, 13) \times 10^{-6} M_{\odot} \text{ yr}^{-1}$]. Both stars were also undetected in previous single-dish studies. For these stars, hydrogen in the circumstellar environment may be too cold to detect via 21-cm line emission or may be largely in molecular form.

LDM acknowledges support for this work from grant AST-1009644 from the National Science Foundation. MCJ was supported through a National Science Foundation Research Experience for Undergraduates grant to MIT Haystack Observatory. The observations presented here were part of NRAO programs AM887 and AM1001

and archival program AK237. This research has made use of the SIMBAD database, operated at CDS, Strasbourg, France.

APPENDIX

AGE ESTIMATES FOR THE DETACHED H I SHELLS BASED ON SIMPLE NUMERICAL MODELS

As a mass-losing star becomes progressively surrounded by an expanding shell of circumstellar material, the collision of the supersonic stellar wind with the surrounding medium (local ISM and/or debris from earlier episode of mass loss) produces a slowly expanding shell of denser material (Lamers & Cassinelli 1999). Young et al. (1993b) developed a model to simulate the formation of these “detached shells” as seen in infrared emission, and Libert et al. (2007) subsequently adapted this type of modeling to circumstellar hydrogen.

In this picture, a detached shell results from a stellar outflow that is abruptly slowed down at a termination shock. This first shock defines the inner boundary of the detached shell (r_1). The outer limit (r_2) is defined by the leading edge (bow shock) where external matter is compressed by the expanding shell (see Figure 5 of Libert et al. 2007). Between these two limits, the detached shell is composed of compressed circumstellar and interstellar matter separated by a contact discontinuity at a radius r_f . The circumstellar matter is decelerated and heated when crossing the shock at r_1 . As it cools from a temperature T_1^+ (at r_1) to T_f (at r_f), the expansion velocity decreases, from v_1^+ to v_f , and the density increases from n_1^+ to n_f^- . Adopting an arbitrary temperature profile, one can numerically solve the equation of motion between r_1 and r_f .

Here we have applied a similar method to modeling the H I shells of RX Lep, Y UMa, Y CVn, and V1942 Sgr. Models for three of the stars (RX Lep, Y CVn, and V1942 Sgr) have previously been published based on single-dish H I observations (Libert et al. 2007, 2008, 2010a), but our new imaging observations provided improved constraints on the model parameters.

We have not attempted to compute models for either TX Psc or R Peg. In the case of TX Psc, the relative high space velocity and large fraction of the circumstellar ejecta present in its extended trailing wake makes it a poor candidate for a stationary and spherically symmetric model. For R Peg, the complex H I morphology and line shape also imply that a simple model fit of the type described here is unlikely to be meaningful.

Following Libert et al. (2008), the temperature profile in the detached shell of the four modeled stars is constrained by the observed H I line profile. For the external part of the detached shell (between r_f and r_2), we assume a density profile that falls off as $1/r^2$, with the condition that the total mass ($M_{DT,CS}$) is given by the equivalent ISM mass enclosed in a sphere of radius r_2 . Inside r_1 , we assume a spherical wind in uniform expansion, whose properties (mass-loss rate, outflow velocity, and systemic velocity) match those derived from CO observations (Table 1). We assume mass lost from the star comprises 90% H atoms and 10% He atoms by number (Glassgold & Huggins 1983). The outer radius of the shell, r_f , is constrained by the VLA images.

Based on our models, the detached shell is expected to produce a narrow, quasi-Gaussian emission peak at or near the stellar systemic velocity in the spatially integrated spectrum, while the freely expanding wind should produce a weaker, broader line component with peaks located on either side of the stellar systemic velocity, near $V_\star \pm V_o$ (see Le Bertre et al. 2012). In general, the shell component dominates the global spectral profile.

Our best-fit parameters for the four stars that we have modeled are summarized in Table A1, and model fits are overlotted on the observed spectra in Figure 28. In all cases, our toy model provides a reasonable fit to the strength and width of the global H I line profile.

For the present study, the most useful outcome of our models is an estimate for the age of each of the shells, which can be obtained from a sum of the parameters t_1 and t_{DS} in Table A1. Not surprisingly, we find the smallest age ($\sim 90,000$ yr) for RX Lep, a star that is believed to be in the early stages of the TP-AGB (see §4.2). For the other three stars, our models imply that the H I data are tracing more than 10^5 years of stellar mass loss history. In the case of Y UMa, our derived shell age is comparable to the age of the FIR-emitting shell previously derived by Young et al. 1993b (9.2×10^4 yr), while in the cases of the carbon stars Y CVn and V1942 Sgr, our new values are 6.8 and 6.6 times larger, respectively.

To obtain a more complete picture of these four stars, future models will ultimately need to take into account the motion of the stars through the ISM and the resulting distortions that this produces on the H I shells. However, this will require sophisticated hydrodynamic simulations that are beyond the scope of the present paper. Furthermore, we note that our model fits break down at small radii ($r \lesssim r_1$), systematically predicting more flux than is observed in both the shell component (central peak) of the line profile and the freely expanding wind (“horns”). This may be due to an uncertainty in the temperature profile adopted in our models, short-term fluctuations in the mass-loss rate, asymmetric or non-spherical mass loss, and/or a breakdown in our assumption that the wind is largely atomic as it leaves the star. These possibilities will be investigated in a future work. Fortunately the ages that we derive for the detached shells (Table A1) depend mostly on their large-scale properties and are relatively insensitive to these details.

REFERENCES

- Begum, A. et al. 2010, ApJ, 722, 395
 Bergeat, J., Knapik, A., & Rutily, B. 2001, A&A, 369, 178
 Bergeat, J., Knapik, A., & Rutily, B. 2002, A&A, 390, 967
 Bergman, P., Kerschbaum, F., & Olofsson, H. 2000, A&A, 353, 257
 Bowers, P. F. & Knapp, G. R. 1987, ApJ, 315, 305
 Bowers, P. F. & Knapp, G. R. 1988, ApJ, 332, 299
 Castro-Carrizo, A. et al. 2010, A&A, 523, A59
 Chiotellis, A., Schure, K. M., & Vink, J. 2012, A&A, 537, A139
 Claussen, M. J., Sjouwerman, L. O., Rupen, M. P., Olofsson, H., Schöier, F. L., Bergman, P., & Knapp, G. R. 2011, ApJ, 739, L5

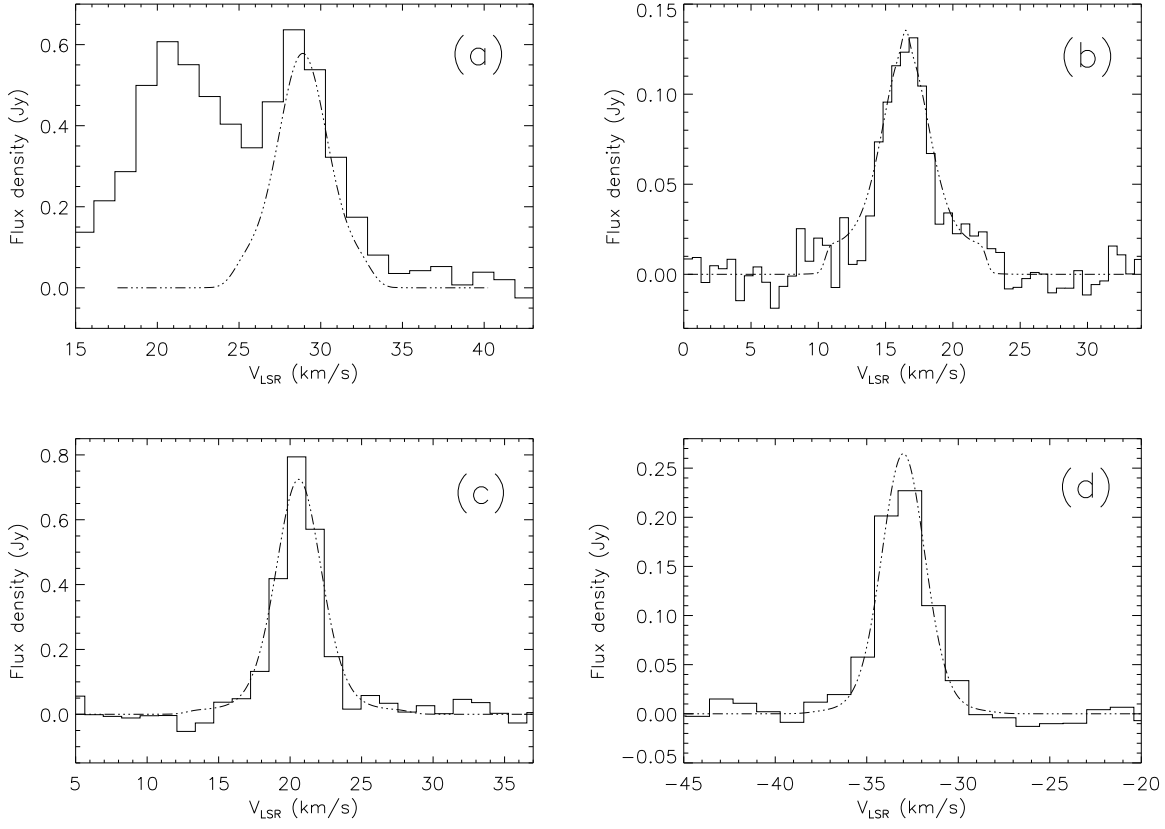


FIG. 28.— Global (spatially integrated) H I spectra for four stars from the current sample (solid histograms), with spectra derived from numerical models overplotted (dot-dash lines; see Appendix A): (a) RX Lep; (b) Y UMa; (c) Y CVn; (d) V1942 Sgr. The model spectra have been smoothed to match the spectral resolution of the observations. For RX Lep, the spectral peak blueward of the stellar emission results from interstellar contamination.

TABLE 1
DETACHED SHELL MODEL PARAMETERS

| Parameter | RX Lep | Y UMa | Y CVn | V1942 Sgr |
|--|----------------------|----------------------|-----------------------|----------------------|
| \dot{M} ($M_{\odot} \text{ yr}^{-1}$) | 2.0×10^{-7} | 2.6×10^{-7} | 1.7×10^{-7} | 1.0×10^{-7} |
| μ | 1.3 | 1.3 | 1.3 | 1.3 |
| t_1 (yr) | 2.0×10^4 | 3.6×10^4 | 2.8×10^4 | 2.4×10^4 |
| t_{DS} (yr) | 7.0×10^4 | 8.8×10^4 | 4.2×10^5 | 7.0×10^5 |
| r_1 (pc) | 0.087 (2'0) | 0.22 (2'0) | 0.22 (2'8) | 0.12 (0'8) |
| r_f (pc) | 0.11 (2'6) | 0.26 (2'3) | 0.32 (4'0) | 0.22 (1'4) |
| r_2 (pc) | 0.17 (4') | 0.34 (3'0) | 0.40 (5'1) | 0.44 (2'8) |
| $T_0 (\equiv T_1^{-1}), T_1^+$ (K) | 20, 528 | 20, 1071 | 20, 1804 | 20, 746 |
| $T_f (\equiv T_2^+)$ (K) | 157 | 221 | 173 | 87 |
| $v_0 (\equiv v_1^+), v_1^+$ (km s^{-1}) | 4.2, 1.07 | 6.0, 1.52 | 7.8, 1.96 | 5.0, 1.27 |
| v_f (km s^{-1}) | 0.16 | 0.18 | 0.07 | 0.04 |
| v_2 (km s^{-1}) | 1.35 | 1.2 | 1.0 | 1.26 |
| n_1^-, n_1^+ (H cm^{-3}) | 14.0, 54.8 | 1.9, 7.55 | 1.0, 3.8 | 2.8, 11.2 |
| n_f^-, n_f^+ (H cm^{-3}) | 228, 2.3 | 45.0, 0.5 | 50.0, 0.6 | 119, 1.6 |
| n_2 (H cm^{-3}) | 1.0 | 0.2 | 0.4 | 0.4 |
| $M_{r < r_1}$ (M_{\odot}) | 4.0×10^{-3} | 9.5×10^{-3} | 4.8×10^{-3} | 2.4×10^{-3} |
| $M_{\text{DT,CS}}$ (M_{\odot}) | 1.4×10^{-2} | 2.3×10^{-2} | 7.17×10^{-2} | 7.0×10^{-2} |
| $M_{\text{DT,EX}}$ (M_{\odot}) | 7.7×10^{-4} | 1.1×10^{-3} | 2.4×10^{-3} | 7.3×10^{-3} |

NOTE. — Notations follow those adopted by Libert et al. 2007. Matter lost is assumed to be 90% neutral hydrogen, 10% helium by number density. Distances are adopted from Table 1.

- Clayton, G. C. 2012, *JAVSO*, 40, 539
- Comerón, F. & Kaper, L. 1998, *A&A*, 338, 273
- Condon, J. J., Cotton, W. D., Greisen, E. W., Yin, Q. F., Perley, R. A., Taylor, G. B., & Broderick, J. J. 1998, *AJ*, 115, 1693
- Cox, N. et al. 2012a, *A&A*, 537, A35
- Cox, N. et al. 2012b, *A&A*, 543, C1
- Cristallo, S., Straniero, O., Gallino, R., Piersanti, L., Domínguez, I., & Lederer, M. T. 2009, *ApJ*, 696, 797
- Decin, L. et al. 2010, *A&A*, 521, L4
- Dickinson, D. F. & Dinger, A. S. C. 1982, *ApJ*, 254, 136
- Dominy, J. F. 1984, *ApJS*, 55, 27
- Dumm, T. & Schild, H. 1998, *New Astron.*, 3, 137
- Dyck, H. M., Lockwood, G. W., & Capps, R. W. 1974, *ApJ*, 189, 89
- Eriksson, K., Gustafsson, B., Johnson, H. R., Querci, F., Querci, M., Baumert, J. H., Carlsson, M., & Olofsson, H. 1986, *A&A*, 161, 305
- Feast, M. W. 1996, *MNRAS*, 278, 11
- Feast, M. W., Whitelock, P. A., Catchpole, R. M., Roberts, G., & Carter, B. S. 1985, *MNRAS*, 215, 63P
- Ferguson, B. A. & Ueta, T. 2010, *ApJ*, 711, 613
- Gardan, E., Gérard, E., & Le Bertre, T. 2006, *MNRAS*, 365, 245
- Geise, K. M. 2011, Masters Thesis, University of Denver
- Gehrz, R. D., Hackwell, J. A., & Briotta, D. 1978, *ApJ*, 221, L23
- Gérard, E. & Le Bertre, T. 2003, *A&A*, 397, L17
- Gérard, E. & Le Bertre, T. 2006, *AJ*, 132, 2566
- Gérard, E., Le Bertre, T., & Libert, Y. 2011a, in *Why Galaxies Care about AGB Stars*, ASP Conf. Series Vol. 445, edited by F. Kerschbaum, T. Lebzelter, and R.F. Wing, 329
- Gérard, E., Le Bertre, T., & Libert, Y. 2011b, in *SF2A-2011: Proceedings of the Annual Meeting of the French Society of Astronomy and Astrophysics*, edited by G. Alecian, K. Belkacem, R. Samadi, and D. Valls-Gabaud, 419
- Glassgold, A. E. & Huggins, P. J. 1983, *MNRAS*, 203, 517
- González Delgado, D., Olofsson, H., Kerschbaum, F., Schöier, F. L., Lindqvist, M., & Groenewegen, M. A. T. 2003, *A&A*, 411, 123
- Groenewegen, M. A. T. & Whitelock, P. A. 1996, *MNRAS*, 281, 1347
- Hawkins, G. & Proctor, D. 1993, in *Mass Loss on the AGB and Beyond*, ed. H. E. Schwarz (ESO: Munich), 461
- Heske, A. 1990, *A&A*, 229, 494
- Heske, A., te Lintel Hekkert, P., & Maloney, P. R. 1989, *A&A*, 218, L5
- Imai, H., Obara, K., Diamond, P. J., Omodaka, T., & Sasao, T. 2002, *Nature*, 417, 829
- Inomata, N., Imai, H., & Omodaka, T. 2007, *PASJ*, 59, 799
- Isaacman, R. 1979, *A&A*, 77, 327
- Izumiura, H., Hashimoto, O., Kawara, K., Yamamura, I., & Waters, L. B. F. M. 1996, *A&A*, 315, L221
- Johnson, D. R. H. & Soderblom, D. R. 1987, *AJ*, 93, 864
- Jorissen, A. et al. 2011, *A&A*, 532, 135
- Josselin, E., Maun, N., Planesas, P., & Bachiller, R. 2000, *A&A*, 362, 255
- Judge, P. G. & Stencel, R. E. 1991, *ApJ*, 371, 357
- Jura, M. 1986, *ApJ*, 303, 327
- Jura, M., Kahane, C., & Omont, A. 1988, *A&A*, 201, 80
- Jura, M. & Kleinmann, S. G. 1992, *ApJS*, 79, 105
- Kahane, C. & Jura, M. 1996, *A&A*, 310, 952
- Kalberla, P. M. W., Burton, W. B., Hartmann, D., Arnal, E. M., Bajaja, E., Morras, R., & Pöppel, W. G. L. 2005, *A&A*, 440, 775
- Kiss, L. L., Sztarmáry, K., Cadmus, R. R. Jr., & Mattei, J. A. 1999, *A&A*, 346, 542
- Klotz, D., Paladini, C., Hron, J., Aringer, B., Sacuto, S., Marigo, P., & Verhoelst, T. 2013, submitted to *A&A* (arXiv:1301.0404)
- Knapp, G. R. & Bowers, P. F. 1983, *ApJ*, 266, 701
- Knapp, G. R. & Morris, M. 1985, *ApJ*, 292, 640
- Knapp, G. R., Pourbaix, D., Platais, I., & Jorissen, A. 2003, *A&A*, 403, 993
- Knapp, G. R., Young, K., Lee, E., & Jorissen, A. 1998, *ApJS*, 117, 209
- Lambert, D. L., Gustafsson, B., Eriksson, K., & Hinkle, K. H. 1986, 62, 373
- Lamers, H. J. G. L. M. & Cassinelli, J. P. 1999, *Introduction to Stellar Winds* (Cambridge University Press: Cambridge)
- Le Bertre, T. 1992, *A&AS*, 94, 377
- Le Bertre, T. 1993, *A&AS*, 97, 729
- Le Bertre, T. & Gérard, E. 2001, *A&A*, 378, 29
- Le Bertre, T. & Gérard, E. 2004, *A&A*, 419, 549
- Le Bertre, T., Matsuura, M., Winters, J. M., Murakami, H., Yamamura, I., Freund, M., & Tanaka, M. 2001, *A&A*, 376, 997
- Le Bertre, T., Matthews, L. D., Gérard, E., & Libert, Y. 2012, *MNRAS*, 422, 3433
- Le Bertre, T. & Winters, J. M. 1998, *A&A*, 334, 173
- Lebzelter, T. & Hinkle, K. H. 2002, *A&A*, 393, 563
- Lebzelter, T. & Hron, J. 1999, *A&A*, 351, 533
- Le Sidaner, P. & Le Bertre, T. 1996, *A&A*, 314, 896
- Leitner, S. N. & Kravtsov, A. V. 2011, *ApJ*, 734, 48
- Libert, Y., Gérard, E., & Le Bertre, T. 2007, *MNRAS*, 380, 1161
- Libert, Y., Le Bertre, T., Gérard, E., & Winters, J. M. 2008, *A&A*, 491, 789
- Libert, Y., Gérard, E., Thum, C., Winters, J. M., Matthews, L. D., & Le Bertre, T. 2010a, *A&A*, 510, 14
- Libert, Y., Winters, J. M., Le Bertre, T., Gérard, E., & Matthews, L. D. 2010b, *A&A*, 515, 112
- Little, S. J., Little-Marenin, I. R., & Hagen Bauer, W. 1987, *AJ*, 94, 981
- Lorenz-Martins, S. 1996, *A&A*, 314, 209
- Loup, C., Forveille, T., Omont, A., & Paul, J. F. 1993, *A&AS*, 99, 291
- Martin, D. C. et al. 2007, *Nature*, 448, 780
- Matthews, L. D. & Reid, M. J. 2007, *AJ*, 133, 2291
- Matthews, L. D., Libert, Y., Gérard, E., Le Bertre, T., & Reid, M. J. 2008, *ApJ*, 684, 603
- Matthews, L. D., Gérard, E., Johnson, M. C., Le Bertre, T., Libert, Y., & Reid, M. J. 2011a, in *Why Galaxies Care about AGB Stars II: Shining Examples and Common Inhabitants*, ed. F. Kerschbaum, T. Lebzelter, & R. F. Wing, (ASP: San Francisco), 445, 305
- Matthews, L. D., Libert, Y., Gérard, E., Le Bertre, T., Johnson, M. C., & Dame, T. M. 2011b, *AJ*, 141, 60
- Matthews, L. D., Marengo, M., Evans, N. R., Bono, G. 2012, *ApJ*, 744, 53
- Mennessier, M. O., Mowlavi, N., Alvarez, R., & Luri, X. 2001, *A&A*, 374, 968
- Menten, K. M., Reid, M. J., Kamiński, T., & Claussen, M. J. 2012, *A&A*, 543, 73
- Merrill, P. W. 1956, *PASP*, 68, 70
- Milam, S. N., Apponi, A. J., Woolf, N. J., & Ziurys, L. M. 2007, *ApJ*, 668, L131
- Miller, A. A., Richards, J. W., Bloom, J. S., Cenko, S. B., Silverman, J. M., Starr, D. L., & Staussun, K. G. 2012, *ApJ*, 755, 98
- Mohamed, S., Mackey, J., & Langer, N. 2012, *A&A*, 541, 1
- Mohamed, S. & Podsiadlowski, P. 2007, in *15th European Workshop on White Dwarfs*, ASP Conf. Series, Vol. 372, ed. R. Napiwotzki and M. R. Burleigh, (ASP: San Francisco), 397
- Neri, R., Kahane, C., Lucas, R., Bujarrabal, V., & Loup, C. 1998, *A&AS*, 130, 1
- Olson, F. M. & Raimond, E. 1986, *A&AS*, 65, 607
- Olofsson, H., Eriksson, K., Gustafsson, B., & Carlström, U. 1993, *ApJS*, 87, 267
- Olofsson, H., González Delgado, D., Kerschbaum, F., & Schöier, F. L. 2002, *A&A*, 391, 1053
- Olofsson, H., Maercker, M., Eriksson, K., Gustafsson, B., & Schöier, F. 2010, *A&A*, 515, 27
- Perley, R. A. & Taylor, G. B. 2003, *VLA Calibration Manual* (<http://www.vla.nrao.edu/astro/calib/manual/index.shtml>)
- Perrin, G., Ridgway, S. T., Coudé du Foresto, V., Mennesson, B., Traub, W. A., & Lacasse, M. G. 2004, *A&A*, 418, 675
- Raga, A. C. & Cantó, J. 2008, *ApJ*, 685, L141
- Roy, N., Kantharia, N. G., Eyres, S. P. S., Anupama, G. C., Bode, M. F., Prabhu, T. P., & O'Brien, T. J. 2012, *MNRAS*, in press (arXiv:1209.2431)
- Sahai, R. 1990, *ApJ*, 362, 652
- Sahai, R. & Chronopoulos, C. K. 2010, *ApJ*, 711, L53
- Sahai, R., Morris, M., Knapp, G. R., Young, K., & Barbaum, C. 2003, *Nature*, 426, 261
- Samus, N. N. et al. 2004, *Combined General Catalogue of Variable Stars*
- Schöier, F. L., Lindqvist, M., & Olofsson, H. 2005, *A&A*, 391, 577
- Schöier, R., Binney, J., & Dehnen, W. 2010, *MNRAS*, 403, 1829
- Schröder, K.-P. & Sedlmayr, E. 2001, *A&A*, 366, 913
- Smith, H. 1976, *MNRAS*, 175, 419
- Soszyński, I., Udalski, A., Szymański, M. K., Kubiak, M., Pietrzyński, G., Wyrzykowski, L., Szczyżak, O., Ulaczyk, K., & Poleski, R. 2009, *Acta Astron.*, 59, 335
- Spergel, D. N., Giuliani, J. L. Jr., & Knapp, G. R. 1983, 275, 330

- Stencel, R. E. 2009, in *The Biggest, Baddest, Coolest Stars*, ASP Conf. Series, Vol. 412, ed. D. G. Luttermoser, B. J. Smith, & R. E. Stencel, 197
- Straniero, O., Chieffi, A., Limongi, M., Busso, M., Gallino, R., & Arlandini, C. 1997, *ApJ*, 478, 332
- Tisserand, P. et al. 2009, *A&A*, 501, 985
- Ueta, T. 2008, *ApJ*, 687, L33
- Ueta, T. 2011, in *Why Galaxies Care about AGB Stars II: Shining Examples and common Inhabitants*, ed. F. Kerschbaum, T. Lebzelter, & R. F. Wing, (ASP: San Francisco), 445, 295
- Ueta, T. et al. 2006, *ApJ*, 648, L39
- Ueta, T. et al. 2010, *A&A*, 514, 16
- Ueta, T., Izumiura, H., Yamamura, I., Nakada, Y., Matsuura, M., Ita, Y., Tanabé, T., Fukushi, H., Matsunaga, N., & Mito, H. 2008, *PASJ*, 60, 407
- Utsumi, L. 1985, in *Cool Stars with Excesses of Heavy Elements*, (Reidel: Dordrecht), 243
- van Belle, G., Dyck, H. M., Benson, J. A., & Lacasse, M. G. 1996, *AJ*, 112, 2147
- van Leeuwen, F. 2007, *A&A*, 474, 653
- van Marle, A. J., Maliani, Z., Keppens, R., & Decin, L. 2011, *ApJ*, 734, L26
- Vassiliadis, E. & Wood, P. R. 1993, *ApJ*, 413, 641
- Villaver, E., García-Segura, G., & Manchado, A. 2002, *ApJ*, 571, 880
- Villaver, E., Manchado, A., & García-Segura, G. 2012, *ApJ*, 748, 94
- Wang, L., Baade, D., Höflick, P., Wheeler, J. C., Kawabata, K., & Nomoto, K. 2004, *ApJ*, 604, L53
- Wareing, C. J. 2012, *ApJ*, 748, L19
- Wareing, C. J. et al. 2006, *MNRAS*, 372, L63
- Wareing, C. J., Zijlstra, A. A., & O'Brien, T. J. 2007a, *ApJ*, 660, L129
- Wareing, C. J., Zijlstra, A. A., & O'Brien, T. J. 2007b, *MNRAS*, 382, 1233
- Wareing, C. J., Zijlstra, A. A., O'Brien, T. J., Seibert, M. 2007c, *ApJ* 670, L125
- Wareing, C. J., et al. 2006b, *MNRAS*, 372, L63
- Wasatonic, R. 1995, *IBVS*, 4159, 1
- Wasatonic, R. P. 1997, *JAVSO*, 26, 1
- Whitelock, P. A., Feast, M. W., & van Leeuwen, F. 2008, *MNRAS*, 386, 313
- Wilkin, F. P. 1996, *ApJ*, 459, L31
- Winters, J. M., Le Bertre, T., Jeong, K. S., Nyman, L.-Å., & Epchtein, N. 2003, *A&A*, 409, 715
- Winters, J. M., Le Bertre, T., Pety, J., & Neri, R. 2007, *A&A*, 475, 559
- Young, K., Phillips, T. G., & Knapp, G. R. 1993a, *ApJS*, 86, 517
- Young, K., Phillips, T. G., & Knapp, G. R. 1993b, *ApJ*, 409, 725
- Zijlstra, A. A. & Weinberger, R. 2002, *ApJ*, 572, 1006
- Zucker, D. B. & Soker, N. 1993, *ApJ*, 408, 579
- Zuckerman, B., Terzian, Y., & Silverglate, P. 1980, *ApJ*, 241, 1014